ABSTRACT

DIFFUSE SCATTERING AND LOCAL ORDER IN LEAD-BASED RELAXOR FERROELECTRICS

Matthew J. Krogstad, Ph.D.
Department of Physics
Northern Illinois University, 2018
Omar Chmaissem, Director

Relaxor ferroelectrics are characterized by their dielectric permittivity, and some of these materials display outstanding electromechanical coupling, a property that makes them useful in applications from sonar and ultrasound to precision actuators. However, there is a surprising lack of consensus regarding the local structure of these materials and how it relates to their useful bulk properties. A common feature of many proposed mechanisms is the importance of short-range order differing from the long-range symmetry of the material. Such a difference between short-range and long-range order makes these materials ideal candidates for study via diffuse scattering, a technique sensitive to differences between local and average structure.

Using modern techniques that allow a survey of a large volume of reciprocal space comprising dozens of Brillouin zones, diffuse neutron scattering data from across the entire phase diagram of the canonical relaxor ferroelectric system PMN-xPT has been collected, allowing for the identification of relevant diffuse scattering features. Complementary x-ray diffuse scattering measurements confirm the presence of these features, and the difference between scattering lengths of the two techniques provides contrast that shows how the different atoms

in the material behave. By characterizing how these features evolve with temperature and composition, they provide a connection between the bulk properties of the system and local atomic displacements and correlations underlying these bulk properties.

Four main components of diffuse scattering were found. Ferroic diffuse scattering, centered on the Bragg peak, is found to correlate in intensity to the strength of piezoelectric coupling and not directly to relaxational behavior. This study finds new structure to this component that indicates a significant role for correlated oxygen displacements in determining local polar structures. Broad, temperature-dependent diffuse peaks centered on M points in the Brillouin zone are indicative of antiferroelectric behavior that become a clear proxy for bulk relaxor behavior. Temperature-independent peaks centered on R points indicate chemical short-range order for pure PMN and are suppressed with the addition of titanium, suggesting that chemical order may seed relaxational character but is not responsible for piezoelectricity. Finally, size-effect scattering is identified and separated from other components, indicating highly anisotropic local environments. These findings are extended by studies of the electric field dependence of diffuse scattering from PMN-30PT which confirm the ferroic nature of diffuse scattering close to the Bragg peak and indicate that the local distortions revealed through size-effect diffuse scattering remain locally dominant even at high electric fields. The identification of similar features in diffuse scattering from the related material PZT indicates the applicability of these results to other lead-based perovskites with competing ferroic orders.

NORTHERN ILLINOIS UNIVERSITY
DE KALB, ILLINOIS

DECEMBER 2018

DIFFUSE SCATTERING AND LOCAL ORDER IN LEAD-BASED RELAXOR FERROELECTRICS

BY

MATTHEW J. KROGSTAD

A DISSERTATION SUBMITTED TO THE GRADUATE SCHOOL

IN PARTIAL FULFILLMENT OF THE REQUIREMENTS

FOR THE DEGREE

DOCTOR OF PHILOSOPHY

DEPARTMENT OF PHYSICS

Dissertation Director:
Omar Chmaissem

ACKNOWLEDGEMENTS

I am deeply indebted to my advisor, Omar Chmaissem, for believing in my potential as a scientist, finding a place where I could contribute to research, and supporting my professional development. I would not have attempted and could not have completed this project without his encouragement.

The Neutron and X-Ray Scattering group at Argonne National Laboratory has been a very exciting place to work as a graduate student. Raymond Osborn and Stephan Rosenkranz have been thinking about how to measure and analyze diffuse scattering for quite some time, and I have been extremely fortunate to be a part of their group at the very time that some of their more ambitious efforts began to bear fruit. I am proud to have been a part of their efforts. In this group I also worked with Jared Allred and Keith Taddei, both wonderful colleagues who provided great examples of how to be a productive part of a scientific group.

My study of relaxor ferroelectrics started with an experiment proposed by Daniel Phelan, who wanted someone with experience using *Corelli* to help with his proposal to study diffuse scattering in these materials. Upon seeing the initial results, I was rash enough to ask if I could work on these materials for my dissertation, and he was kind enough to agree. His guidance and supervision made this work possible.

I have been fortunate to meet and learn from many people with experience in both diffuse scattering and in relaxors. Peter Gehring provided invaluable insight and context on the study of PMN-xPT and relaxors. Feng Ye has made *Corelli* an extremely powerful tool for measuring neutron diffuse scattering, allowing its use in this work. Jacob Ruff provided valuable support in collecting our x-ray scattering measurements at CHESS, and Justin Wozniak provided irreplaceable computing expertise in handling the record-setting

datasets collected at CHESS. Guy Jennings developed the software CCTW for transforming x-ray scattering data, and Branton Campbell assembled the math beneath it. Reinhard Neder developed the *DISCUS* scattering program with ability to simulate the kind of data we can now routinely collect; his aid in using this program has been essential. Arkadiy Simonov provided insight as to the possibilities of analyzing scattering data through Fourier transforms; I must apologize for being unable to integrate 3D-PDF into this work! I am sure that the application of this method will ultimately improve our understanding of diffuse scattering in this and many other materials. Hiroyuki Takenaka graciously provided access to his molecular dynamics simulations for me to examine for similarities with our experimental data, and I'm pleased to say that the comparison between simulation and experiment is instructive.

Work at the Materials Science Division at Argonne National Laboratory was supported by the U.S. Department of Energy, Office of Science, Materials Sciences and Engineering. Research conducted at ORNL's Spallation Neutron Source was sponsored by the Scientific User Facilities Division, Office of Basic Energy Sciences, U.S. Department of Energy. Research conducted at the Cornell High Energy Synchrotron Source (CHESS) was supported by the NSF and NIH/NIGMS via NSF award DMR-1332208.

DEDICATION

To my parents, Cathy and Craig, and to my wife, Liz, for their patience, support, and love.

TABLE OF CONTENTS

LIST OF TABLES

LIST OF FIGURES

LIST OF APPENDICES

CHAPTER 1

INTRODUCTION TO DIFFUSE SCATTERING

One of the most successful applications of physics in the modern era has been the study of solid materials in the crystalline state. The near-infinite periodicity of crystalline materials allows physicists to derive exact or near-exact solutions for many-body systems from the atomic structure of these materials, directly applying quantum mechanical principles to common macroscopic systems. However, there is increasing interest in materials where deviations from ideal crystallinity are physically important. Such deviations from long-range order are of increasing scientific interest, as they may help explain poorly understood physical phenomena such as colossal magnetoresistance [1], geometric frustration [2], fast ion conduction [3], and relaxor ferroelectricity [4].

Neutron and x-ray scattering are among of the most powerful tools for understanding crystal structure. While the long-range order of a crystal determines Bragg scattering, deviations from long-range order determines diffuse scattering. Interest in diffuse scattering is not new [5, 6], but it has been experimentally difficult to measure in large volumes for single crystals. Recent advances in instrumentation combined with improved computation resources allow for single crystal diffuse scattering surveys of unprecedented scope and rapidity. As these experiment methods are being developed, methods of analyzing diffuse scattering are improving, allowing for important insights into the short-range order within a crystalline material.

This dissertation will discuss the application of these new experimental methods to the relaxor ferroelectric system PMN-xPT. Relaxor ferroelectrics have been of significant scientific and technical interest for some time [4, 7]; however, a complete physical explanation of

these materials remains elusive. Short-range order has long been invoked when discussing relaxor ferroelectrics [8], and diffuse scattering has long been considered a hallmark of the relaxor state. As such, PMN-xPT is an important test case for both the measurement and understanding of diffuse scattering.

This dissertation will first discuss diffraction and the theory of diffuse scattering in Chapter 1, which mostly follows the derivations found in [9], adding a few clarifying points and examples. This chapter will also discuss the intruments and methods for measuring diffuse neutron and x-ray scattering. Chapter 2 will briefly address ferroelectrics, relaxors, and the solid solution PMN-xPT, discussing why short-range order is important to the system. Chapter 3 will detail the extensive diffuse scattering studies performed for this work on PMN-xPT, first summarizing the findings of the neutron and x-ray experiments, then detailing the understading gained from examining each component of diffuse scattering. Chapter 4 will describe diffuse scattering experments on PMN-30PT performed with an applied electric field and how the changes observed in diffuse scattering offer new insights into the underlying local order present in PMN-30PT. Chapter 5 will describe the results of diffuse scattering experiments performed on $PbZr_{0.54}Ti_{0.46}O_3$, a similar system to PMN-xPT that shows how the local ordering found in PMN-xPT may be generalized to other systems.

1.1 Scattering Theory for Crystalline Solids

A crystal is material that can be described by a unit cell, an arrangement of atoms repeating in three dimensions throughout a material [10]. For any macroscopic object, the spatial extent of this lattice is acceptably approximated by the limit where the lattice is infinite in extent. Mathematically described, a unit cell is defined by three linearly independent basis vectors $\mathbf{a}_1$, $\mathbf{a}_2$, $\mathbf{a}_3$, and a finite number of atoms occupying defined positions within the

volume defined by those basis vectors. Each atom, labelled j, has a position in the unit cell $\mathbf{r}_j$ expressed as a fraction x_i of the basis vectors:

$$\mathbf{r}_j = x_1\mathbf{a}_1 + x_2\mathbf{a}_2 + x_3\mathbf{a}_3$$

Using this language, the displacement $\mathbf{d}_{ij}$ between *any* two atoms ij in the crystal can be expressed as $\mathbf{d}_{ij} = n_1\mathbf{a_1} + n_2\mathbf{a_2} + n_3\mathbf{a_3} + \mathbf{r}_i - \mathbf{r}_j$, with the n_i being integers; this strongly restricts the relative position of atoms in a crystalline system. The unit cell is not a uniquely determined property of a material. The choice of the origin is arbitrary, and one can continuously redefine the $\mathbf{r}_j$ while still describing the same physical arrangement of atoms. One can also take any unit cell and obtain new basis vectors by multiplying an existing set by integers; the new unit cell will still be able to describe the position of each atom in the crystal. However, a unit cell can be chosen so as to minimize unit cell volume and to best reflect the symmetry operations under which the crystal will be invariant; such a unit cell is called a primitive unit cell.

The lattice will be invariant under some set of proper and improper rotations; these symmetries define the point group of the lattice. There is also a considerable degree of discrete translational invariance, as the lattice is also invariant under translation by a linear combination of integer multiples of the basis vectors. The combined rotational and translational invariances of a lattice define the space group of that lattice. For three-dimensional lattices, there are 32 point groups and 230 space groups. With an appropriate unit cell chosen, the unit cell is characterized by the lattice parameters a, b, c, α, β, and γ (Fig. 1.1). The lengths a, b, and c describe the length of the basis vectors, while α, β, and γ are the angles between the basis vectors.

In anticipation of the consideration of scattering from crystals, it is useful to define the reciprocal lattice, a vector space derived from the basis vectors of the crystal lattice in real

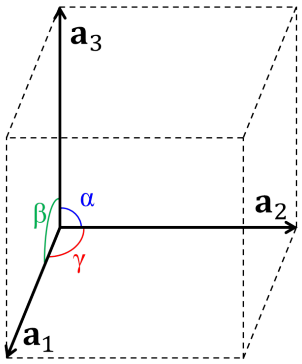

Figure 1.1: The unit cell is defined by the basis vectors $\mathbf{a_1}, \mathbf{a_2}, \mathbf{a_3}$. a, b, c are the lengths of the vectors, and the angles between the $\mathbf{a_i}$ are denoted by α, β, γ.

space. The basis vectors $\mathbf{a}_i^*$ of this reciprocal lattice will be defined using the real space basis vectors $\mathbf{a}_i$ as

$$\mathbf{a}_i^* = 2\pi \frac{\mathbf{a}_j \times \mathbf{a}_k}{\mathbf{a}_i \cdot (\mathbf{a}_j \times \mathbf{a}_k)}$$

By this construction, the real and reciprocal lattice vectors have the useful property

$$\mathbf{a}_i \cdot \mathbf{a}_j^* = 2\pi\delta_{ij}$$

with δ_{ij} the Kronecker delta function. Where the crystal lattice is expressed in units of length, the reciprocal lattice has units of inverse length. The region of reciprocal space surrounding points on the reciprocal lattice defines the first Brillouin zone of the reciprocal lattice (Fig. 1.2), analogous to the unit cell.

It is difficult to directly examine the atomic lattice defining the structure of a crystalline material. Even those tools which do directly probe the atomic structure of a material are inevitably focused on the surface and have difficulty providing a statistical average of the structure throughout a bulk material. The scattering of some mediating particle (usually x-rays, neutrons, or electrons) from a crystalline lattice provides indirect information as to the structure of the lattice. Scattering from an ideal crystal is described by Bragg's Law.

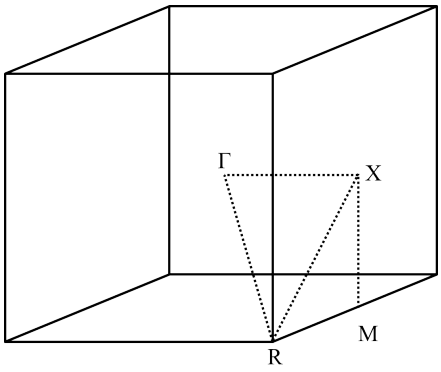

Figure 1.2: The first Brillouin zone for a cubic reciprocal lattice. The center of the zone is a reciprocal lattice point, represented by $h\mathbf{a}_1^* + k\mathbf{a}_2^* + l\mathbf{a}_3^*$, with $h, k, l \in n$ (n is the set of all integers). This zone center can be referred to as the Γ point. Other special points include the **X** point, with two of h, k, l belonging to n and one belonging to $n + \frac{1}{2}$; the **M** point, with one of h, k, l belonging to n and two belonging to $n + \frac{1}{2}$, and the **R** point, with h, k, l all belonging to $n + \frac{1}{2}$.

In its simplest form, Bragg's Law is expressed as a condition for the scattering of a beam of wavelength λ incident upon a series of equally spaced planes to constructively interfere after reflection:

$$n\lambda = 2d\sin(\theta)$$

Here, d is the distance between planes, θ the angle between the incident beam and the series of planes, and n some natural number. The scattered wave will exhibit constructive interference only for certain discrete values of θ; for most values of θ, the scattered wave will destructively interfere with itself and produce no scattering amplitude.

As defined earlier, a crystal can be considered a three-dimensional array of atoms, forming regularly-spaced planes in three dimensions. Constructive interference will occur if the Bragg's Law is simultaneously satisfied in three dimensions. For an incident wave of

wavelength λ travelling along unit vector $\hat{\mathbf{k}}_\mathbf{0}$ and scattering elastically along unit vector $\hat{\mathbf{k}}$ and letting $\mathbf{Q} = \hat{\mathbf{k}}_\mathbf{0} - \hat{\mathbf{k}}$, this is described by the three Laue conditions:

$$\mathbf{Q} \cdot \mathbf{a}_1 = 2\pi\lambda h$$

$$\mathbf{Q} \cdot \mathbf{a}_2 = 2\pi\lambda k$$

$$\mathbf{Q} \cdot \mathbf{a}_3 = 2\pi\lambda l$$

with h, k, l being integers. Expressing the incident wavevector in terms of the reciprocal lattice basis vectors $\mathbf{a}_i^*$ yields

$$\mathbf{Q} = (h\mathbf{a}_1^* + k\mathbf{a}_2^* + l\mathbf{a}_3^*)$$

Just as the periodicity of the lattice defines a natural basis in real space, Bragg peaks in reciprocal space form a lattice defined by the reciprocal space basis vectors. For an ideal crystal, it is only at discrete wavevector points matching linear combinations of integer multiples of the reciprocal lattice basis vectors that a scattered beam will constructively interfere and produce intensity. Sampling a range of $\mathbf{Q}$ will yield no scattered intensity for almost all scattered vectors but will find sharp peaks of intensity at $\mathbf{Q}$ coinciding with reciprocal lattice points (Fig. 1.3). These discrete points are referred to as Bragg peaks, and the integer multiples h, k, l of the vector are adopted as the Miller indices of Bragg peaks[1]. These peaks are a natural reference point in reciprocal space. Within the first Brillouin zone surrounding a Bragg peak hkl, a point in reciprocal space can be defined by a reciprocal space vector from the center of the zone $\mathbf{Q}_{hkl}$ to the point $\mathbf{q}_{hkl} = \mathbf{Q} - \mathbf{Q}_{hkl}$.

[1]The indices hkl can be used to refer to several distinct objects. Without any parentheses, hkl refers to the Bragg peak itself. (hkl) refers to a plane in reciprocal space, e.g., $(hk0)$ is the plane where $l = 0$. $[hkl]$ refers to a direction in reciprocal space, e.g,. [111] would be the direction from the 321 reflection to the 432 reflection, and $\langle hkl \rangle$ refers to the set of all directions symmetrically equivalent to $[hkl]$. In the interest of compactness, a negative number is indicated by an overscore, e.g. $1\bar{1}0$.

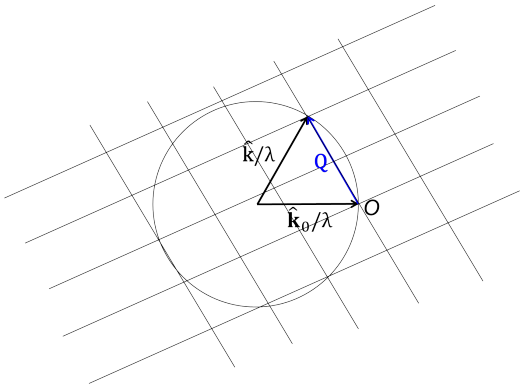

Figure 1.3: The Ewald Sphere construction is a useful visualization of Bragg's Law. The sphere has radius $1/\lambda$, the incident and scattered wave vectors $\hat{\mathbf{k}}_\mathbf{0}/\lambda$ and $\hat{\mathbf{k}}/\lambda$ point from the center of the sphere to the surface, and the origin O of the reciprocal lattice of the scattering crystal coincides with the end of the incident wave vector $\hat{\mathbf{k}}/\lambda$. Bragg's Law is satisfied if $\mathbf{Q}$ intersects a lattice point on the reciprocal lattice.

The amplitude of the scattered wave is determined by the atoms j within each unit cell and their relative positions and is proportional to the structure factor $F(\mathbf{Q})$:

$$F(\mathbf{Q}) = \sum_j f_j(\mathbf{Q}) e^{i\mathbf{Q}\cdot\mathbf{r}_j}$$

In this equation, $f_j(\mathbf{Q})$ represents the scattering length for atom j. For x-rays, which interact with charge density, this scattering length is mostly proportional to the atomic number Z, and decays as $\mathbf{Q}$ increases due to the extended nature of the electrons surrounding the nucleus. For neutrons, which interact with the point-like atomic nuclei via the strong nuclear force, the form factor is constant to very large $\mathbf{Q}$ (at least 100 Å^{-1}) and is not directly related to the atomic number. This is well-approximated by the Fermi pseudopotential $\hat{U}(\mathbf{r}) = b_j\delta(\mathbf{r} - \mathbf{R}_j)$, with j being some atom and b_j being its neutron scattering length [11].

For a crystal containing N unit cells, the observed intensity $S(\mathbf{Q})$ is given by $S(\mathbf{Q}) = N^2|F(\mathbf{Q})|^2$. More generally, $S(\mathbf{Q})$ from a collection of scatterers m with position $\mathbf{R}_m$ is given by

$$S(\mathbf{Q}) = \sum_{m} \sum_{m'} f_m f_{m'} e^{i\mathbf{Q}\cdot(\mathbf{R}_m - \mathbf{R}'_m)}$$

Even more generally, $S(\mathbf{Q})$ can be viewed as the Fourier transform of scattering density of the crystal:

$$S(\mathbf{Q}) \propto |\int e^{i\mathbf{Q}\cdot\mathbf{r}} \rho(\mathbf{r}) d\mathbf{r}|^2$$

The scattering density $\rho(\mathbf{r})$ here will depend on the interaction between the crystal and the scattering medium. X-rays will interact with charge, making $\rho(\mathbf{r})$ the charge density of the crystal, while neutrons interact most strongly with nuclei, making $\rho(\mathbf{r})$ the nuclear scattering length density. The Fourier transform of a diffraction pattern is called the Patterson function and is an auto-correlation (or pair-distribution) function of scattering density. Measured diffraction intensities will always display inversion symmetry, even if the lattice that generates these intensities does not. This is a consequence of Friedel's Law for Fourier transforms [12], and it means that a scattering experiment cannot distinguish between some atomic arrangement and its spatial inverse. This result holds beyond the case of the ideal crystal.

One of the assumptions made so far is that the scattered particle scatters without any gain or loss in energy, or *elastically*. Inelastic scattering occurs when the scattered particle gains or loses energy in its interaction with the scattering material. Elastic scattering does not only originate from a purely static lattice; it represents the static correlations of a dynamic system, with more scattering being inelastic in proportion with the dynamics of the system. Inelastic scattering provides a view of the phonon dynamics of the lattice [11].

1.2 Diffuse Scattering from Crystalline Materials

For all the successes of the theory of crystalline materials, there are numerous ways in which real materials deviate from the assumptions made in describing them. The prior treatment of scattering from an ideal crystal depends on a perfect lattice of infinite extent, in which every unit cell is exactly identical. Real materials can deviate from this ideal in many ways, and even subtle deviations from the assumptions of ideal crystallinity can have strong effects on material properties. For example, the assumptions of infinite periodicity are violated near surfaces of materials and at interfaces between areas of different crystal systems, and the physics of thin films and polycrystalline materials can be drastically different from those of bulk single crystals.

Structural deviations from ideal crystallinity affect scattering from crystalline materials by allowing scattering that does not arise from the restrictive Bragg condition. This scattering may appear anywhere in reciprocal space, both coinciding with the Bragg peaks and between them, and is generally referred to as diffuse scattering. Diffuse scattering is typically several orders of magnitude weaker than Bragg scattering [9], making measurement difficult, but it can provide insight into local correlations that differ from the average structure of a material.

While deviations from ideal crystallinity complicate the preceding discussion of scattering, scattering can still be expressed as the Fourier transform of scattering density [13]. Quite generally, diffuse scattering is produced by various moments of the probability distribution of atomic positions from their average positions and is indifferent to the physical forces generating those moments; any kind of probability correlation in occupancy or displacement that is non-zero locally but zero for the average crystal can produce diffuse scattering. Just as the three-dimensional correlations of atomic positions in real space produces sharp zero-

dimensional points in reciprocal space, the dimensionality of short-range correlations in real space determines the shape of the corresponding diffuse scattering so that the sum of the dimensionalities equals that of the space. For a three dimensional crystal, a one-dimensional correlation will produce a plane of diffuse scattering. More quantitatively, the scattering equation can be modified to allow for deviations in both the occupation of crystallographic sites and the position of the atoms at those sites, with conditional correlations of and between these types of deviations producing scattering differing from Bragg scattering from an ideal crystal. Following the treatment of Borie and Sparks [14] (and subsequent [9,15]), each atom j has a position $\mathbf{r}_j = \mathbf{R}_j + \mathbf{u}_j$, with $\mathbf{u}_j$ being the deviation of atom j from its average position $\mathbf{R}_j$; all of these are expressed in fractional coordinates of the unit cell. This modifies the original scattering equation:

$$S(\mathbf{Q}) = \sum_i \sum_j b_i b_j \exp(i\mathbf{Q} \cdot (\mathbf{R}_i + \mathbf{u}_i - \mathbf{R}_j - \mathbf{u}_j))$$

$$S(\mathbf{Q}) = \sum_i \sum_j b_i b_j \exp(i\mathbf{Q} \cdot (\mathbf{R}_i - \mathbf{R}_j)) \exp i\mathbf{Q} \cdot (\mathbf{u}_i - \mathbf{u}_j))$$

The exponential term containing the deviation term can be expanded in a Taylor series:

$$S(\mathbf{Q}) = \sum_i \sum_j b_i b_j \exp(i\mathbf{Q} \cdot (\mathbf{R}_i - \mathbf{R}_j)) \times \left\{1 + i\mathbf{Q} \cdot (\mathbf{u}_i - \mathbf{u}_j) - \frac{1}{2}\mathbf{Q} \cdot (\mathbf{u}_i - \mathbf{u}_j)^2 - ...\right\}$$

Subtracting the Bragg scattering yields a separation of diffuse scattering terms in the exponent of the deviation $\mathbf{u}_j$:

$$I_{diffuse} = I_0 + I_1 + I_2 + ...$$

These first three terms will be considered in more detail. Higher-order terms exist and can contribute to diffuse scattering, but tend to be of vanishing importance compared to the first three since $(\mathbf{u}_i - \mathbf{u}_j) \ll 1$ even in non-ideal crystals. In a case where is necessary to consider I_3 or some higher-order term, it is very likely that at least one of the first three terms will also require consideration.

1.2.1 Chemical Short-Range Order

Chemical short-range order occurs when there are multiple possible occupants of a certain crystallographic site, and the probability of a certain occupant is dependent on the occupation of neighboring sites. More formally, consider a material that has a crystallographic site with multiple possible occupants i, each with a concentration c_i; by definition, $\sum_i c_i = 1$. For any two sites separated by real space vector $\mathbf{d}_{lmn}$ (expressed in real-space lattice units l, m, and n), the probability that the first is occupied by occupant i and the second by occupant j is denoted p^{ij}_{lmn}. These p^{ij}_{lmn} are of course strongly correlated with each other; if there are N possible occupants, the p^{ij}_{lmn} will number N^2 , but the number of *independent* parameters defining the p^{ij}_{lmn} is $\frac{1}{2}(N \times (N-1))$ for $N > 1$. Also useful is the conditional probability P^{ij}_{lmn}, defined as the probability that occupant j is found at the end of average lattice vector $\mathbf{d}_{lmn}$ given that occupant i is found at the beginning of that vector; this probability is somewhat more naturally applied to the expansion of the scattering equation. It should be noted that $c_i P^{ij}_{lmn} = p^{ij}_{lmn}$.

A final set of quantities useful in considering chemical short-range order are the Warren-Cowley short-range order parameters α^{ij}_{lmn} [16], which are defined as follows:

$$\alpha^{ij}_{lmn} = 1 - \frac{P^{ij}_{lmn}}{c_j}$$

While this term may seem to add nothing but another layer of variables to an already variable-laden discussion, the Warren-Cowley parameters are a natural term with which to discuss chemical short-range order. Most usefully, it is noted that $\alpha^{ij}_{lmn} = 0$ when $P^{ij}_{lmn} = c_j$, describing a conditional probability identical to that random occupation. An $\alpha^{ij}_{lmn} > 0$ describes a probability of ij pairs for vectors $\mathbf{d}_{lmn}$ being less than would be expected if the species were randomly distributed, and $\alpha^{ij}_{lmn} < 0$ describes a probability of ij pairs being greater than expected in the random case.

A useful identity in this formulation is $\alpha^{ij}_{lmn} = \alpha^{ji}_{lmn}$. This can be shown by applying Bayes' Theorem, $\frac{P(A|B)}{P(A)} = \frac{P(B|A)}{P(B)}$, to the definitions of the Warren-Cowley parameters:

$$\frac{P^{ij}_{lmn}}{c_j} = \frac{P^{ji}_{lmn}}{c_i} \Rightarrow P^{ij}_{lmn} = \frac{c_j}{c_i} P^{ji}_{lmn}$$

$$\alpha^{ij}_{lmn} = 1 - \frac{P^{ij}_{lmn}}{c_j} = 1 - \frac{c_j}{c_i}\frac{P^{ji}_{lmn}}{c_j} = 1 - \frac{P^{ji}_{lmn}}{c_i} = \alpha^{ji}_{lmn}$$

Another useful property of the α^{ij}_{lmn} is

$$\sum_j c_j \alpha^{ij}_{lmn} = 0$$

,

derived from the definition of the α^{ij}_{lmn}, $\sum_j P^{ij}_{lmn} = 1$, and $\sum_j c_j = 1$:

$$P^{ij}_{lmn} = c_j(1 - \alpha^{ij}_{lmn})$$

$$\sum_j \frac{P^{ij}_{lmn}}{c_j} = \sum_j c_j(1 - \alpha^{ij}_{lmn}) = 1$$

$$\sum_j c_j - \sum_j c_j \alpha^{ij}_{lmn} = 1$$

$$\sum_j c_j \alpha^{ij}_{lmn} = 0$$

For binary systems in particular, it is seen that $\alpha^{ij}_{lmn} = -\frac{c_i}{c_j}\alpha^{ii}_{lmn}$. As there is only one indepent parameter defining the probability of the four possible atomic pairs, there is only one independent α^{ij}_{lmn} for a given lmn.

Returning to the scattering equation, the first term in the diffuse scattering expansion can now be expressed as a function of reciprocal space coordinate h_i (in reciprocal lattice units)[2] as a sum over distinct atomic specie pairs ij as

$$I_0 = -N \sum_{ij} \sum_{lmn} c_i c_j b_i b_j^* \alpha^{ij}_{lmn} \cos(2\pi(h_1 l + h_2 m + h_3 n))$$

The $\cos(2\pi(h_1 l + h_2 m + h_3 m))$ factor in this term makes this feature even in intensity across Bragg positions.

The effects of chemical short-range order are perhaps best illustrated by example (Fig. 1.4). Consider a binary alloy on a simple square atomic lattice with two occupants, A and B, that have equal concentration $c_A = c_B = 0.5$. In the ordered limit, A and B form a rock-salt structure on the lattice, with every atom having all four nearest-neighbors be of the other type. In this limit, the unit cell is effectively doubled in volume, with two sublattices containing each of the different types of scatterers; this leads to Bragg peaks at the $(h + \frac{1}{2}, k + \frac{1}{2}, 0)$ positions. The Warren-Cowley parameters are finite even as $\mathbf{d}_{lmn} \to \infty$, as the system can be described using long-range order. Calculating I_0 in this case would be impractical, as the series defining it is infinite; more to the point, this case can be adequately described using the doubled unit cell in a case of no disorder. In the opposite, disordered limit, the occupation of every site is completely random and uncorrelated with its neighbors. The scattering pattern resulting from the disordered system is identical to a monatomic lattice with scattering factor equal to the average of A and B; as the cubic unit cell is

[2]The use of reciprocal lattice units to express reciprocal space coordinates and fractional coordinates to express atomic positions will add a factor of 2π to these equations; as diffuse scattering data is usually best expressed in reciprocal lattice units, this is a considerable convenience.

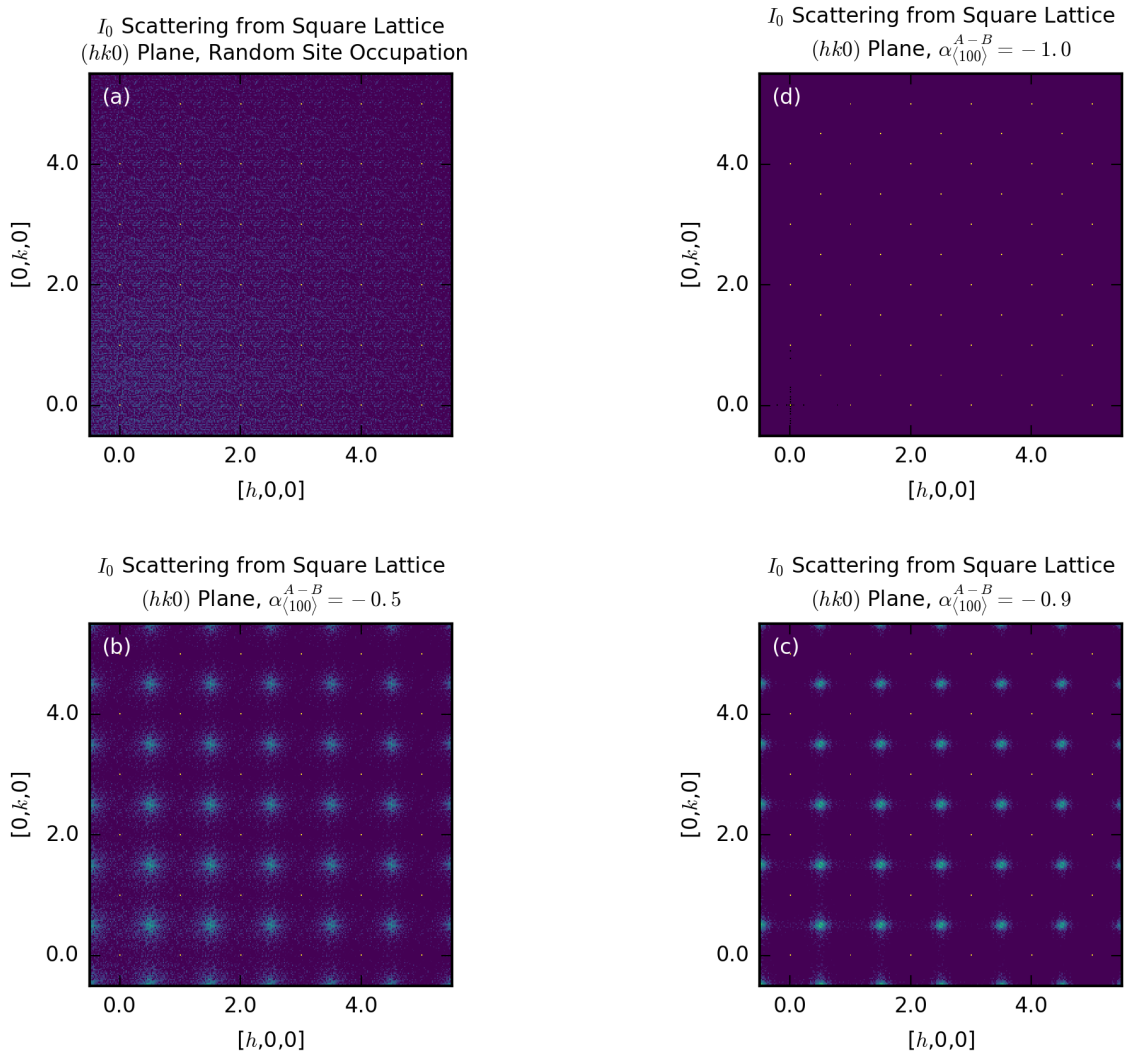

Figure 1.4: A simple 200 × 200 square atomic lattice with two occupants of equal concentration will produce I_0 scattering depending on the Warren-Cowley parameters. (a) Random occupation of sites; the only diffuse scattering is Laue monotonic scattering. (b) Rock-salt ordering of atoms, effectively doubling the unit cell. (c) Short-range order generated using a Monte Carlo process in DISCUS with $\alpha^{A-B}_{\langle 100\rangle} = -0.5$. (d) Short-range order generated using a Monte Carlo process in DISCUS with $\alpha^{A-B}_{\langle 100\rangle} = -0.9$. For (c) and (d), only first nearest-neighbor interactions were used in the Monte Carlo simulation, but higher correlations are present.

appropriately chosen, there will be no Bragg peaks at non-integer positions. In both of these extreme cases, diffuse scattering is minimal, only arising from self-correlation of the I_0 term. This scattering is called Laue monotonic scattering, and it is quite weak, only observable in systems with very little short-range order.

In between the completely ordered and the completely random limits are states defined by chemical short-range order. In these states, the Warren-Cowley parameters are non-zero for certain $\mathbf{d}_{lmn}$ within some finite upper bound for $mathbfd$; above this upper bound, all $\mathbf{d}_{lmn}$ are zero. As might be expected, scattering from such materials falls in between the completely ordered and completely disordered limits, with broad, diffuse peaks present at $h + \frac{1}{2}, k + \frac{1}{2}, 0$ positions. The width of these peaks is inversely related to the length of correlations [17].

1.2.2 Size-Effect Scattering

Diffuse scattering may also result from the displacement of an atom being dependent upon the chemical identity of a neighbor. Such scattering is referred to as size-effect scattering. This is associated with the I_1 term of the diffuse expansion. Short-range displacement correlations now need to be considered. With the position of each atom being $\mathbf{r}_j = \mathbf{R}_j + \mathbf{u}_j$, the displacement from equilibrium position $\mathbf{u}_j$ can be broken into its components,

$$X^{ij}_{lmn} = (\mathbf{u}^j_{lmn})_x - (\mathbf{u}^i_0)_x$$

$$Y^{ij}_{lmn} = (\mathbf{u}^j_{lmn})_y - (\mathbf{u}^i_0)_y$$

$$Z^{ij}_{lmn} = (\mathbf{u}^j_{lmn})_z - (\mathbf{u}^i_0)_z$$

Applying the same substitution of P^{ij}_{lmn} and c_j to the second term of the expansion yields

$$I_1 = -2\pi N \sum_{ij} \sum_{lmn} c_i c_j b_i b_j^* (1 - \alpha^{ij}_{lmn}) \sin(2\pi(h_1 l + h_2 m + h_3 m)) \times \left[h_1 \langle X^{ij}_{lmn} \rangle) + (h_2 \langle Y^{ij}_{lmn} \rangle) + (h_3 \langle Z^{ij}_{lmn} \rangle)\right]$$

While more complicated than I_0, a few key features of I_1 can be seen in this analytical form. The sine term means that I_1 will be antisymmetric with respect to Bragg peaks. Atomic specie is important here due to the odd expectation value for deviations of type X^{ij}_{lmn}; this will usually suppress interactions between atoms of the same type for this term, as any deviation from $X^{ii}_{lmn} = 0$ would define a new unit cell. I_1 thus describes diffuse scattering resulting from a dependence of atomic displacements upon atomic specie, or a size-effect[3].

As an example, consider again a simple square atomic lattice of two atom types, A and B, with equal concentration $c_A = c_B = 0.5$, these atoms are randomly distributed, making $\alpha^{A-B}_{lmn} = 0$ for all lmn and suppressing I_0 diffuse scattering. The average nearest-neighbor distance defines the size of the unit cell, but this nearest-neighbor distance varies locally depending on the atom pair: $A - A$ pairs tend to have a smaller nearest-neighbor distance than average, $B - B$ pairs tend to have a larger distance, and $A - B$ pairs tend to the average. The diffuse scattering produced by this short-range order will be odd in parity across Bragg positions and will depend on the relative scattering lengths of A and B (Fig. 1.5).

[3]This is not to be confused with a dependence of scattering on the size of the crystal itself! Such a dependence on physical crystal size is usually due to deviations in structure at the surface of a crystal and will be referred to here as a skin effect.

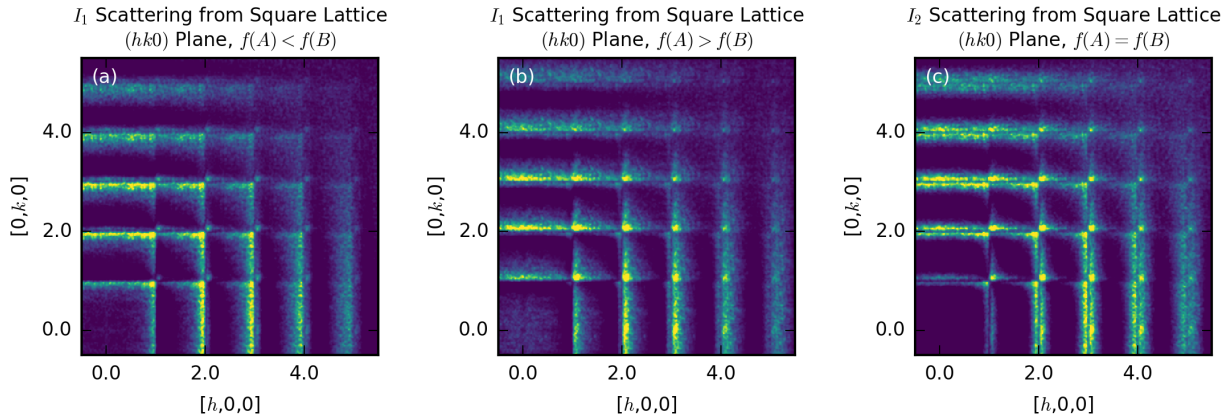

Figure 1.5: A simple 100×100 square atomic lattice with two occupants A and B of equal concentration produces I_1 scattering. A Monte Carlo procedure optimized the displacements between $A-A$ atoms pairs to be 0.95 times that of the average, $A-B$ pairs to be of average distance, and $B-B$ pairs to be 1.05 times the average. Higher-order interatomic distances are not considered in the simulation but are affected. (a) Scattering length $f(A) < f(B)$. (b) Scattering length $f(B) < f(A)$. (c) The scattering lengths $f(A) = f(B)$. This could be considered I_2 type scattering, as the atoms could be considered to be identical.

1.2.3 Displacement Correlations

Displacement correlations can also be independent of the chemical species. The next term in the expansion is related to the mean-square deviation of the displacements:

$$
\begin{aligned}
I_2 = -2\pi^2 N \sum_{ij} \sum_{lmn} c_i c_j b_i b_j^* (1 - \alpha_{lmn}^{ij}) \cos(2\pi h_1 l + h_2 m + h_3 n) \\
\times \big[h_1^2 (\langle (X_{lmn}^{ij})^2 \rangle - (1 - \alpha_{lmn}^{ij})^{-1} \langle (X_{\infty}^{ij})^2 \rangle) \\
+ h_2^2 (\langle (Y_{lmn}^{ij})^2 \rangle - (1 - \alpha_{lmn}^{ij})^{-1} \langle (Y_{\infty}^{ij})^2 \rangle) \\
+ h_3^2 (\langle (Z_{lmn}^{ij})^2 \rangle - (1 - \alpha_{lmn}^{ij})^{-1} \langle (Z_{\infty}^{ij})^2 \rangle) \\
+ 2h_1 h_2 \langle X_{lmn}^{ij} Y_{lmn}^{ij} \rangle + 2h_1 h_3 \langle X_{lmn}^{ij} Z_{lmn}^{ij} \rangle + 2h_2 h_3 \langle Y_{lmn}^{ij} Z_{lmn}^{ij} \rangle \big]
\end{aligned}
$$

Note that both time-averaged and spatially averaged terms can be included here; the I_2 term is often referred to as the thermal diffuse scattering and Huang scattering component ([9, 15]).

One can generate this kind of scattering by returning to the example of I_1, with atomic displacements depending on the ij pair, and giving each atom an identical scattering length (Fig. 1.5(c)). In this case, the I_1 scattering term vanishes, as there is only one type of atomic specie pair, and the average displacement X_{lmn}^{ii} from average positions is zero. The mean-square displacement, however, remains non-zero, producing a finite I_2 term.

A similar example of I_2 scattering is Huang scattering, where a dilute 'defect' atom in a lattice induces a local distortion in the lattice, forcing nearby atoms to respond. While the defect atoms could be a source of I_1 scattering if their scattering lengths differ from that of the host lattice, they are sufficiently few in number that the greater effect is caused by the distortion of the atoms in the host lattice. The resulting scattering (Fig. 1.6) is very much

like that seen from a size-effect where the scattering lengths are equal. Notably, scattering from atoms moving away from a defect is quite similar to that of atoms moving toward the defect; the even parity of the cosine terms makes the I_2 contribution from both cases identical.

As a final example of this term, consider a square lattice of atoms, this time all occupied by the same type of atom. Each atom is displaced from its average position in its unit cell by the same distance δ along one of four possible $\langle 100 \rangle$ directions or $\langle 110 \rangle$ directions. The direction of the displacements is correlated between unit cells, with like displacements being favored and opposite displacements being disfavored. The displacement directions between the atoms correlate between either nearest neighbors or next-nearest neighbors. The diffuse scattering patterns produced all display rods of scattering (Fig. 1.7), reflecting the one-dimensional nature of the real space correlations. It is seen that the direction of the rods in reciprocal space is determined by the direction of the correlation and not the direction of the displacement. It is also notable that the real space displacements are all discrete while the diffuse scattering is broad and continuously varying.

1.3 Measuring Diffuse Scattering

The goal of a diffuse scattering experiment is the mapping of reciprocal space intensities in an area or volume of interest. While these experiments can borrow instrumentation, detectors, and language from single-crystal diffraction experiments, the requirements for measurements and detection are quite different. For a standard single-crystal diffraction experiment, the goal is to accurately determine the intensity and reciprocal space position of a certain number of Bragg reflections; depending on instrumentation and the system being studied, between 50 and 10000 reflections may be considered ideal. The size of the dataset

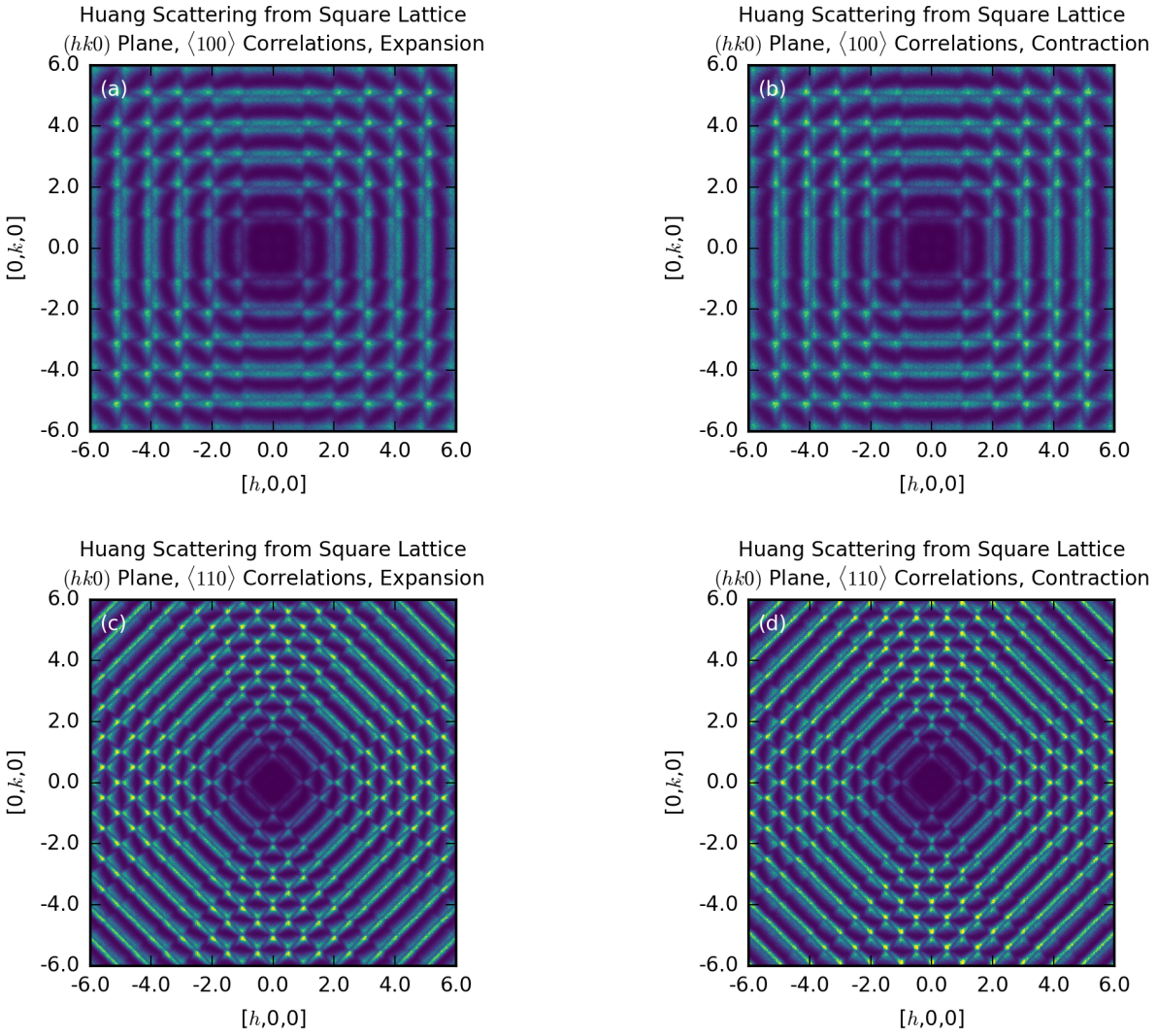

Figure 1.6: A simple 200 × 200 square atomic lattice of lattice constant a has 20 randomly selected atoms replaced by atoms of the same scattering length but different effective size. Nearest or next-nearest neighbors move toward or away from the defect, with surrounding atoms relaxing to best maintain equilibrium distance. The slight asymmetry observed is due to a contribution from the I_3 term in the expansion.

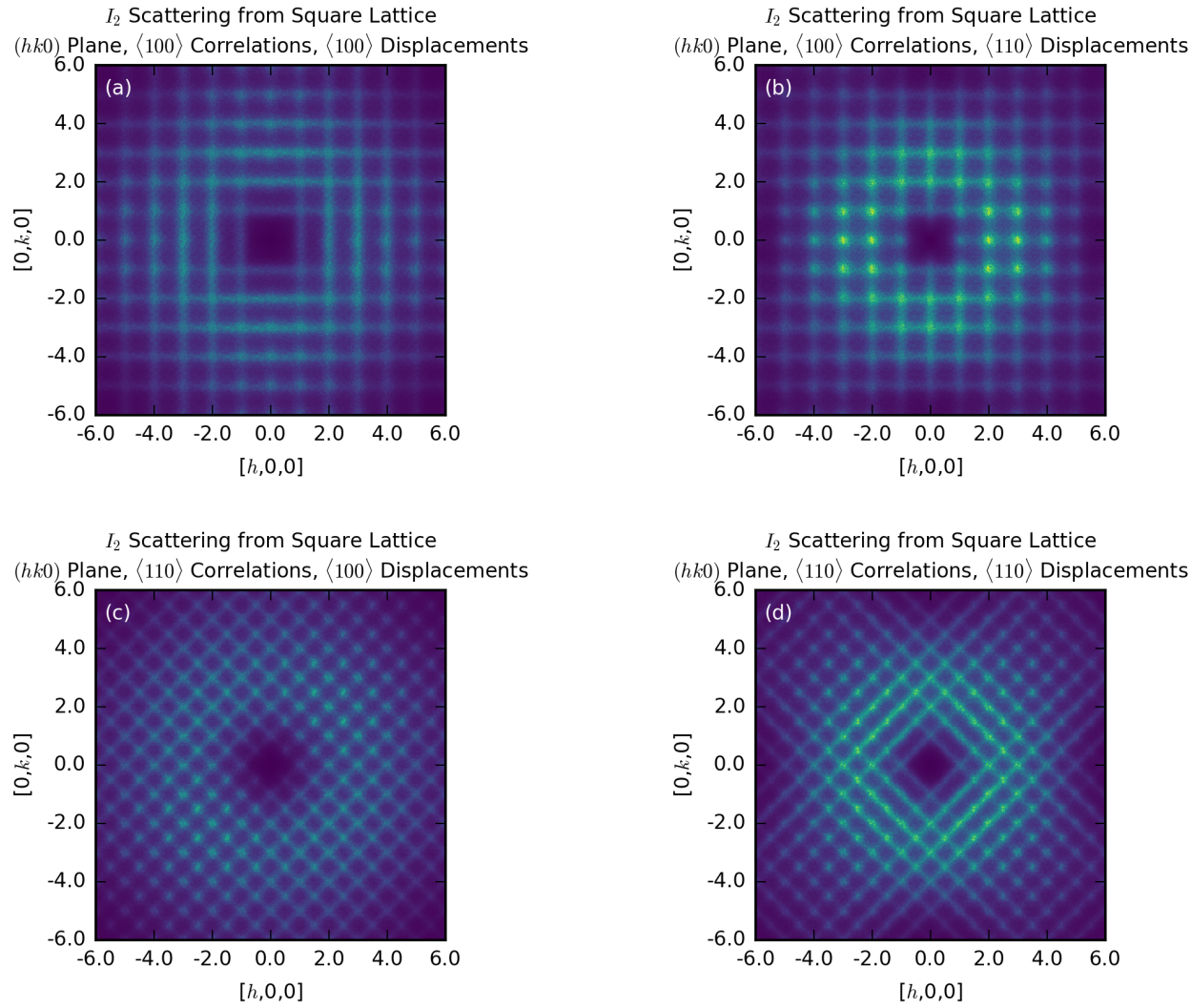

Figure 1.7: A simple 200 × 200 square atomic lattice of lattice constant a has each atom displaced by a small amount $\delta = a/20$ in one of four directions, $\langle 100 \rangle$ or $\langle 110 \rangle$. A Monte Carlo procedure produces a correlation between displacements, with displacements in the same direction being favored and those of opposite direction being disfavored; these correlations are applied to nearest neighbors or to next-nearest neighbors. The rods of scattering formed by the one-dimensional correlations are determined by the direction of the correlation, not the direction of the displacement.

is on the order of the number of reflections characterized, possibly including whatever peak profile parameters that have been extracted from the measurement.

In contrast, a diffuse scattering experiment can be interested in the intensity of every position of reciprocal space within a certain volume of interest up to a certain resolution. A very modest dataset may be comprised of scattering intensities in a well-defined plane around a single Bragg peak; even a limited picture may require some 30 points of measurement each in two dimensions to resolve anything, or on the order of 10^3 intensity measurements; this is already similar to the amount of data required for Bragg refinement! Studying multiple peaks or a three-dimensional volume using a point detector becomes impractical very quickly. Furthermore, each of these intensities will require sufficient counting time to achieve an acceptable signal-to-noise ratio. Given that diffuse scattering intensities are almost always a few to several orders of magnitude weaker than Bragg intensities, diffuse scattering studies using point detectors are usually limited to a single plane of reciprocal space surrounding one or a few Brillouin zones.

The use of area detectors allow for diffuse scattering measurements to be completed much more efficiently. While area detectors of the past have been limited by slow readout times or small dynamic range, modern x-ray and neutron area detectors are able to measure scattering intensities in a large region of reciprocal space quickly enough to allow for rapid surveys. Such instruments promise the ability to simultaneously collect Bragg intensities and diffuse scattering, making the study of diffuse scattering much more relevant to the broader crystallographic community.

While collecting data in a volume of reciprocal space may be greatly simplified, the tools used to display such data remain limited by the two-dimensional surfaces used to view them. Point detector instruments can produce line cuts of intensity; these can be reproduced from three-dimensional data but often fail to capture all the relevant features with diffuse scattering data. While three-dimensional objects may be captured and rendered

from intensity contours in measured diffuse scattering, such objects offer limited flexibility in investigating extended diffuse scattering features and may obscure unexpected features. Two-dimensional color plots match the dimensionality of the surfaces used to display data but require a color scale to define intensities; these color scales can be misleading on their own and will always have minimum and maximum values constraining the colors displayed. The challenge of accurately and completely displaying three-dimensional data on two-dimensional surfaces (such as this work) has not been solved here, but a few rules-of-thumb have been found to be useful:

1) Use a perceptually uniform color scale; grayscale is accurate but drab, the commonly-used 'jet' tends to overly emphasize mid-range colors. This work will use the 'viridis' color map from the MatPlotLib Python package.

2) Use a logarithmic scale if the features displayed differ in intensity by orders of magnitude; otherwise, use a linear color scale.

3) Show representative line cuts to isolate broad or weak features and to help track changes in ennvironment like temperature or applied field.

The Python-based program NeXpy has been used extensively in this work both to visualize and perform quantitative analysis upon both x-ray and neutron diffuse scattering data.

1.3.1 Measuring Diffuse Neutron Scattering

Neutron diffuse scattering requires a source of neutrons, usually either a reactor designed to produce a continuous neutron flux or a spallation source that produces regular pulses of intense neutron flux. Neutron sources produce significantly less flux than x-ray sources and require much longer counting times to achieve similar statistics. However, because a

neutron's velocity is proportional to its energy, one can use the time-of-flight to determine the energy of a neutron. This in turn allows the use of a broad band of wavelengths simultaneously, Laue diffractometry, while still maintaining the ability to determine the wavelength of the scattered neutron.

A standard instrument at many reactor sources is the triple-axis neutron spectrometer. Using monochromators and analyzers to establish both incident and scattered energy, triple-axis spectrometers offer resolution and flexibility in measuring inelastic signals and can be used to make high-resolution elastic measurements [18]. Most previous diffuse neutron scattering studies on relaxors have been performed using these instruments. Triple-axis spectrometers typically do not employ area detectors and are thus not optimized for diffuse scattering measurements; they are also typically limited in maximum $|\mathbf{Q}|$ to 7 Å^{-1}, with highest flux achieved within 4 Å^{-1}, greatly reducing the potential scope of study.

The instrument *Corelli* ([19–21]) at the Spallation Neutron Source is a Laue diffractometer designed to measure elastic diffuse scattering, utilizing a large bank of area detectors and a broad spectrum of neutron energies to achieve a large volume of $\mathbf{Q}$ coverage. The energy of the scattered neutrons is determined by time-of-flight, and a cross-correlation chopper that introduces a pseudorandom signal to the incident beam. By identifying events with different periodicity from the pseudorandom chopper signal, inelastic events are removed. This allows for static diffuse scattering to be separated from inelastic contributions within a certain energy resolution.

Scattering from a single sample is typically observed over a range of sample orientations to measure scattering in a large volume of $\mathbf{Q}$. *Corelli*'s CCR (closed-cycle refrigeration) unit is able to achieve a base temperature of 6 K and a maximum temperature of near 500 K without using a heat shield. Using an aluminum heat shield will add aluminum rings as a background signal while increasing the upper heat limit to 700 K; other sample environments continue to be developed and can expand this temperature range even further. Algorithms

for analyzing data collected using *Corelli* have been implemented in Mantid [22]; data from *Corelli* in this work have been processed using these Mantid algorithms.

1.3.2 Measuring Diffuse X-ray Scattering

While laboratory sources and instruments are capable of measuring diffuse scattering, x-ray synchrotron sources offer distinct advantages of easily tuned and tightly monochromatic beams and extremely high flux. However, the type of fast area detectors used to measure diffuse x-ray scattering are currently unable to determine the wavelength of scattered x-rays; this inability to measure the scattered wavelength makes diffuse x-ray scattering experiments inherently less able to distinguish between elastic and inelastic scattering.

The diffuse x-ray scattering experiments performed for this work were done at the Cornell High-Energy Sychrotron Source (CHESS), utilizing a Pilatus 6M x-ray detector with 1mm thick Si detector chips. Detector geometry parameters such as sample-to-detector distance and the beam center on the face of the detector were established by calibration to CeO_2 powder standard. A nitrogen cryostream was placed above the sample position to control sample temperature within 100 K to 400 K. A crystal was placed in the beam on a goniometer and continuously rotated about an axis denoted ϕ at a rate of 1° per second. The area detector operated continuously, reading out a new frame every 0.1 seconds over a range of ϕ angles, typically 365° but sometimes limited to a smaller range. This produces a stack of 3,650 x-ray detector images.

A peak search algorithm is then applied to the image stack to identify Bragg peaks from the sample. The 2θ angles of these peaks can be compared to those expected from the detector geometry and the unit cell of the crystal; experimental lattice parameters are extracted by refining lattice parameters, the beam center, and detector offset angles to these

2θ angles. The orientation matrix $\mathbf{U}$ of the crystal is roughly derived by assigning hkl indices to a few peaks; if this estimation is sufficient to map most of the detected peaks near to self-consistent integer hkl values, $\mathbf{U}$ can be refined further, along with offsets to the nominal goniometer angles. Using this orientation data, the raw detector data can be transformed into oriented reciprocal space using the software CCTW (Crystal Coordinate Transformation Workflow, [23]). A complete expression of detector geometry and how it relates to $\mathbf{Q}$-space is found in Appendix 1.

CCTW places x-ray counts into reciprocal space bins of constant size throughout a volume; the chosen bin size should not be smaller than the largest reciprocal space resolution in the transformed volume. Reciprocal space resolution will vary with $\mathbf{Q}$ and will have different perpendicular and in-plane components. The perpendicular component $\Delta\mathbf{Q}_\phi$ is determined by the step size $\Delta\phi$ and will vary depending on both 2θ and the relative angle μ between $\mathbf{Q}$ and the ϕ axis as $\Delta\mathbf{Q}_\phi \propto \sin\mu$. For small $\Delta\phi$:

$$
\begin{aligned}
|\Delta\mathbf{Q}_\phi| =& |\mathbf{Q}(\phi) - \mathbf{Q}(\phi + \Delta\phi)| \\
\Delta Q_x =& -Q_y \sin\Delta\phi \\
\Delta Q_y =& Q_x \sin\Delta\phi \\
|\Delta\mathbf{Q}_\phi| =& \sin\mu \sin\Delta\phi |\mathbf{Q}|
\end{aligned}
$$

The experiments conducted at CHESS used $\Delta\phi = 0.1^\circ$ and had a maximum $|\mathbf{Q}|$ of about 15 $\text{Å}^{-1} \approx 10$ r.l.u., yielding $|\Delta\mathbf{Q}_\phi| \approx 0.017$ r.l.u.

The in-plane resolution, $\Delta\mathbf{Q}_r$, can be approximated using the simple form of Bragg's Law by determining the change in d-spacing over a single detector pixel of length s_p and using the relation $|\mathbf{Q}| = \frac{2\pi}{d}$. For a scattering geometry with sample-to-detector distance l,

beam center (x_{cen}, y_{cen}), scattered beam incident on the detector at $\mathbf{r} = (x, y) - (x_{cen}, y_{cen})$, $r = |\mathbf{r}|$, and assuming the incident beam is perfectly normal to the detector face,

$$\begin{aligned}\Delta\mathbf{Q}_r =& |\mathbf{Q}(r) - \mathbf{Q}(r + s_p)| \\ =& \frac{4\pi}{\lambda} |\sin(\frac{1}{2}\arctan\frac{r}{l}) - \sin(\frac{1}{2}\arctan\frac{r + s_p}{l})|\end{aligned}$$

For the experiment at CHESS, this yields an upper limit of $\Delta\mathbf{Q}_r \approx 0.01$ r.l.u. for the aristotype perovskite unit cell.

Bin size should be chosen to be larger than both these limits. It is often desirable to have both Bragg peaks and special points on the boundary of Brillouin zones consistently lie in bin centers and not on bin boundaries; to achieve this, bins of 0.05, 0.02, or 0.01 r.l.u. are preferred. One should also consider the size of the output file; halving the bin size in each of three dimensions will increase the size of the transformed data by a factor of eight! If very high experimental resolution is achieved, it may be necessary to limit the volume of reciprocal space investigated.

1.4 Modelling Diffuse Scattering

The general problem of reconstituting atomic positions from a scattering pattern is an inverse problem: possible models that reproduce observed scattering are not certain to be unique. Indeed, it is quite possible for vastly different models to produce qualitatively similar results. An example of immediate relevance to this work is the relaxor $PbMg_{1/3}Nb_{2/3}O_3$, shown by Pasciak *et al.* [24] to have similar diffuse scattering from a variety of different models. Given both the complexity of the functional forms of scattering data and its inherent loss of phase information, analysis of diffuse scattering data can be quite difficult, as the

question of what real-space structure generates the measured reciprocal-space intensities does not have a unique analytical solution. One way to address these difficulties is by simulating data from a crystal with certain correlations and comparing the simulated scattering to that obtained from experiment. While this does not address uniqueness concerns, it may be easier to understand the effects of various types of order when they can be simulated; at the very least, models can be eliminated by showing that they produce scattering that does not match measured intensities. An ideal case study would involve the comparison of experimental data to its analytical forms and to simulated data. Until solutions to structural correlations can be directly derived from data (an unlikely prospect in the near term!), comparisons among experimental data, analytical forms, and simulated data will be useful tools in understanding diffuse scattering. Scattering calculations from simulated crystals in this work have been done using *DISCUS* software [25, 26], which can find scattering from an arbitrary array of atoms with given positions. *DISCUS* also has a simple mixed Monte Carlo routine built-in for structural simulations. By defining equivalent atomic position in the unit cell as well as atom neighborhoods, both chemical short-range order and displacement correlations can be simulated within a model crystal, and the scattering from the model crystal can then be calculated in either a plane or a volume of reciprocal space.

As an example, consider a crystal with a cubic lattice and combine the chemical ordering and size-effect demonstrated earlier. A simulation can quickly provide a qualitative picture of the change in scattering by producing simulated crystals with different $\alpha_{\langle 100\rangle}^{A-B}$, applying the same size-effect potential to each, then calculating the scattering from each (Fig. 1.8). As expected from the $(1-\alpha_{lmn}^{ij})$ term in I_1, increasing chemical short-range order suppresses size-effect scattering, even as the deviations $\langle X_{lmn}^{A-B}\rangle$ remain largely unchanged.

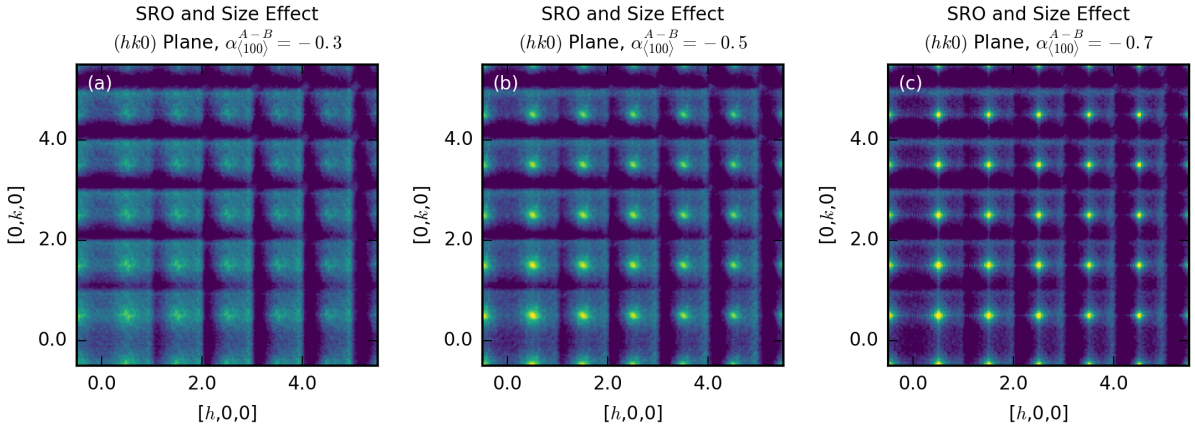

Figure 1.8: A simple 100 $\times$ 100 square atomic lattice with two occupants A and B of equal concentration produces I_1 scattering; the occupants A and B have varying amounts of short-range order. Increasing chemical short-range order suppresses size-effect scattering in this case, due both to the $(1 - \alpha^{ij}_{lmn})$ factor in I_1 and to reduced longer-range displacement correlations.

CHAPTER 2

INTRODUCTION TO FERROELECTRICS AND RELAXORS

An electrically neutral object with separated positive and negative charges is an electric dipole. This dipole is defined by the electric dipole moment $\mathbf{p} = q\mathbf{d}$, the product of the magnitude of the separated charges q and the vector displacement $\mathbf{d}$ between them. A dielectric material is one which is insulating, preventing any major redistribution of electric charge under an applied electric field, and instead develops a bulk electric polarization due to slight displacements of electric charge. A dielectric crystalline material could be viewed as having a dipole moment in each unit cell, with the bulk polarization being the sum of these microscopic dipoles. However, the unit cell is not a unique property of a material; a differently defined unit cell can show different electric polarizations for the same configuration of charges by having different surface charges. This ambiguity in microscopic polarization can be removed by considering the electronic wavefunctions, where polarization can be expressed as an invariant Berry phase independent of unit cell choice; in this picture, polarization is established as a truly quantum phenomenon [28, 29].

2.1 Ferroelectrics and Relaxors

Some definitions of electric crystals can now be made. A pyroelectric crystal is a crystal whose natural unit cell has a finite dipole moment [30]; this microscopic dipole moment adds up to a net polarization of the bulk material. Such an arrangement of atoms severely

Material is this chapter has been adapted with permssion from [27].

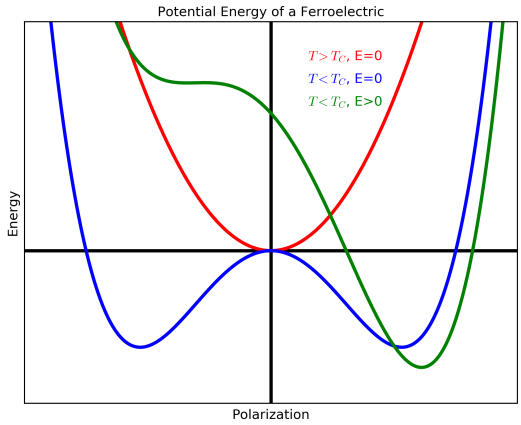

Figure 2.1: Above T_C, a ferroelectric material displays no spontaneous polarization. Below T_C, polarized states become energetically favorable, and an applied electric field can select an individual state.

restricts the possible symmetry of a pyroelectric crystal; only non-centrosymmetric space groups can give rise to this phenomenon. Some materials have no bulk electric polarization at high temperature, but spontaneously polarize upon cooling below a certain temperature. In analogy to ferromagnetism, such materials are called ferroelectric, with the transition temperature T_C called the Curie temperature. Ferroelectrics can also respond to an applied electric field by aligning their polarization direction with that of the applied field (Fig. 2.1). Ferroelectrics typically possess a large dielectric permittivity ϵ, following a Curie-Weiss Law $\epsilon \propto \frac{1}{T-T_C}$ [31]; as the polarization states are distinct but close in potential energy near T_C, there is a large enhancement of ϵ near T_C. The measured permittivity ϵ is independent of the frequency of the applied field.

Ferroelectricity in crystals is inherently tied to crystallographic structure; a crystal described by a point group containing inversion symmetry cannot be ferroelectric, since such a crystal must have $\mathbf{p} = -\mathbf{p}$. The lack of inversion symmetry in ferroelectric crystals also allows such crystals to display piezoelectricity. A piezoelectric material is one where a mechanical stress can induce electric polarization. Piezoelectricity in a material is defined by

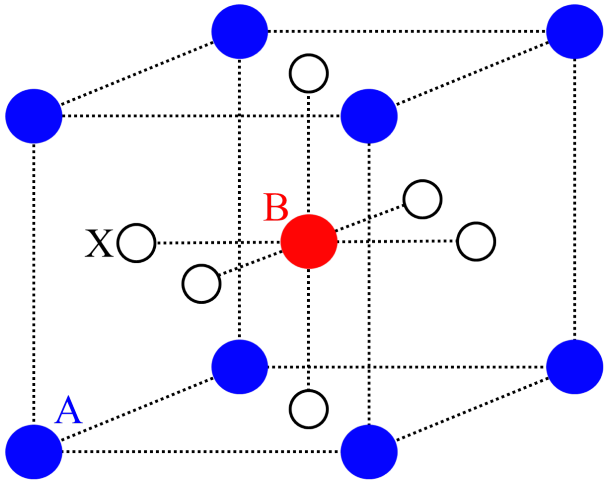

Figure 2.2: The cubic perovskite structure has three crystallographic sites: the A site, at the corners of the unit cell, the B site, at the center, and the X site, on the faces of the cube.

its piezoelectric tensor, d [32], a third-rank tensor which relates the electric displacement $\mathbf{D}$, a first-rank tensor, to the strain σ via

$$D_k = d_{kij}\sigma_{ij}$$

Most elements of d_{kij} will be zero even in strongly piezoelectric materials due to the symmetry. For the materials considered here, the d_{33} component alone (note that the index k is a dummy index), relating a strain parallel to the direction of the applied field, is a good metric for the piezolectric behavior of a material.

Many widely-used ferroelectric materials share a perovskite crystal structure; the lead-based relaxor ferroelectrics (PBRF's) considered in this work are all perovskites. The perovskite structure has a simple chemical formula, ABX_3, with cations occupying the A and B sites and anions (usually but not always oxygen atoms) occupying the X sites (Fig. 2.2).

The simplicity of the perovskite structure is at odds with the complex range of behaviors present in ferroelectric perovskite oxides. The first such material discovered, $BaTiO_3$, does have a paraelectric cubic phase at high temperature. Rather than a single ferroelectric phase

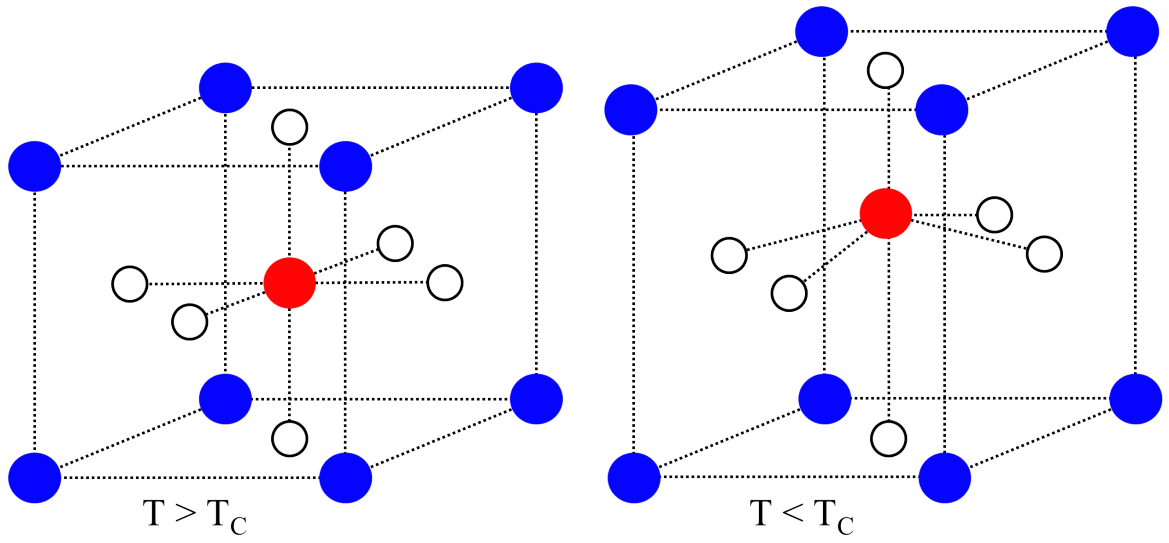

Figure 2.3: Above T_C, lead titanate has an undistorted cubic perovskite structure. Below T_C, one side of the unit cell expands relative to the other two and atoms leave their high-symmetry positions, leading to a net polarization.

below T_C, however, it has multiple phase transitions between distinct ferroelectric phases [7], indicating a more complex picture of ferroelectricity than the simple model proposed above.

A simpler example of a ferroelectric perovskite is lead titanate, $PbTiO_3$, abbreviated to PTO. PTO is paraelectric and cubic above $T_C = 763$ K [33]. Upon cooling below Below T_C, PTO develops ferroelectricity, as atoms leave high-symmetry positions. One axis of the unit cell lengthens with respect to the other two, making the unit cell tetragonal (Fig. 2.3). The large ratio $c/a \approx 1.07$ [34] makes single crystals of PTO prone to cracking upon structural transitions.

Another class of material is the relaxor, best understood in contrast to a ferroelectric. A relaxor does not generate a bulk polarization if sufficiently cooled, but it does have a similar anomaly in its dielectric constant ϵ around a certain temperature. In contrast to a ferroelectric material, where the anomoly in ϵ is sharp in temperature around T_C, in relaxors, this anomaly is broad in temperature around a peak value at temperature $T_m(f)$ and dependent upon the frequency (f) used to test the dielectric response [35]. One could

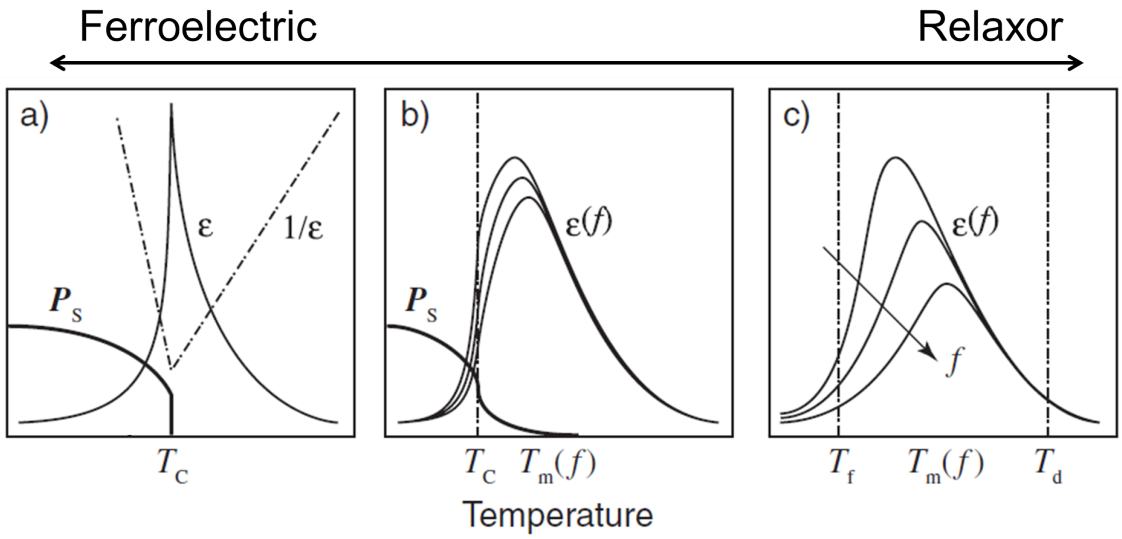

Figure 2.4: (a) A classic ferroelectric with a Curie temperature T_C has a sharp, frequency-independet anomaly in permittivity ϵ. By contrast, a relaxor (c) has a broad anomaly in ϵ;the temperature $T_m(f)$ at which ϵ is peaked is temperature dependent. These behaviors can be mixed (b). Figure adapted from [36]. ©2006 The Physical Society of Japan.

quantify the degree of relaxational character in a material by comparing the change in $T_m(f)$ with frequency; the larger the change, the more relaxational the character of the material. Measurements of optical refractive index in relaxors show evidence for local polar distortions where there is no bulk polarization [8]; this local polar behavior can persist up to a temperature T_d, called the Burns temperature. This indicates that relaxors, like ferroelectrics, have a local polar structure; unlike ferroelectrics, this local order does not persist across the bulk of a sample.

If there is a canonical relaxor, it is $PbMg_{1/3}Nb_{2/3}O_3$, referred to as PMN [4,37]. PMN is also a perovskite oxide, but has two possible B site occupants, Mg^{2+} and Nb^{5+}. PMN retains its high-temperature cubic structure when cooled, but displays an increasing Debye-Waller factor as temperature decreases [38]; as this is not due to increasing thermal excitement, it likely indicates increasing deviation of atoms from equilibrium sites unrelated to the population of phonons.

2.2 PMN-xPT and Related Systems

Numerous relaxor and ferroelectric systems are found among perovskites oxides with lead on the A sites; such a material is referred to as lead-based relaxor ferroelectric (PBRF). PTO and PMN share a perovskite structure and many of the same constituent atoms, only differing in the atom occupying the B site at the center of the O_6 octahedra. The two materials can be mixed in a solid solution with PTO fraction x, most correctly named (1-x)$PbMg_{1/3}Nb_{2/3}O_3$-$x$$PbTiO_3$. This is frequently shortened to PMN-xPT, with x as a percentage PTO (e.g, 0.7$PbMg_{1/3}Nb_{2/3}O_3$-0.3$PbTiO_3$ is referred to as PMN-30PT); this work will use this convention.

PMN-xPT is something of a model system for relaxor ferroelectrics, with a rich structural and behavioral dependence on temperature and concentration. Near the extremes of concentration, the system predictably behaves like the nearest end member. However, near $x = 0.3$, the system exhibits new behavior. There is no sharp first-order phase transition from a PMN-like system to a PTO-like system. Instead, the system displays entirely different behavior over a range of x. This wide intermediate region is referred to as the morphotropic phase boundary (MPB). Near the MPB, the piezolelectric properties of the system are greatly enhanced, with d_{33} orders of magnitude above that of the end members.

Fig. 2.5(a) illustrates our current understanding of how the average symmetry, which governs the long-range polar (ferroelectric) order of single crystal PMN-xPT, evolves with composition and temperature [39]. The low-temperature structure transforms from non-ferroelectric, cubic symmetry at $x = 0$ [38, 41] to highly-strained ferroelectric, tetragonal symmetry at $x = 100$ via two different monoclinic space groups: Cm (which is nearly indistinguishable from rhombohedral $R3m$) and Pm.

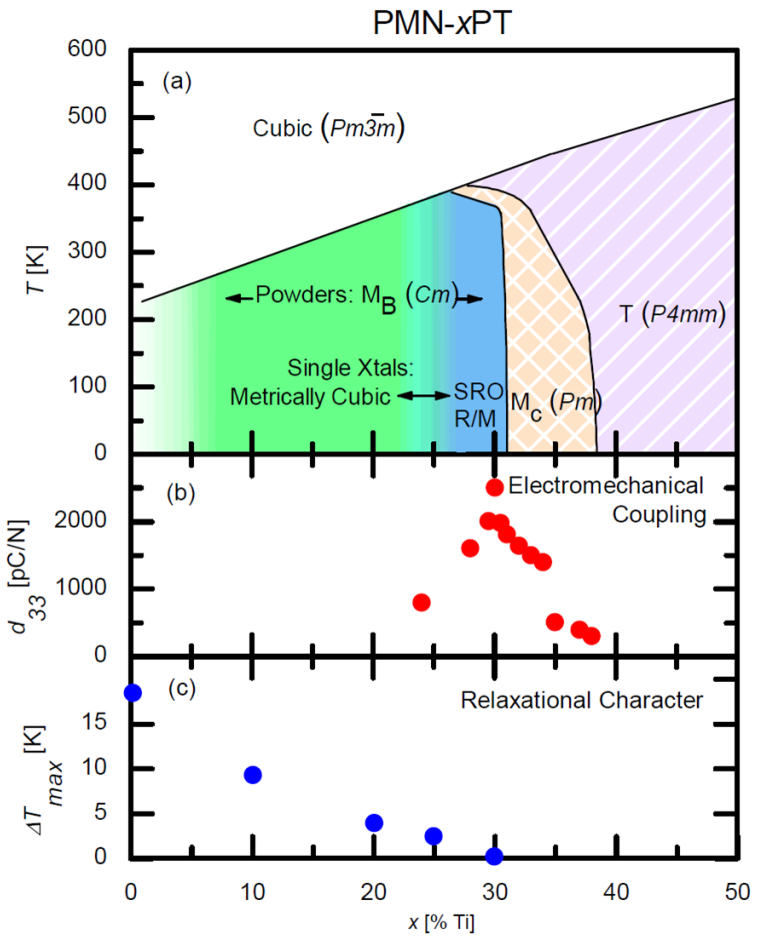

Figure 2.5: (a) The structure of PMN-xPT has a significant dependence on doping and temperature, with different kinds of probes sometimes showing different structures in the Ti-poor relaxor region. Figure adapted from [39]. (b) Piezoelectric coefficient d_{33} as a function of doping. d_{33} is maximized near the morphotropic phase boundary. (c) Relaxational character of PMN-xPT as a function of x. Data was collected and adapted from [40].

Relaxational properties also display a range of behavior across the phase diagram of PMN-xPT. PMN ($x = 0$) is generally discussed as a canonical 'relaxor,' a material that is distinguished by an unusually broad and rounded maximum in dielectric permittivity at a strongly frequency-dependent temperature T_{max} [4, 37]. The frequency-dependent shift in T_{max}, defined as $\Delta T_{max} = T_{max}(10^6 \text{ Hz}) - T_{max}(10^2 \text{ Hz})$, is approximately 24 K for PMN [40, 42]. However, as first elucidated by Grinberg *et al.* [40] and reproduced in Fig. 2.5(c), ΔT_{max}, and hence the diffusive character, gradually vanishes with x as the system changes from relaxor-like to ferroelectric-like. Most importantly, the relaxor character disappears at approximately the same composition at which the MPB is reached and where the electromechanical response is maximal. The compositional dependence of the piezoelectric coefficient d_{33}, which relates the strain to an applied electric field, is adapted from [43] and presented in Fig. 2.5(b); this shows that the electromechanical properties are poor for both end-members but anomalously large close to the monoclinic Pm phase that borders the tetragonal phase at a morphotropic phase boundary (MPB) near $x \approx 30$. Distinguishing between these two properties and discovering how they are linked to each other remains an important question in understanding PMN-xPT.

A frequently employed model for relaxor behavior consists of nano-scale ferroelectric domains, or polar nanoregions (PNR) [4, 8, 44–46] that are embedded in a non-ferroelectric matrix, and it has been argued that these PNR strongly influence the dielectric permittivity [47, 48] and enhance the electromechanical properties [49–51]. However, this 'raisins-in-the-cake' picture is inconsistent with competing models that instead implicate a large number of low-energy domain walls arising from nanoscale variations in the polar displacement vectors [52,53]. Other researchers have highlighted the importance of chemical short-range order [54], competing antiferroelectric and ferroelectric interactions [55], or contrasting ferroelectric tendencies of different cations occupying crystallographically equivalent sites [56] - all of which influence local atomic displacements and material properties. PBRFs thus represent a

valuable platform for testing new experimental methodologies being developed to determine local order and correlate it to material performance.

2.3 Diffuse Scattering from PMN-xPT and Proposed Models

Diffuse scattering, measured in neutron and x-ray scattering experiments, is the classic signature of local ordering in materials, and it has been well-documented in PBRFs. The diffuse scattering that has attracted the most attention by far is the "butterfly" scattering surrounding Bragg peaks. This is generally characterized as rod-like, centered at Bragg reflections, and oriented along $\langle 110 \rangle$ [4, 45, 57, 58], forming butterfly-shaped patterns around $h00$ peaks, 'cigar'-shaped patterns around $hh0$ peaks, and some mixture of the two around other peaks. This 'butterfly'-shaped diffuse scattering has been associated with ferroic order, relaxor behavior, or both [59, 60]. This scattering can be affected by an applied electric field [61], strongly indicating a connection to ferroic properties. As yet, there is still no consensus in the literature on a correct physical interpretation of the underlying local order or how it influences material properties. Models of this feature have been based on PNR [45,58,62–65], oriented polar domain walls [66], polar correlations between chemically-ordered nanoregions [54], Huang scattering [67], thermal-like diffuse scattering [68], or a homogeneous random network of anisotropically coupled dipoles [69]. Diffuse scattering is also observed at high temperature [63] without being well-characterized; it has been noted that the low-temperature scattering fits into the high-temperature scattering as a lock into a key.

In addition, diffuse scattering centered on the M points $\frac{1}{2}(2h+1, 2k+1, 2l)$ (see Fig. 1.2)of the Brillouin zone boundaries has been observed in PMN and attributed to antiferrodistortive displacements of Pb cations [70]. Unusual neutron inelastic scattering from highly-damped phonons is observed at these M points and has been attributed to soft antiferroelectric

modes [71] that soften to produce broad elastic peaks at low temperature. Diffuse peaks centered on the **R** points $\frac{1}{2}(2h+1, 2k+1, 2l+1)$ have also been reported; these have been attributed to ordering of Mg^{2+} and Nb^{5+} ions [70, 72].

Without energy resolution, diffuse scattering can reflect both static and dynamic displacements within the lattice; as both types are relevant in PMN-xPT in different regimes, this can lead to considerable confusion. It is noteworthy that diffuse scattering from PMN-xPT increases with decreasing temperature, and neutron spin echo experiments have shown this scattering to be elastic [73]. While there are many interesting dynamics in PMN-xPT relating to soft phonon modes, the low-temperature structure and diffuse scattering is related to static displacements. Further complicating interpretation of diffuse scattering from PMN-xPT is evidence of a skin effect [74], whereby scattering from these materials shows a marked dependence on the incident energy of the scatterer. This suggests that the surface of these materials may behave differently from the bulk, making it important to determine if experiments are providing a true average of the material.

CHAPTER 3

DIFFUSE SCATTERING FROM PMN-xPT

Despite the significant body of work already produced on PMN-xPT, many fundamental questions about the system remain unresolved. Given the likely role of short-range order and local correlations in the system, it is natural to apply modern methods of measuring diffuse scattering to PMN-xPT. These methods (outlined in Chapter 1.3) provide both a larger, more complete picture of scattering from a given composition at a given temperature and sufficient throughput to obtain these pictures at many different compositions and temperatures. By tracking diffuse scattering and how it changes with temperature and composition, it can be linked to bulk properties, thus showing the connection between various forms of local order and their effects on bulk materials. A phase diagram of PMN-xPT is shown in Figure 3.1 with markers placed for the different scattering experiments performed.

Table 3.1: PMN-xPT crystals measured for neutron diffuse scattering using Corelli, with actual compositions determined by prompt gamma activation analysis (PGAA).

Crystal	Mass (g)	Nominal %Ti	Actual % Ti
PMN	0.651	0	0
PMN-20PT	1.02	20	21.7
PMN-30PT	0.725	30	28.8
PMN-35PT	0.136	35	33.0
PMN-40PT	0.638	40	39.8
PMN-50PT	0.275	50	48.5

Material is this chapter has been adapted with permssion from [27].

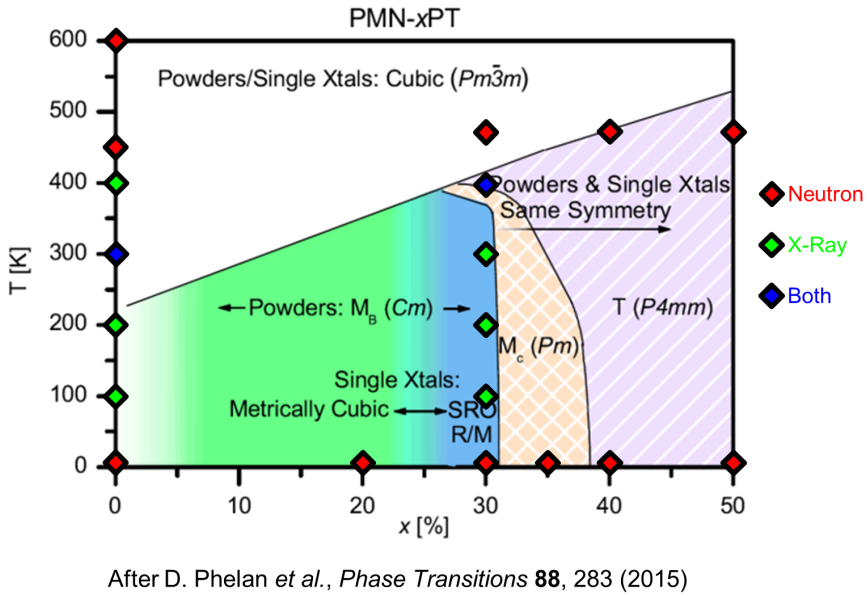

After D. Phelan *et al.*, *Phase Transitions* **88**, 283 (2015)

Figure 3.1: Diffuse scattering from PMN-xPT was measured at a variety of Ti concentrations and temperatures spanning the phase diagram.

3.1 Neutron Scattering Experiments

Neutron diffuse scattering measurements were made on a series of PMN-xPT crystals using the instrument *Corelli* at the Spallation Neutron Source. The crystals ranged in total mass from 0.136 g to 1.01 g; to normalize the scattering among the different crystals, each was measured using *Corelli* with the incident beam shutters completely open so as to completely bathe the crystal in the incident beam. Bragg intensities from this measurement were then taken and normalized to measured mass to establish relative Bragg intensity per scatterer for each crystal; normalization factors for diffuse scattering data were then extrapolated from Bragg peaks and applied to the diffuse scattering data sets. Data were processed in MANTID using Corelli's cross-correlation algorithm, which ensured that inelastic scattering is filtered out. Prompt gamma activation analysis (PGAA) was performed at the NIST Center for Neutron Research to determinue the actual composition of each sample; as shown

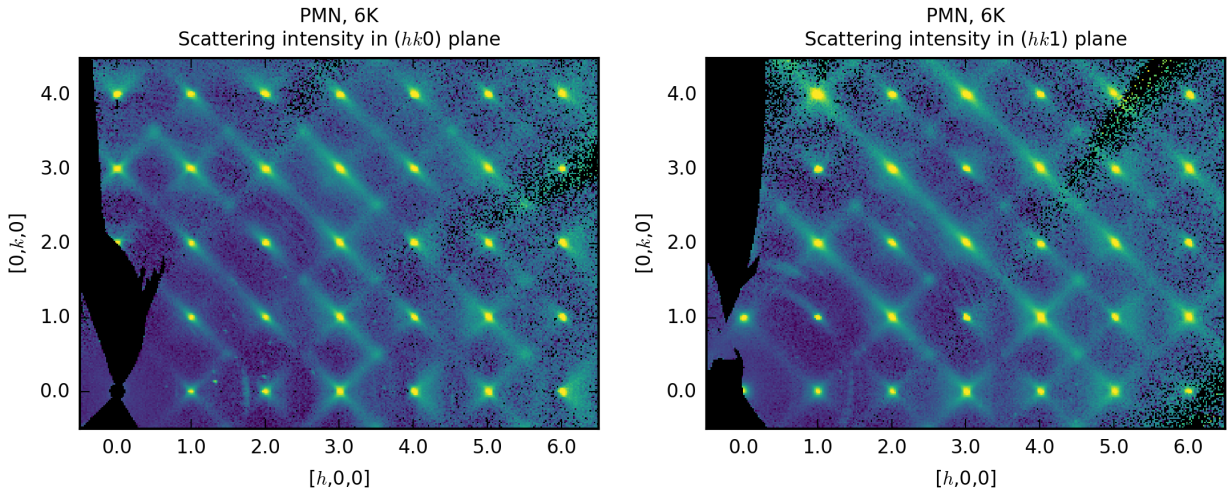

Figure 3.2: Diffuse scattering from PMN at 6 K, shown in the $l = 0$ (left) and $l = 1$ (right) planes.

in Table 3, actual Ti concentration was close to the nominal concentration for each sample, and samples will be referred to by their nominal concentration for the remainder of this work.

3.1.1 PMN

A sample of pure PMN with mass 0.67 g was examined at 6 K and again at 300 K, with about 8 hours of measurement over an angular range of 120°. The sample was mounted on a small aluminum post using superglue, limiting maximum temperature; this post was itself masked using cadmium. Given the low $T_m(f)$ of ≈220 K for PMN, this was thought to be sufficient to capture two different areas of behavior.

At 6 K, examination of the $l = 0$ and $l = 1$ (Fig. 3.2) planes show significant diffuse scattering surrounding each Bragg peak. This scattering emanates from the central peak along ⟨110⟩ directions. Compared to the data found in previous neutron scattering studies,

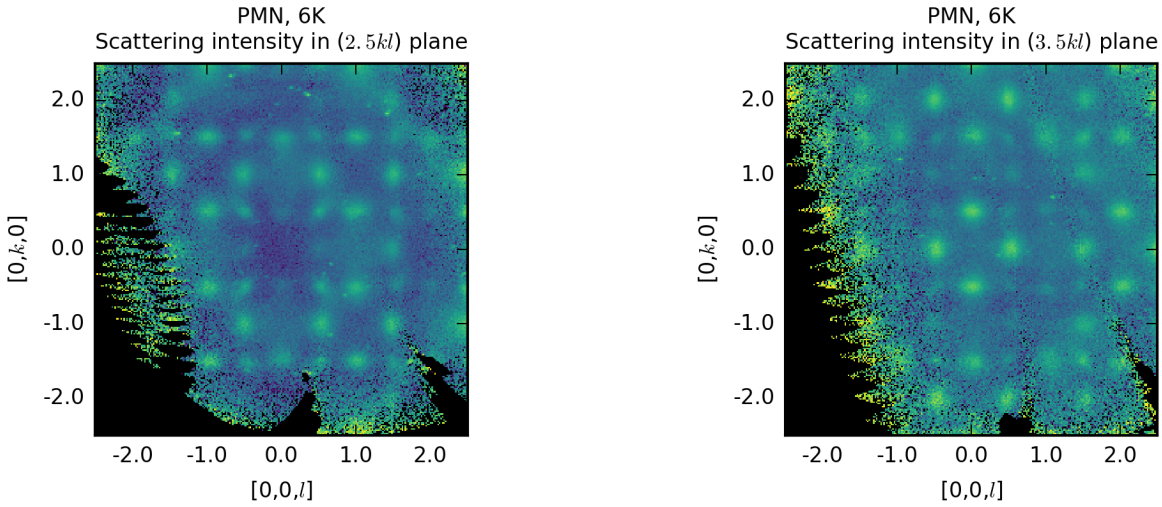

Figure 3.3: Diffuse scattering from PMN at 6 K, shown in the $h = 2.5$ (left) and $h = 3.5$ (right) planes.

there is an obvious asymmetry between the low-$|\mathbf{Q}|$ and high-$|\mathbf{Q}|$ diffuse scattering around some of the Bragg peaks. Also visible in the $l = 0$ and $l = 1$ planes are broad peaks at certain $\mathbf{M}$ points in the Brillouin zone. These peaks are better visualized in the $l = 2.5$ and $l = 3.5$ planes (Fig. 3.3), where they can be seen alongside slightly sharper peaks on the $\mathbf{R}$ points.

Later analysis raised questions about the behavior of certain components of diffuse scattering at higher temperatures. To this end, further experiments were performed with the sample affixed to an aluminum plate with aluminum wire and surrounded by an aluminum heat shield. The additional aluminum background was necessary to achieve higher temperatures and keep the sample stable at these temperatures. In this configuration, scattering was measured at 300 K, 450 K, 600 K, and 700 K. These higher-temperature measurements used less time and covered less of reciprocal space than the previous measurements, but important information regarding specific, localized features was still extracted from these datasets.

Higher-temperature scans covered less reciprocal space but show the clear suppression of the scattering around the Bragg peaks (Fig. 3.4 (a-d)), as well as the scattering near M points (Fig. 3.4 (e-h)). Some R points appear relatively unchanged from 300 K to 700 K, while others become less intense (this is further discussed in Ch. 3.3.4).

3.1.2 PMN-20PT

A sample of PMN-xPT with nominal $x = 0.2$ and total mass 1.01 g was measured at 6 K. The sample was suspended from an aluminum post with a binary epoxy allowing for higher-temperature measurements, with the post shielded by a band of gadolinium. While large, this sample consisted of a main crystal and a few smaller crystallites. The normalization factor for this sample was further corrected by comparing the intensity of Bragg peaks from the main sample to that of its crystallites; 84% of the total Bragg intensity coming from the main peak, and the effective mass of this sample is considered to be 0.84 g for the purpose of normalization. While data from this sample is of sufficient quality to highlight overall trends, more detailed modelling would require an impractical amount of data correction.

Comparing diffuse scattering from PMN-20PT to the diffuse scattering from PMN reveals a few obvious changes. As seen in Fig. 3.5, the extended 'butterfly' shapes centered on Bragg peaks are more concentrated to the zone center in PMN-20PT and do not extend as far across the Brillouin zone as they do in PMN. Similar asymmetry between low-$|\mathbf{Q}|$ and high-$|\mathbf{Q}|$ halves is observed, but manifests differently around different peaks – for example, the 300 peak appears mostly symmetric in PMN but has much more intensity on the low-$|\mathbf{Q}|$ side in PMN-20PT. Scattering at the M and R points is almost impossible to discern by eye in these images; while later analysis will show that small remnants of these peaks can be found, they are indeed greatly suppressed for this sample compared to PMN.

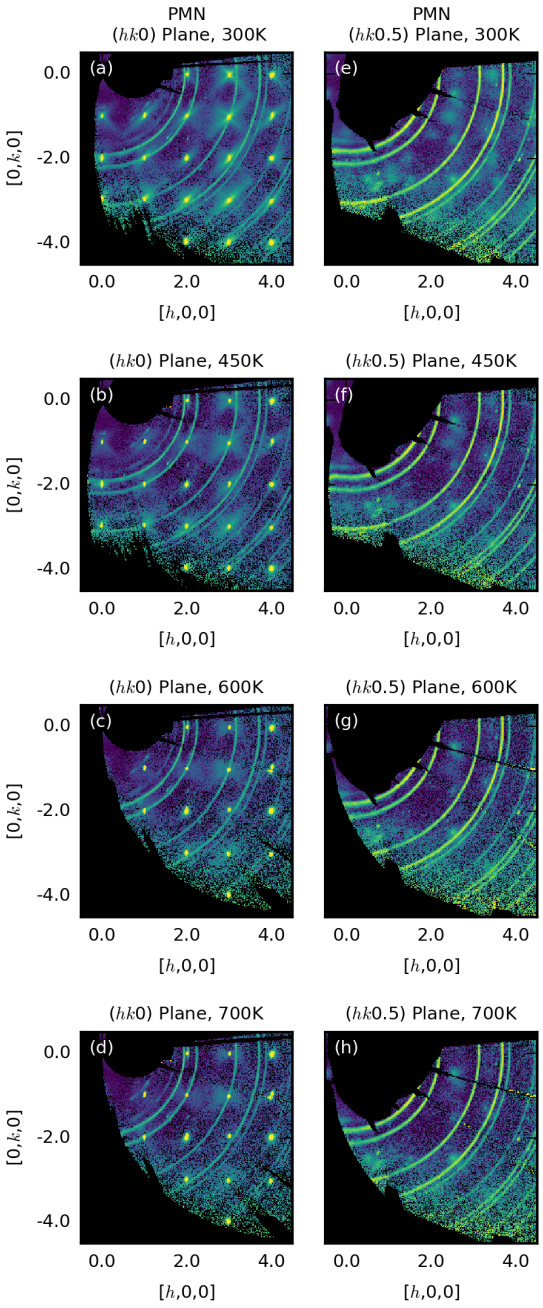

Figure 3.4: Diffuse scattering from PMN at 300 K, 450 K , 600 K, and 700 K, shown in the $l = 0.0$ (panels (a-d)) and $l = 0.5$ (panels (e-h)) planes.

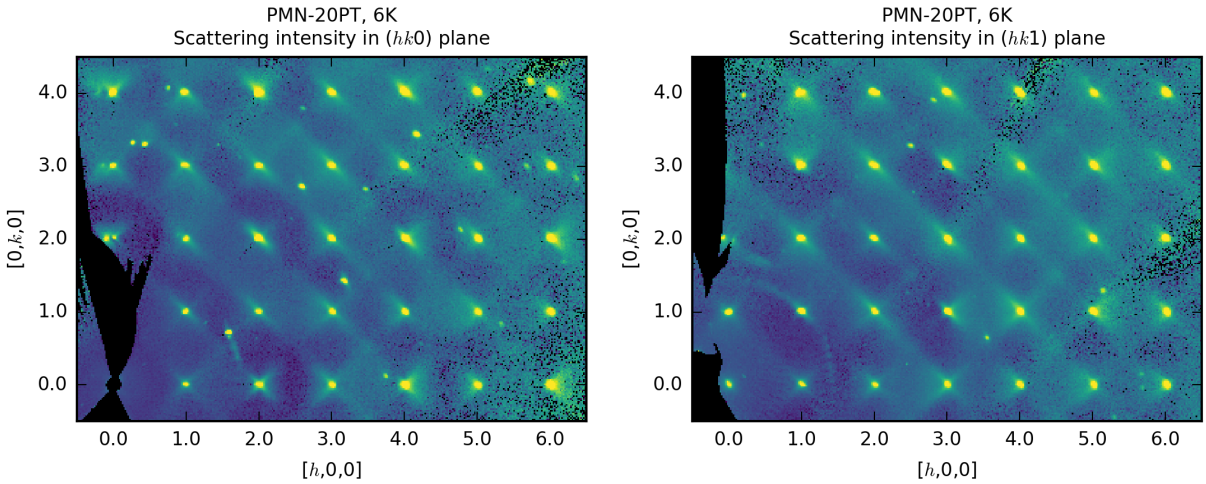

Figure 3.5: Diffuse scattering from PMN-20PT at 6 K, shown in the $l = 0$ (left) and $l = 1$ (right) planes.

A new feature between the Bragg peaks is clear in this data – very broad scattering spanning the space between certain zone centers, e.g. the 300 and 400. This scattering is best viewed in half-integer planes as in Fig. 3.6. The strong M point scattering observed in PMN is weakened and coincides with this broad scattering, showing up on the corners of the diamond-like shapes formed in the half-integer planes; this feature is thus roughly octahedral in three dimensions, at least in Brillouin zones close to $\langle h00 \rangle$. The R point scattering is almost gone entirely.

3.1.3 PMN-30PT

Diffuse scattering from a sample of PMN-xPT with nominal $x = 0.3$ and mass 0.725 was measured using Corelli at three temperatures: 6 K, the base temperature for Corelli using the CCR; 390 K, close to the paraelectric transition temperature for this composition; and 470 K, well above the transition temperature. The sample was mounted with high-temperature

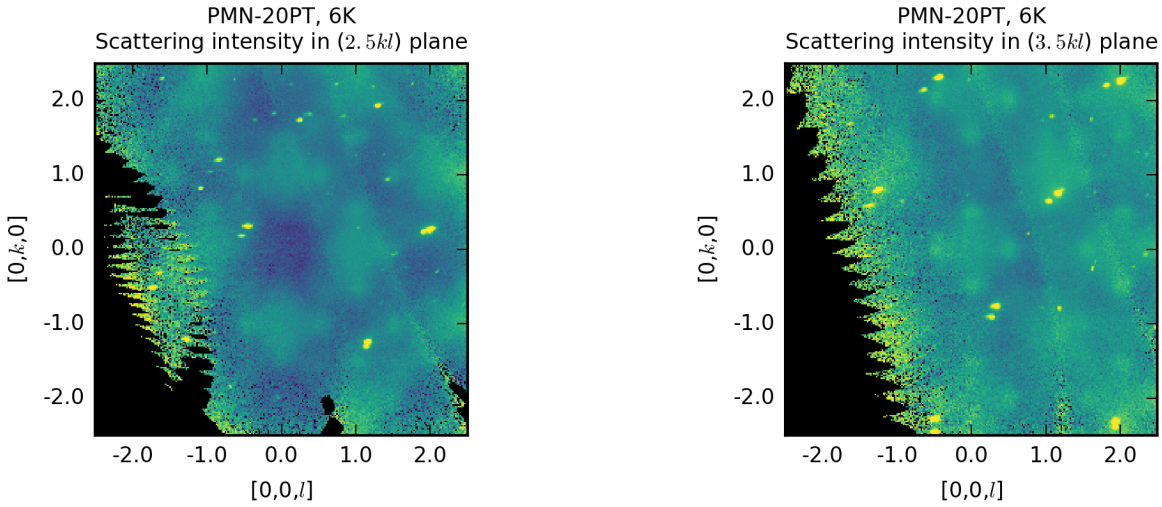

Figure 3.6: Diffuse scattering from PMN-20PT at 6 K, shown in the $h = 2.5$ (left) and $h = 3.5$ (right) planes.

epoxy on an aluminum pin; a boron nitride shield removed any scattering from the pin at the expense of adding a weaker background of its own. This sample has a Ti concentration placing it close to the morphotropic phase boundary and thus has a strongly enchanced d_{33}.

At 6 K, examination of the $l = 0$ and $l = 1$ planes shows a continuation of the trend from PMN to PMN-20PT. Diffuse scattering around the Bragg peaks appears more concentrated near $\mathbf{q} = 0$, and superlattice reflections are not clearly visible in these planes. As in PMN-20PT, broad scattering spans the region of reciprocal space between certain zone centers; this scattering is particularly visible in the $l = 2.5$ and $l = 3.5$ planes (Fig. 3.8). Scattering at the M point is still visible at the corners of the 'diamonds' in these planes.

With the temperature increased to 470 K, which is above T_C, the concentrated scattering around the Bragg peaks is weakened considerably (Fig. 3.9). While the broad scattering between Bragg peaks remains visible (Fig. 3.10), the M point peaks on corners are suppressed entirely. The broad scattering itself appears mostly unchanged, particularly in zones close to

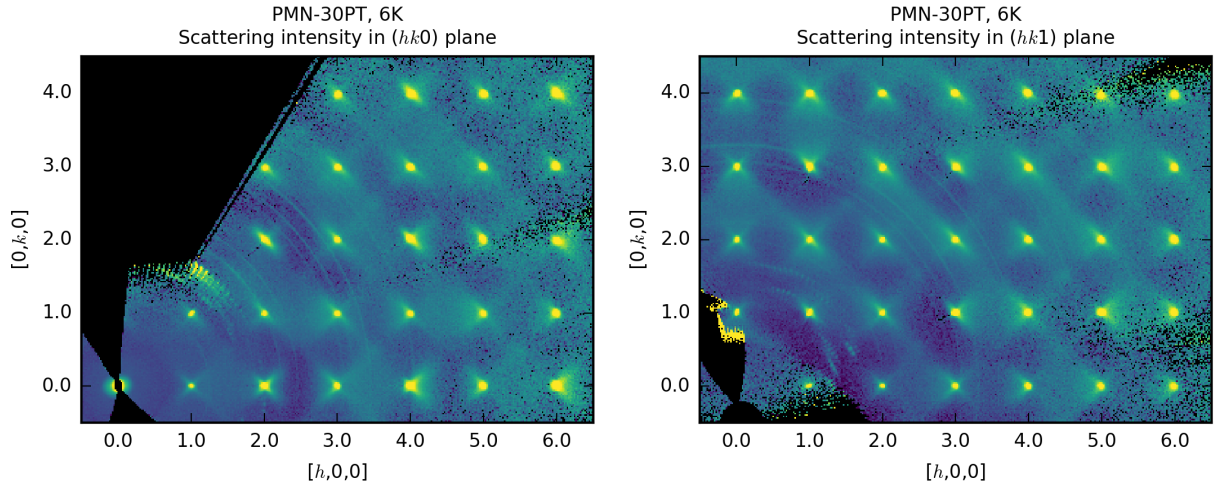

Figure 3.7: Diffuse scattering from PMN-30PT at 6 K, shown in the $l = 0$ (left) and $l = 1$ (right) planes.

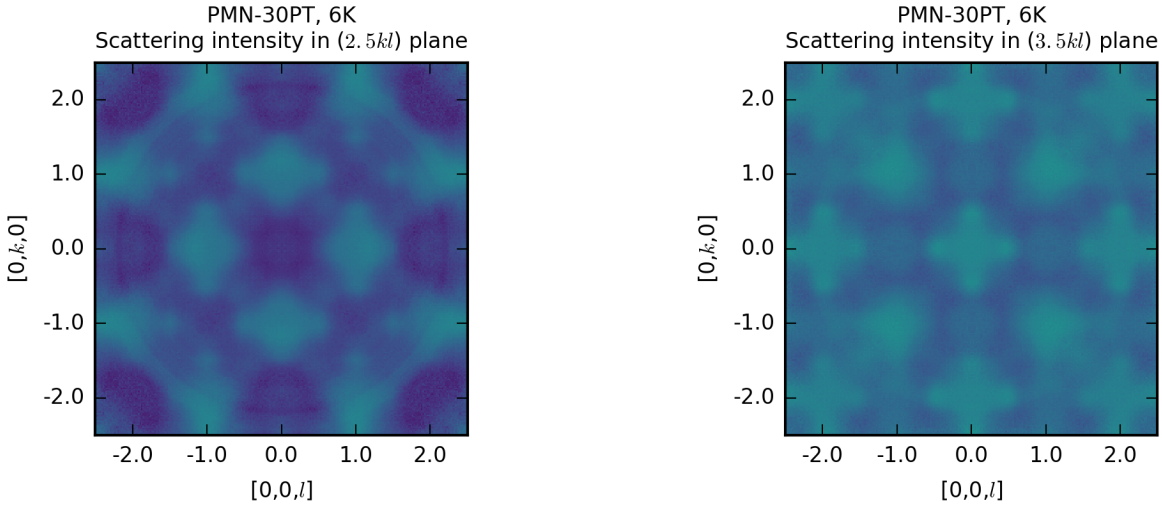

Figure 3.8: Diffuse scattering from PMN-30PT at 6 K, shown in the $h = 2.5$ (left) and $h = 3.5$ (right) planes. These data have been symmetrized to fill gaps in coverage and better portray the pattern of scattering.

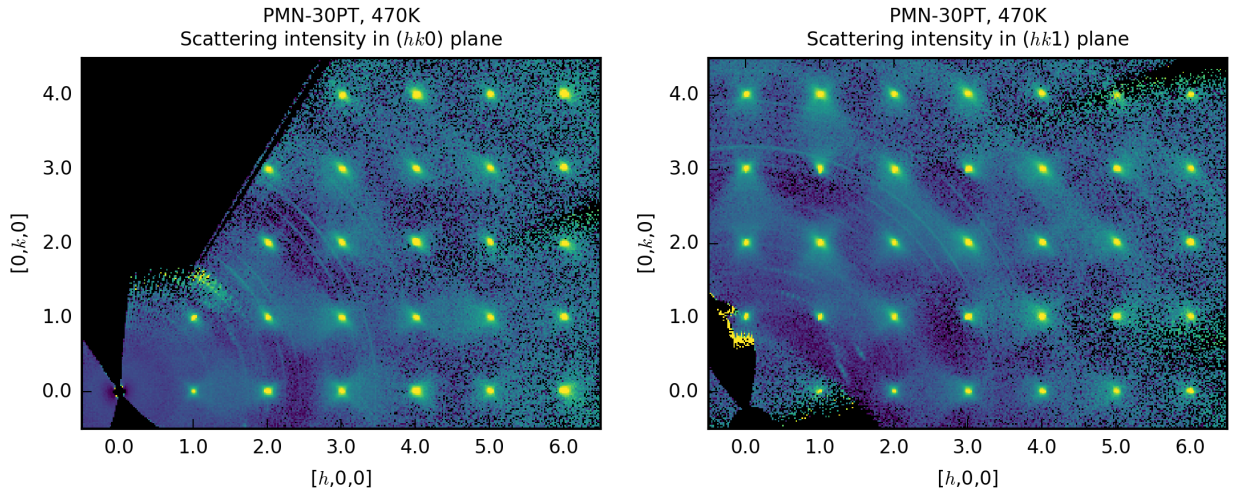

Figure 3.9: Diffuse scattering from PMN-30PT at 470 K, shown in the $l = 0$ (left) and $l = 1$ (right) planes.

$\langle h00 \rangle$, with some minor details appearing to change and the feature itself becoming slightly less distinct.

3.1.4 PMN-35PT

A sample of PMN-xPT with nominal $x = 0.35$ and mass 0.136 g was measured at 6 K. This sample used the same gadolinium-masked mount as the x = 0.2 sample. The measured Ti concentration of this sample places it within the MPB (see Fig. 3.1).

Trends of changes in the diffuse scattering observed in previous samples are continued here. The scattering near Bragg peaks continues to appear more concentrated toward $\mathbf{q} = 0$, and little remnant of the M-point scattering can be seen, while the broad, zone-spanning scattering continues to be prominent. Unfortunately, scans at higher temperatures were not completed for this sample.

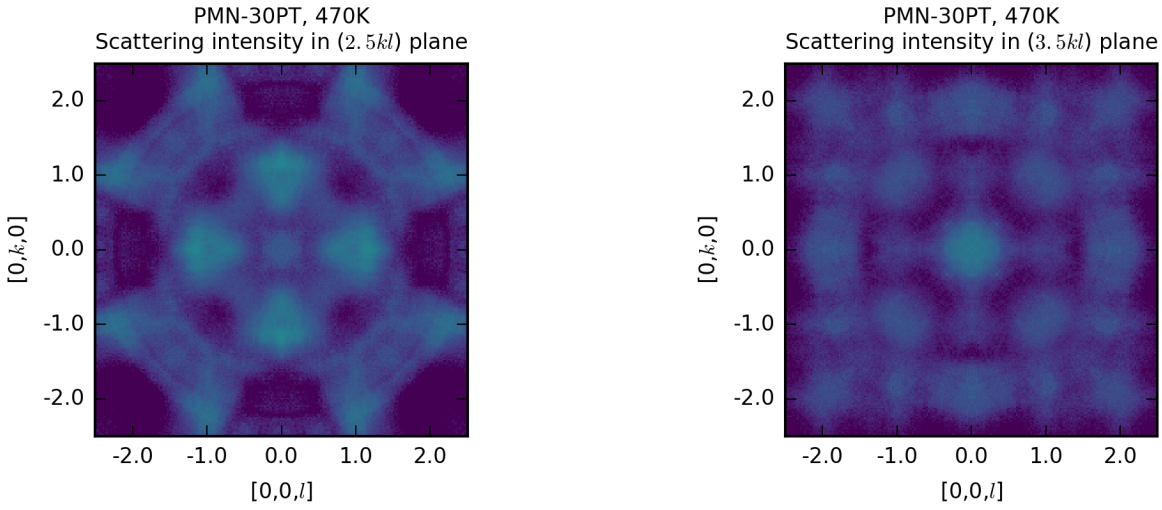

Figure 3.10: Diffuse scattering from PMN-30PT at 470 K, shown in the $h = 2.5$ (left) and $h = 3.5$ (right) planes. These data have been symmetrized to fill gaps in coverage and better portray the pattern of scattering.

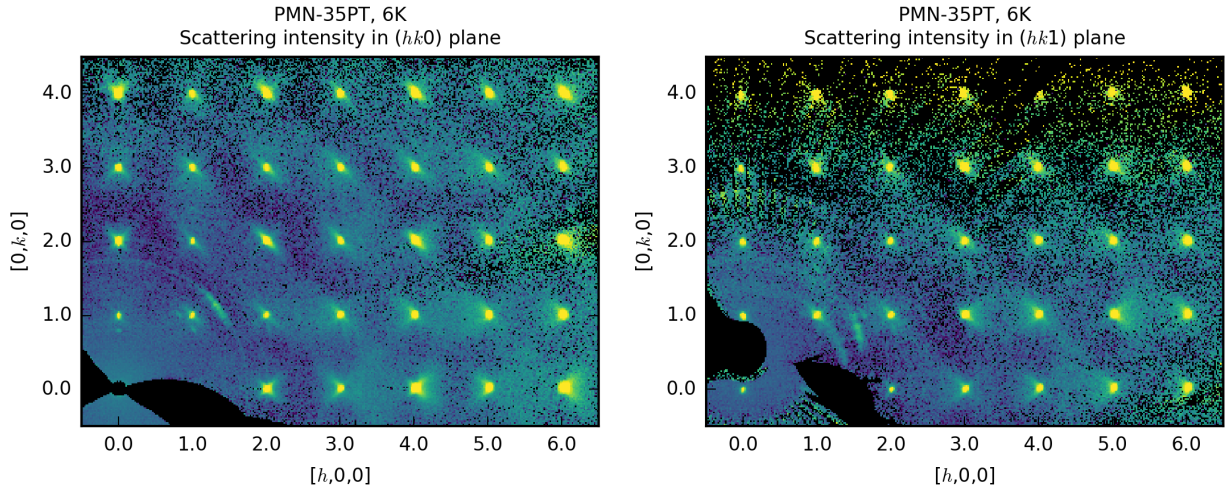

Figure 3.11: Diffuse scattering from PMN-35PT at 6 K, shown in the $l = 0$ (left) and $l = 1$ (right) planes.

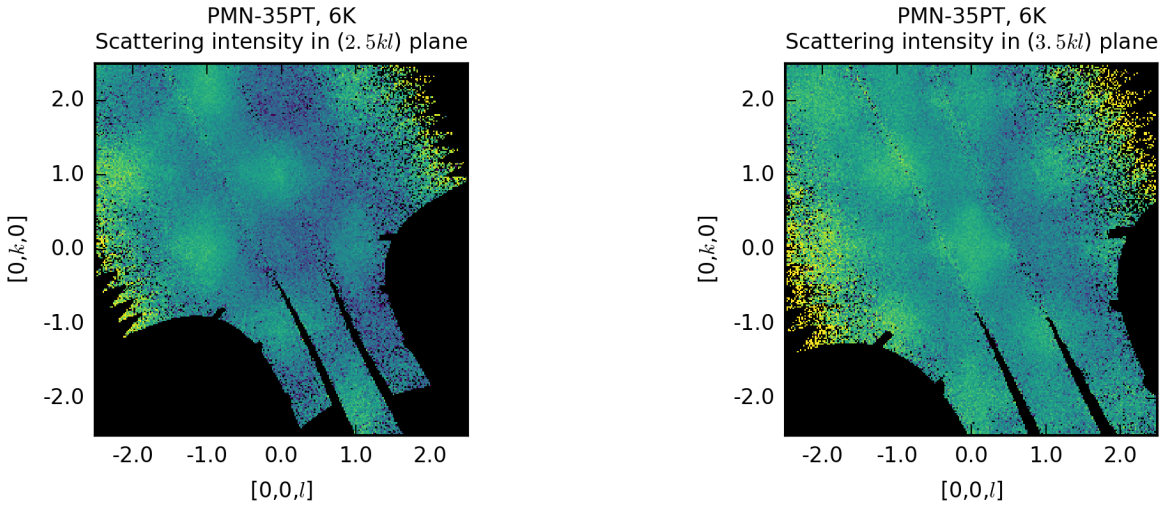

Figure 3.12: Diffuse scattering from PMN-35PT at 6 K, shown in the $h = 2.5$ (left) and $h = 3.5$ (right) planes.

3.1.5 PMN-40PT

A sample of PMN-xPT with nominal x = 0.40 and mass 0.638 g was measured at 6 K and 475 K. This sample used the same gadolinium-masked mount as the x = 0.2 sample.

This sample is clearly on the Ti-rich, ferroelectric side of the phase diagram, so some change is diffuse scattering is expected. Observation of the $l = 0$ and $l = 1$ planes (Fig. 3.13) at 6 K show that the scattering around the Bragg peak is now suppressed. As the system is now tetragonal at low temperature, there is some indication of Bragg peak splitting due to the presence of three different tetragonal orientations. The broad scattering between the Bragg peaks is still present, and is particularly noticeable in the $h = 2.5$ and $h = 3.5$ planes (Fig. 3.14).

At 475 K, which is above T_C for this composition and where the sample is in a cubic, paraelectric state, the Bragg peaks are sharp and unsplit (Fig. 3.15). However, the broad scattering between Bragg peaks remains (Fig. 3.16). Background is actually diminished

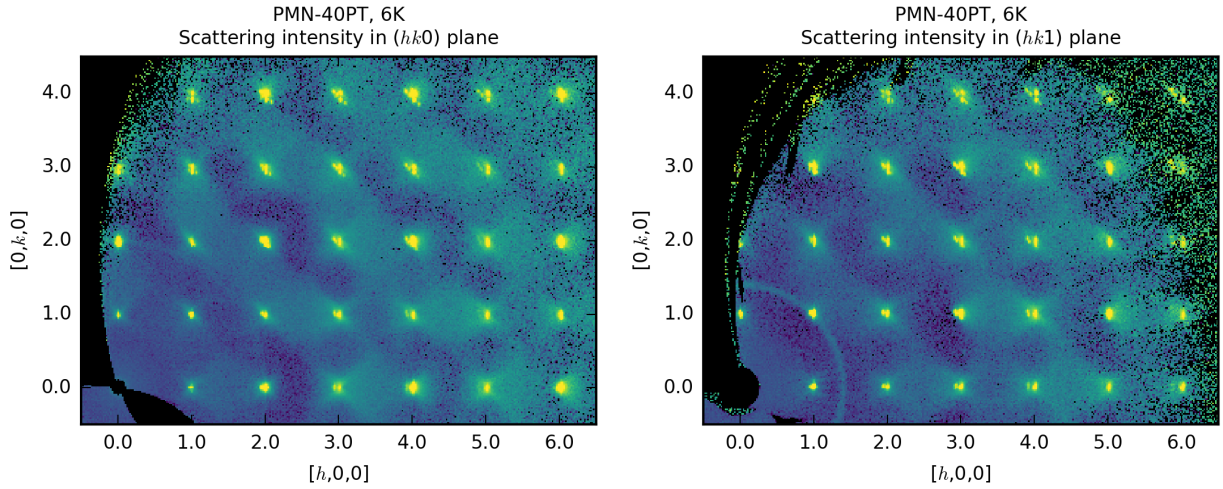

Figure 3.13: Diffuse scattering from PMN-40PT at 6 K, shown in the $l = 0$ (left) and $l = 1$ (right) planes.

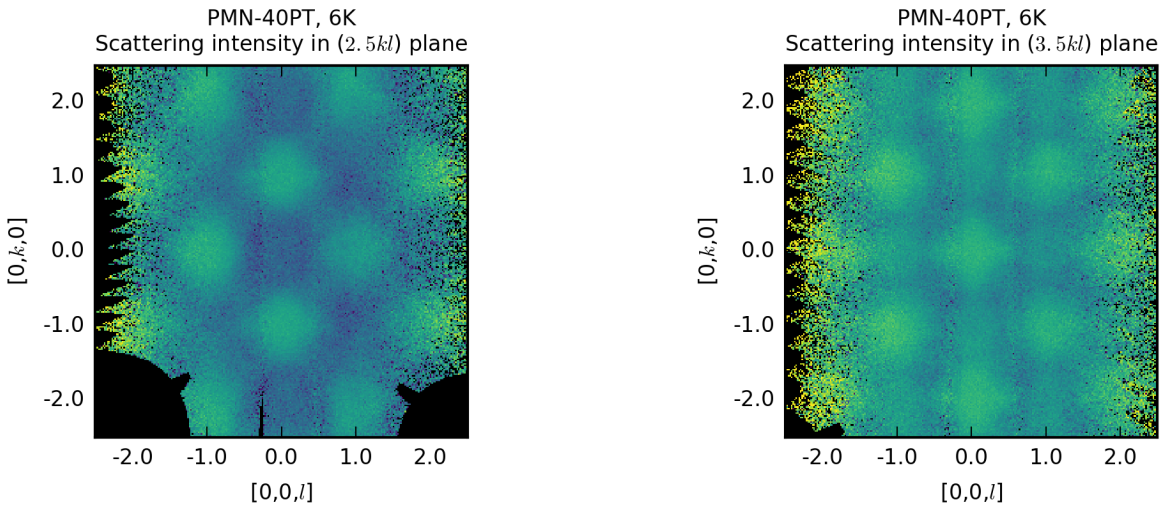

Figure 3.14: Diffuse scattering from PMN-40PT at 6 K, shown in the $h = 2.5$ (left) and $h = 3.5$ (right) planes.

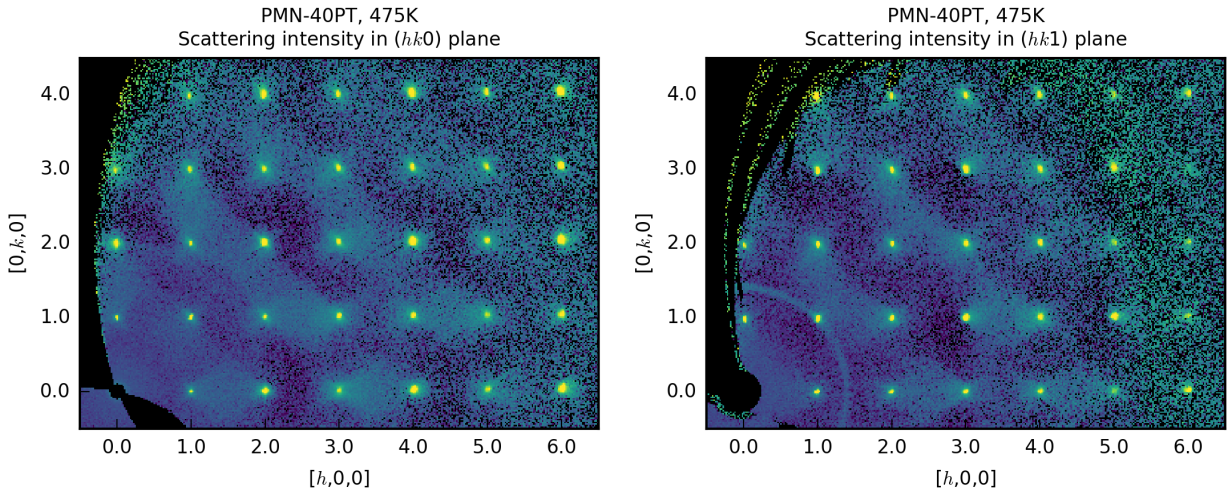

Figure 3.15: Diffuse scattering from PMN-40PT at 475 K, shown in the $l = 0$ (left) and $l = 1$ (right) planes.

at high temperature; this may be a result of background sources producing more inelastic and less elastic scattering and thus more of the background being filtered out by *Corelli*'s cross-correlation chopper.

3.1.6 PMN-50PT

A sample PMN-xPT with nominal $x = 0.50$ and mass 0.235 g was measured at 6 K and 480 K. This sample used the same gadolinium-masked mount as the $x = 0.2$ sample.

At 6 K, the diffuse scattering features strongly suppressed in PMN-40PT are now completely gone. At low temperature, no butterfly scattering or peaks at M or R points can be observed at all (Fig. 3.17), although the broad scattering centered on zone boundaries remains (Fig. 3.18). Bragg peaks are both split into tetragonal domains and strongly distorted, with the peaks both split in **Q** and extended along the rocking curves, a likely result of

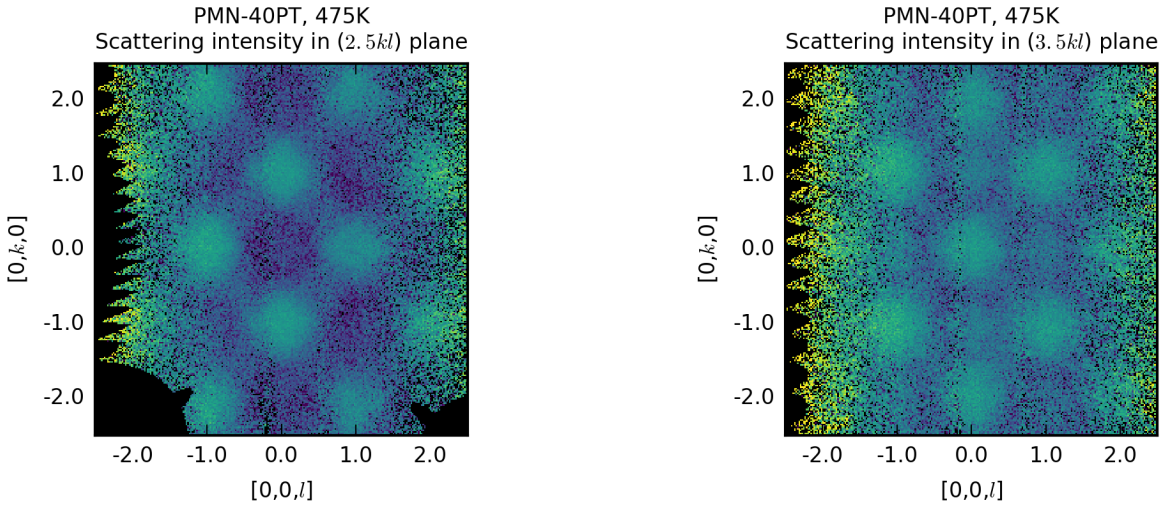

Figure 3.16: Diffuse scattering from PMN-40PT at 475 K, shown in the $h = 2.5$ (left) and $h = 3.5$ (right) planes.

different ferroelectric domains being present in the crystal and the strong strain that must exist at the boundaries between these domains.

At 480 K, relatively narrow Bragg peaks are observed (Fig. 3.19), as the sample is now above T_C and in a cubic phase. Similar to PMN-40PT, the broad zone-boundary-centered scattering remains visible (Fig. 3.20), though a reduced background reduces the absolute intensity in areas covered by this broad scattering, making this feature appear weaker but clearer at high temperature.

3.2 X-ray Scattering Experiments

As a complement to the neutron measurements, x-ray diffuse scattering from PMN and PMN-30PT was measured at beamline A2 of CHESS using the continuous rotation method outlined in Chapter 1.3. Previously published x-ray and neutron measurements of diffuse scattering were largely harmonious, reporting very similar diffuse scattering features around

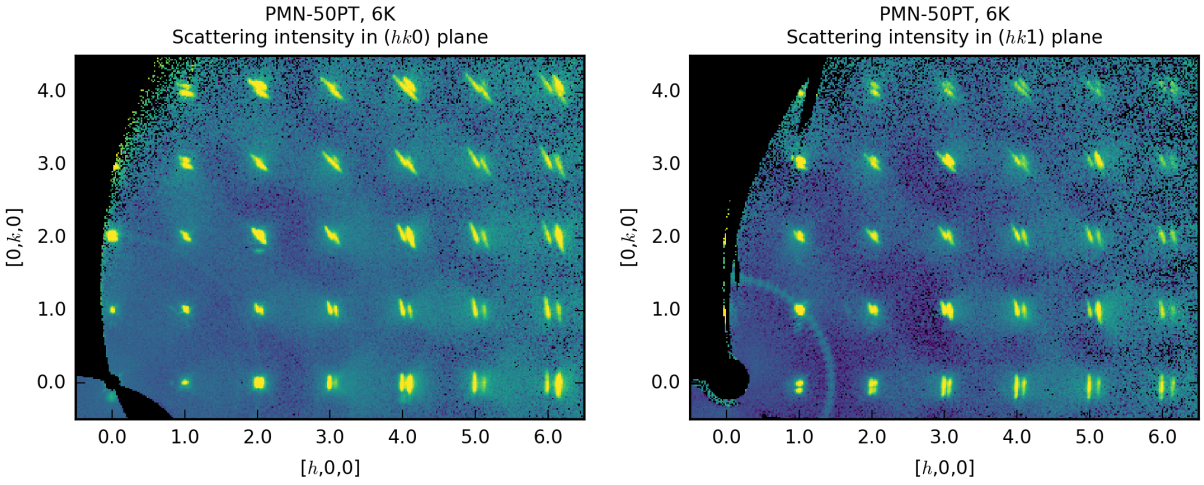

Figure 3.17: Diffuse scattering from PMN-50PT at 6 K, shown in the $l = 0$ (left) and $l = 1$ (right) planes.

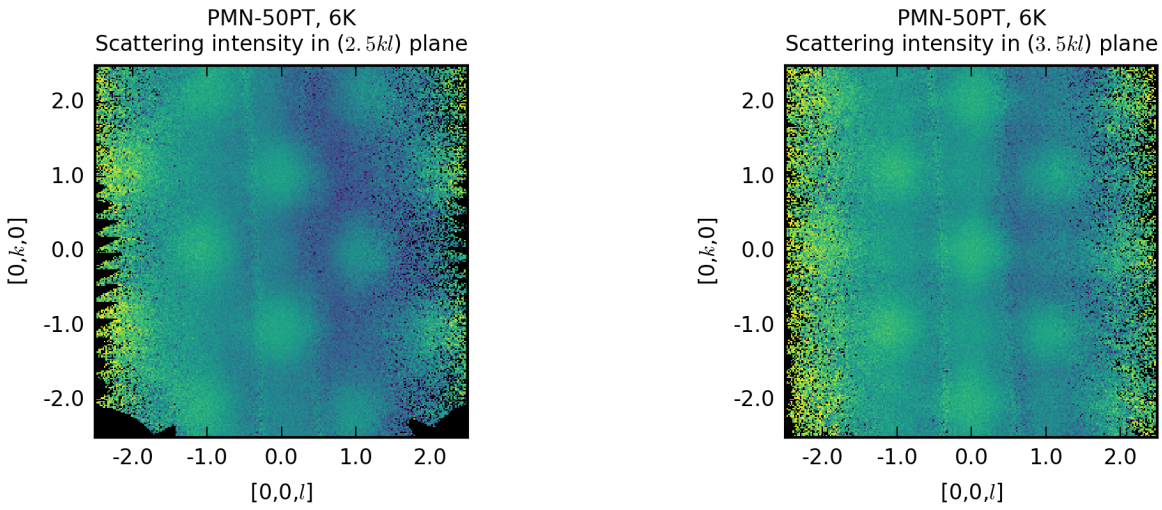

Figure 3.18: Diffuse scattering from PMN-50PT at 6 K, shown in the $h = 2.5$ (left) and $h = 3.5$ (right) planes.

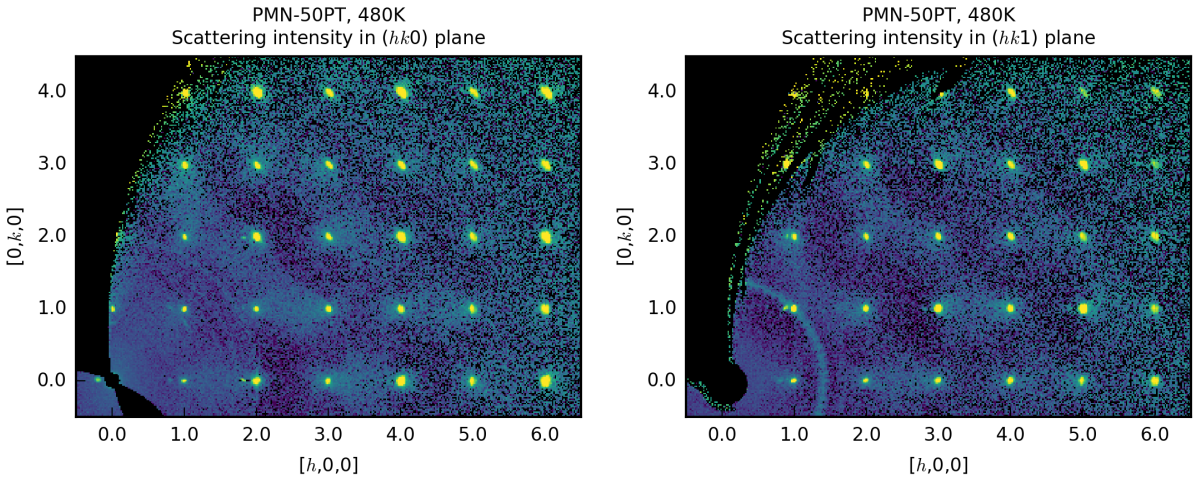

Figure 3.19: Diffuse scattering from PMN-50PT at 480 K, shown in the $l = 0$ (left) and $l = 1$ (right) planes.

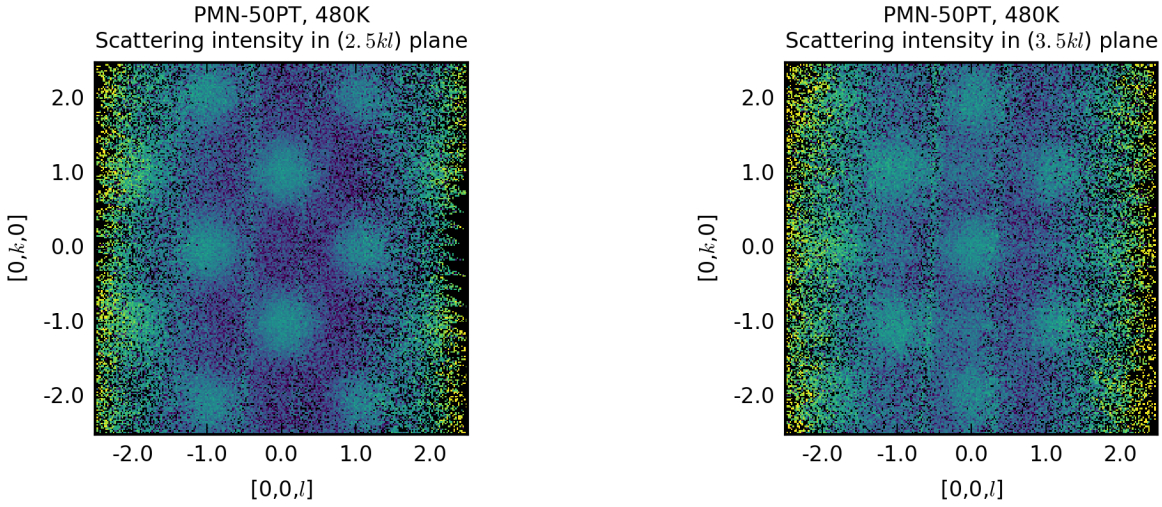

Figure 3.20: Diffuse scattering from PMN-50PT at 480 K, shown in the $h = 2.5$ (left) and $h = 3.5$ (right) planes.

a small number of low-$|\mathbf{Q}|$ Brillouin zones; x-ray scattering data covering the features newly observed with neutron scattering provide a valuable contrast. X-ray and neutron diffuse scattering have different scattering factors: for x-rays, the scattering length for each element is mostly proportional to Z, the atomic number, and decays with increasing $|\mathbf{Q}|$; for neutrons, the scattering length is not correlated to Z. This difference in contrast between the two scatterers emphasizes different correlations. X-ray scattering will be dominated by contributions from Pb atoms, while neutron scattering will be more sensitive to lighter elements such as oxygen (Tab. 3.2).

Table 3.2: The contrasting scattering lengths for neutrons and x-rays produces a contrast between diffuse scattering seen between the two experiments. Particularly noteworthy is the large discrepency between $Z_{Pb}/Z_O = 10.25$ and $b_{Pb}/b_O = 1.62$, making neutron scattering much more sensitive than x-ray scattering to the position of oxygen atoms relative to lead atoms. Values taken from [75]

Element	Z	b
O	8	5.803
Pb	82	9.405
Mg	12	5.375
Nb	41	7.054
Ti	22	-3.438

Small crystals were removed from the large PMN and PMN-30PT crystals examined with neutrons for diffuse x-ray scattering experiments. To avoid the surface effects indicated by other studies [76], x-ray samples were etched in hydrochloric acid at 350 K for 60 minutes prior to being mounted on kapton capillaries with binary epoxy. To ensure x-rays penetrated the bulk of the sample, an incident beam energy of 56.8 keV ($\lambda = 0.218$Å) was used. This high incident energy produces artifacts in the Si-based detector as discussed in Ch. 1.3.

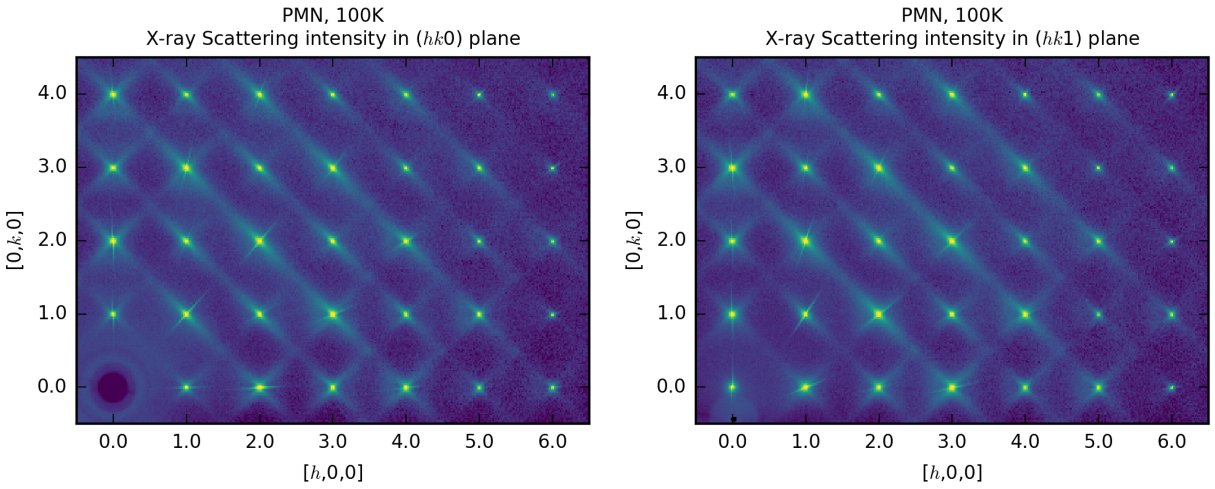

Figure 3.21: Diffuse x-ray scattering from PMN at 100 K, shown in the $l = 0$ (left) and $l = 1$ (right) planes.

3.2.1 PMN

A sample of PMN was measured at 100 K, 200 K, 300 K and 400 K; as seen in Fig. 3.1, these temperatures are both above and below $T_m(f) \approx 220$K.

As seen in Figs. 3.21 and 3.22, many of the features identified in the neutron picture can be seen in the x-ray diffuse scattering at 100 K as well. The 'butterfly' scattering surrounding each Bragg peak is easily seen, in some cases extending all the way to the M point. Scattering from half-integer planes clearly reveal broad peaks on M and R points, and a quite broadly-varying background can be seen as well, similar to that seen with neutron scattering for compositions with 20% titanium and above; reexamination of the neutron scattering data show that this scattering is also present in PMN, while much weaker than it is for other samples. This feature is thus the only one present for all compositions of PMN-xPT measured, and is indeed present at all temperatures as well.

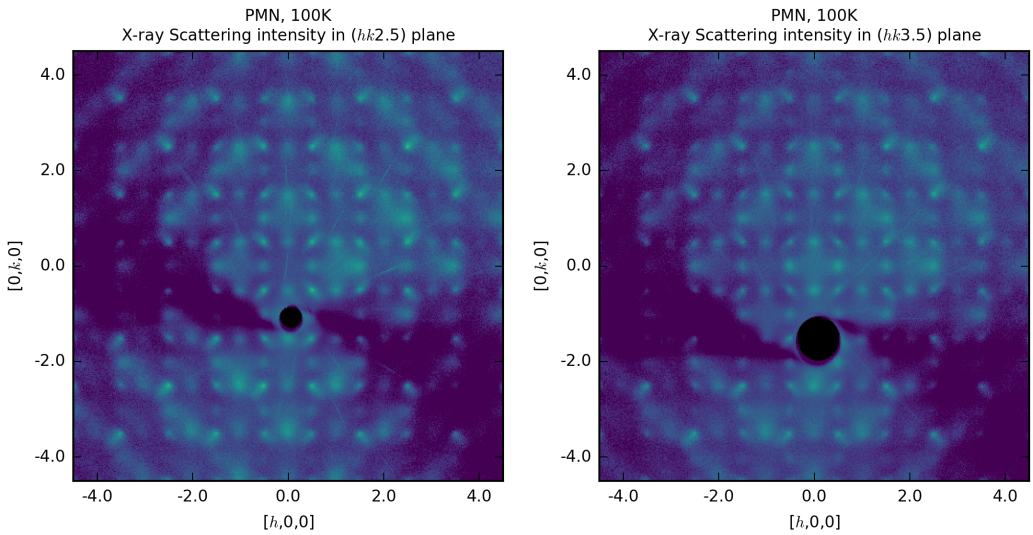

Figure 3.22: Diffuse x-ray scattering from PMN at 100 K, shown in the $l = 2.5$ (left) and $l = 3.5$ (right) planes.

Raising the temperature to 400 K brings similar changes to diffuse x-ray scattering from PMN as it does to diffuse neutron scattering. The butterfly scattering close to Bragg peaks diminishes in intensity and sharpness compared to lower temperature, the M point peaks are greatly weakened, and the R point peaks seem relatively unaffected.

3.2.2 PMN-30PT

Two samples of PMN-30PT were measured at 100 K, 200 K, 300 K, and 400 K; all temperatures are below T_C for this sample. Data from only one sample is shown, but the two show consistent pictures of diffuse scattering.

As seen with neutrons, the addition of titanium to PMN changes diffuse scattering considerably. At low temperature, the spatial extent of the diffuse scattering surrounding Bragg peaks is reduced, with this scattering appearing more concentrated around the Bragg peaks. The broad peaks at M and R points are no longer visible, but the broad scattering spanning

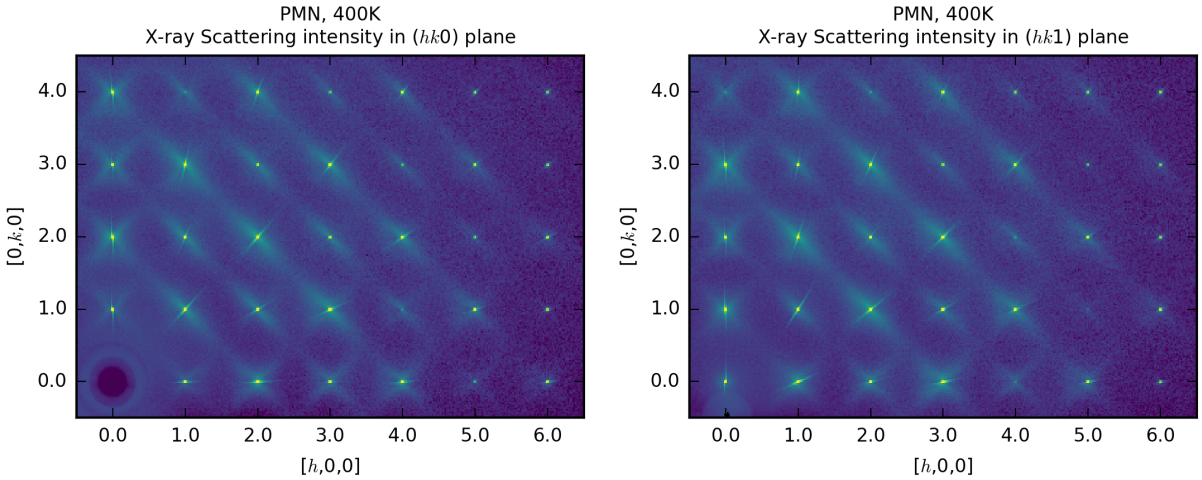

Figure 3.23: Diffuse x-ray scattering from PMN at 400 K, shown in the $l = 0$ (left) and $l = 1$ (right) planes.

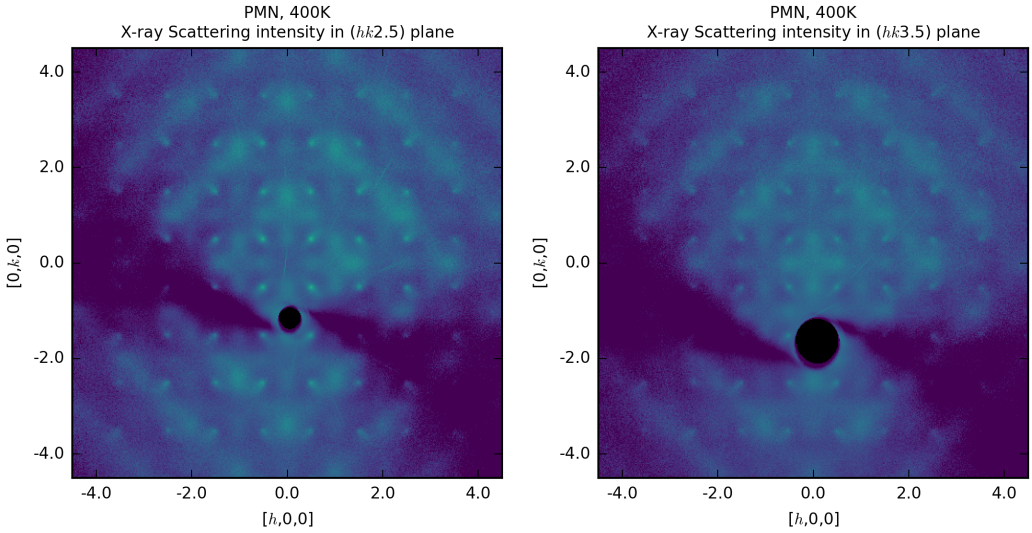

Figure 3.24: Diffuse x-ray scattering from PMN at 400 K, shown in the $l = 2.5$ (left) and $l = 3.51$ (right) planes.

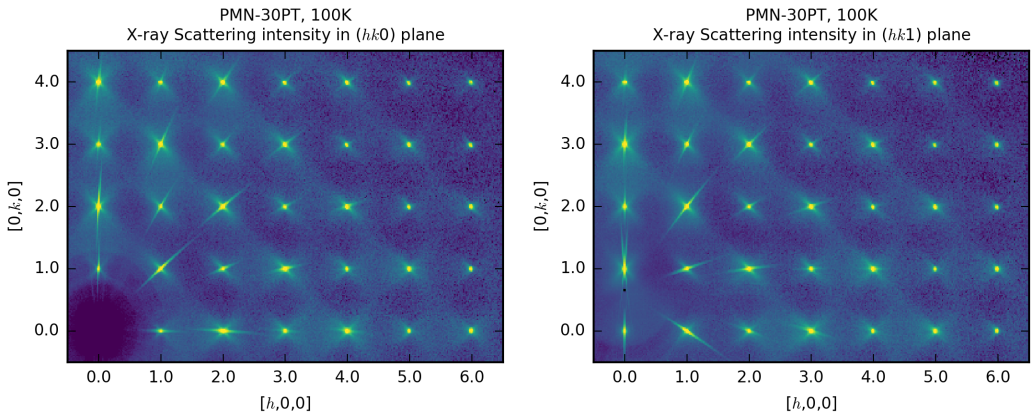

Figure 3.25: Diffuse x-ray scattering from PMN-30PT at 100 K, shown in the $l = 0$ (left) and $l = 1$ (right) planes.

Brillouin zones appears stronger. This scattering is considerably better resolved with the x-ray measurements than with the neutron measurements, and can now be clearly seen to consist of diffuse octahedra, alternating in intensity in a checkerboard-like pattern throughout reciprocal space and increasingly distorted as the region of reciprocal space gets farther away from $\langle 100 \rangle$ directions. Interestingly, the faint hint of the M point peaks seen with neutron scattering is absent in the x-ray picture, an indication of contrast between the scatterers of the different features.

The highest temperature for PMN-30PT surveyed with x-rays was 400 K, lower than the 470 K achieved during the neutron measurements and ambiguously close to the presumed $T_C \approx 410$ K for this sample. As with other samples, higher temperatures make the zone-centered diffuse scattering less apparent, while leaving the broad zone-spanning features more intact.

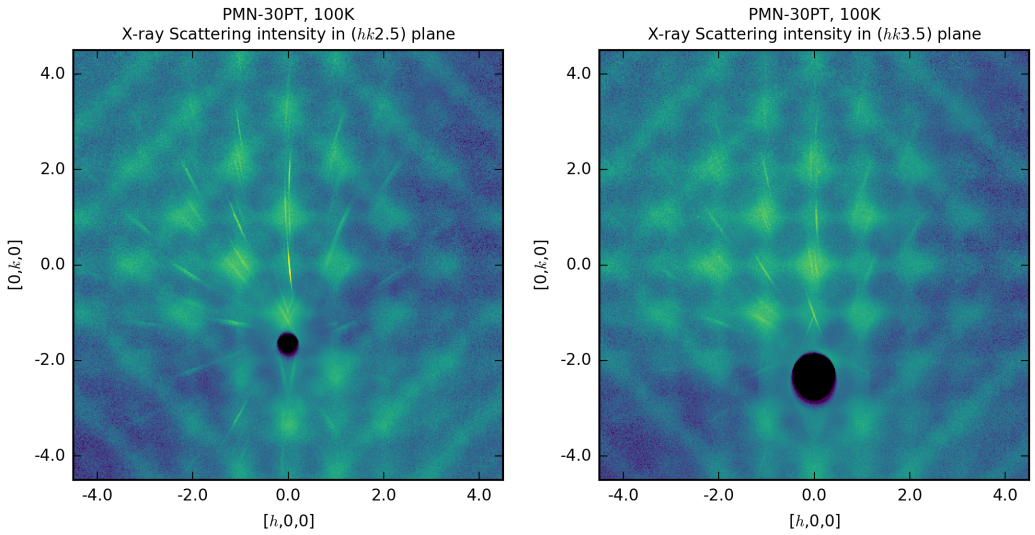

Figure 3.26: Diffuse x-ray scattering from PMN-30PT at 100 K, shown in the $l = 2.5$ (left) and $l = 3.5$ (right) planes.

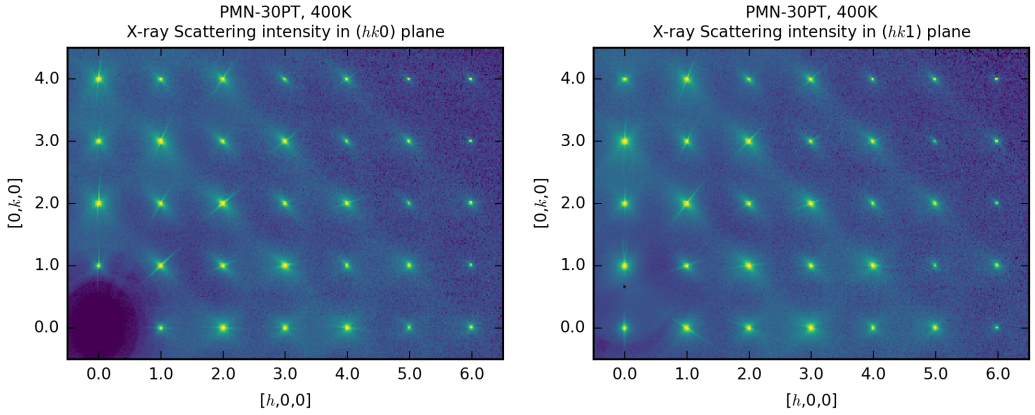

Figure 3.27: Diffuse x-ray scattering from PMN-30PT at 400 K, shown in the $l = 0$ (left) and $l = 1$ (right) planes.

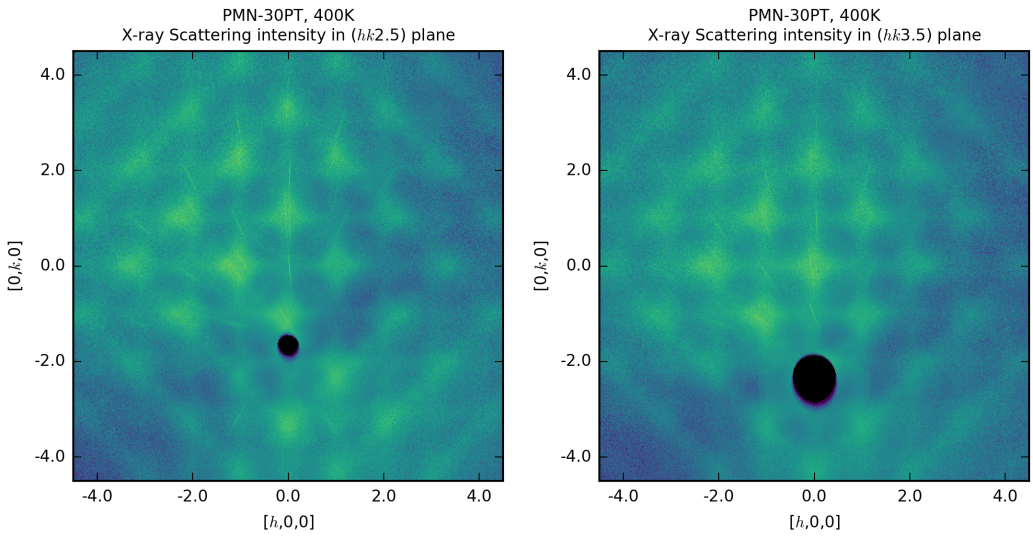

Figure 3.28: Diffuse x-ray scattering from PMN-30PT at 400 K, shown in the $l = 2.5$ (left) and $l = 3.51$ (right) planes.

3.3 Components of Diffuse Scattering

A brief overview of the compositional dependence of each distinct feature of diffuse scattering found in the data will follow, after which each component will be discussed in detail. Fig. 3.29 shows trends in the bulk properties of PMN-xPT alongside trends in the various diffuse scattering components.

The first component considered will be the so-called 'butterfly' diffuse scattering surrounding Bragg peaks, concentrated around $\mathbf{q} = 0$. This component, the main focus of most previous studies of diffuse scattering from PMN-xPT, is apparent in samples from $x = 0$ to $x = 0.35$ but not in more Ti-rich samples. Previous studies have shown that this component changes significantly under applied electric fields; as such, this work will refer to this feature as ferroic diffuse scattering or *C1* scattering in PMN-xPT. The intensity of this component close to $\mathbf{q} = 0$ is correlated with the piezoelectric tensor component d_{33} and thus the electromechanical coupling of the material.

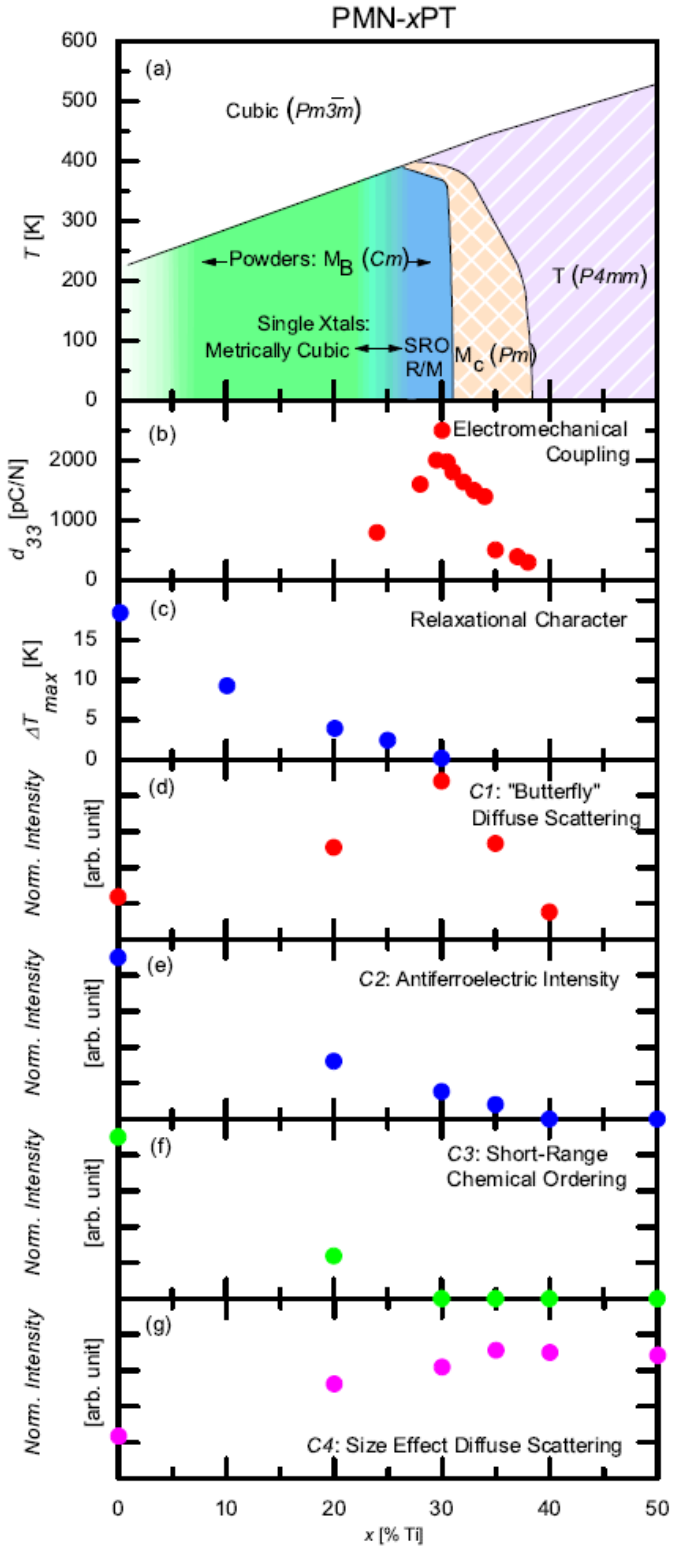

Figure 3.29: (a) Structural phase diagram for single crystals of PMN-xPT as adapted from [39]. Here "SRO R/M" refers to a region in the phase diagram where there is short-range rhombohedral or monoclinic order that is resolvable from splitting of fundamental Bragg reflections. "M_c" refers to a monoclinic symmetry with space group Pm [77]. "T" refers to tetragonal symmetry. (b-f) Compositional dependence of various parameters. (b) The piezoelectric coefficient, d_{33}, as reported for single crystals and adapted from [43]. (c)ΔT_{max}, as described in text. Data was collected and adapted from [40]. (d) Amplitude of *C1* measured with neutrons. Amplitude was estimated by integrating intensity in a section of the diffuse lobes around the 200 Bragg peak, centered on (2.14, 0.14, 0.0). (e) Amplitude of the M-point scattering (*C2*), obtained by least-squares fitting a Gaussian function to the (3.5,0.5,0.0) peak. (f) Amplitude of the R-point scattering (*C3*) obtained by least-squares fitting a Gaussian function to the (2.5,0.5,0.5) peak. (g) Amplitude of the size-effect scattering (*C4*) obtained by integrating over 0.4x0.4x0.4 r.l.u. box centered on (3.5,0,0). Linear vertical scales are used for (d)-(g). Data collected at 6 K for (d)-(g).

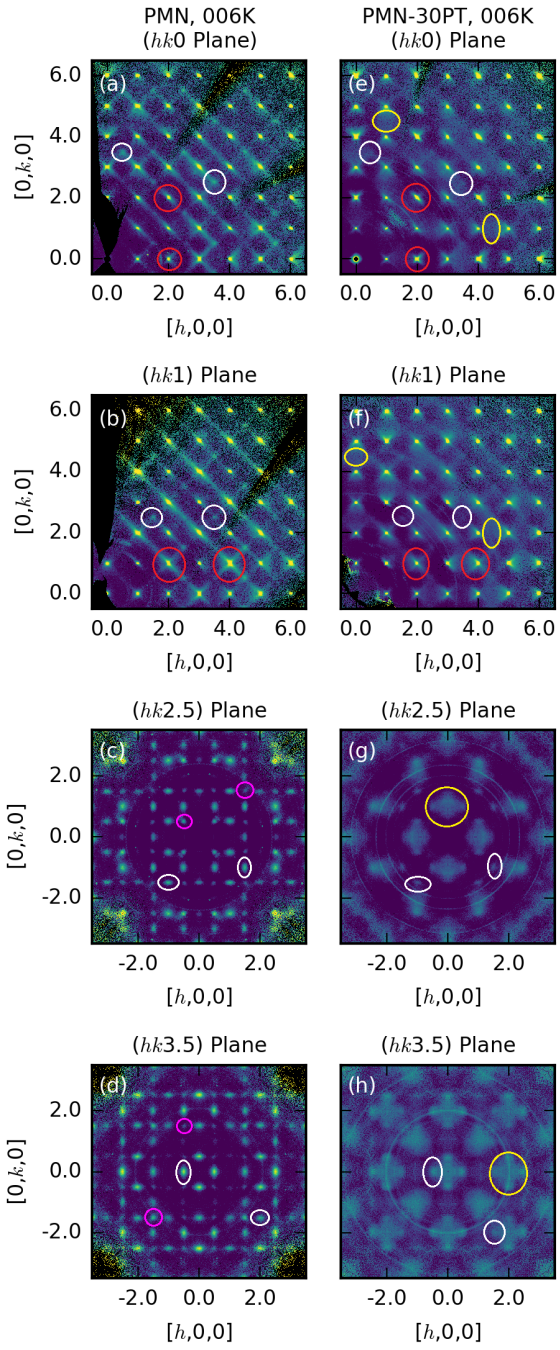

Figure 3.30: Reciprocal space maps of neutron scattering intensities measured on *Corelli* at 6 K. Data are shown in the $l = 0$, 1, 2.5, and 3.5 planes in panels (a), (b), (c), and (d) for $x = 0.0$ and (e), (f), (g), and (h) for $x = 0.3$, respectively. Data have been integrated over a range in l of 0.06 r.l.u. Four different diffuse scattering features, as discussed in the text, are indicated with colored circles: *C1* with red, *C2* with white, *C3* with magenta, and *C4* with yellow. Intensity scales are logarithmic.

The second component considered will be the somewhat oblong diffuse peaks centered on M points $\frac{1}{2}(2h+1, 2k+1, 2l)$ in the Brillouin zone. These are most clearly apparent in PMN, but they are also resolvable in PMN-20PT and PMN-30PT as 'shoulders' on another component (*C4*, to be discussed later). These peaks have strong temperature dependence and have been connected by previous studies to antiferroelectric interactions. This component of diffuse scattering will be referred to as *C2*, and its intensity is correlated with the relaxational character of the sample.

The third component considered will be the diffuse peaks centered on R points of the Brillouin zone $\frac{1}{2}(2h+1, 2k+1, 2l+1)$. These are again most apparent in pure PMN, with some small trace remaining for Ti concentrations up to $x = 0.3$. The temperature dependence of this scattering shows a contribution similar to *C2* and another, temperature-independent component indicative of short-range chemical ordering of Mg and Nb atoms. This scattering will be referred to as *C3*.

The fourth and final component considered is perhaps the most apparent in the figures shown: broad scattering between Bragg peaks that alternates in intensity between zones, forming pseudo-octahedra centered on **X** points along the $\langle h00 \rangle$ directions. This scattering is apparent in previous studies, but it had not been clearly identified as a component separate from others. It is only weakly temperature-dependent in the region studied and increases in intensity as Ti concentration increases, at least up to $x = 0.5$. It is caused by a tendency of Pb atoms to be closer than average to Mg and Ti atoms and farther away from Nb atoms. This can thus be considered a size effect, although the origin may not be strictly related to the effective radius of the cation. While this scattering does not appear to be directly related to any bulk physical properties, its presence is important to recognize, as it can easily confound measurements of *C1* and *C2*, and it may be indicative of the strong local interactions necessary for a random-field model of relaxor ferroelectrics. This scattering will be referred to as *C4*.

3.3.1 *C1*: Ferroic Scattering

As discussed in Chapter 2.3, most previous studies on diffuse scattering in PMN-xPT have focused on areas close to Bragg positions. The 'butterfly' appellation is a bit imprecise; while this diffuse scattering somewhat resembles a butterfly around certain $\langle h00 \rangle$ Bragg peaks, other $\langle h00 \rangle$ peaks may show a strong imbalance between the wings, particularly with neutron scattering, and the scattering around $\langle hh0 \rangle$ peaks displays only one rod along the perpendicular $\langle hh0 \rangle$ direction. These significant details and the array of different local distortions in other systems that can give rise to such a 'butterfly' shape (Huang scattering in bilayer manganites, etc.) are at odds with the uncertainty of the local displacement correlations that must give rise to this feature; this work will thus refer to this component as ferroic diffuse scattering, or *C1*.

Both neutron and x-ray experiments confirmed the presence of this feature around every Bragg peak surveyed. In a clear difference from previous studies, neutron scattering clearly indicate inter-zone intensity modulations to *C1*. Specifically, if the Miller indices hkl of a Bragg peak are all odd or all even, then *C1* is stronger on the high-$|\mathbf{Q}|$ side of the Bragg peak; otherwise, the scattering is stronger on the low-$|\mathbf{Q}|$ side. This rule holds for all Brillouin zones and is most easily visualized along $\langle h00 \rangle$, where successive zones have diffuse intensities that alternate between strong high-$|\mathbf{Q}|$ and strong low-$|\mathbf{Q}|$. A broader view of scattering shows the universality of these modulations – Fig. 3.31 shows an hhl scattering plane from PMN-30PT, and the rule can be seen to hold even for the weaker lobes emanating along $\langle 110 \rangle$ for hhl peaks.

Most previous neutron studies have focused on a small number of mainly low-$|\mathbf{Q}|$ Brillouin zones and were thus unable to identify this asymmetry [57, 62, 63, 78]. While it is not surprising that this feature had not been appreciated in previous neutron scattering

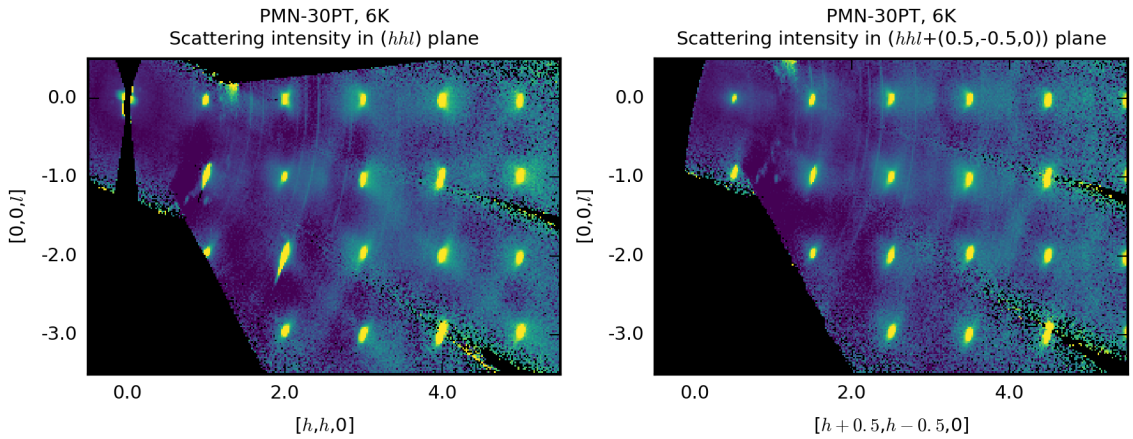

Figure 3.31: Figure 3. Diffuse neutron scattering from PMN-30PT shown in the *hhl* scattering plane. While the *C1* scattering components are weak in this plane, the asymmetry between low-$|\mathbf{Q}|$ and high-$|\mathbf{Q}|$ is apparent, with peaks of all even or all odd indices showing more *C1* intensity on the high-$|\mathbf{Q}|$ side and other peaks with more *C1* intensity on the low-$|\mathbf{Q}|$ side.

measurements, in retrospect it is recognizable in previous reports on PMN and related systems [24,57,79–81]. However, it is surprising that this intensity modulation was not reported in previous synchrotron x-ray studies, as synchrotron x-ray sources typically provide access to a much larger $|\mathbf{Q}|$-range. We therefore carried out complementary x-ray scattering experiments (Fig. 3.32 shows x-ray scattering intensity maps measured on pieces taken from the same crystals in the same planes as shown for neutrons in Fig. 3.30). Fig. 3.33 compares the diffuse scattering surrounding the 400 Bragg peak for $x = 0.3$ in the $l = 0$ plane for x-rays (Fig. 3.33(a)) and neutrons (Fig. 3.33(d)), and it appears that the low-$|\mathbf{Q}|$ and high-$|\mathbf{Q}|$ intensities are much closer to equal for x-rays than for neutrons. This is confirmed by examination of the $(3.9, k, l)$ and $(4.1, k, l)$ planes, which illustrate the distribution of *C1* on the low-$|\mathbf{Q}|$ and high-$|\mathbf{Q}|$ sides of 400, respectively for both x-rays (Fig. 3.33(b) and (c)) and neutrons (Fig. 3.33(e) and (f)). The large difference in intensity between the low-$|\mathbf{Q}|$ and

high-|**Q**| diffuse lobes measured with neutrons around this peak does not match the nearly equal intensity distribution of the same diffuse lobes measured with x-rays. For peaks of all even or all odd Miller indices, the *C1* intensity is close to symmetric when measured with x-rays; for peaks of mixed even and odd indices,the same asymmetry observed with neutrons is observed with a less extreme difference in intensity with x-rays.

The large penetration depths of both the neutrons and the high-energy x-rays used in our study ensure that both probes sampled the bulk of the crystals, so the observed difference is not due to a skin effect [39, 74, 82]. Moreover, the low-|**Q**|/high-|**Q**| inter-zone modulations described above are present in both the elastic and energy-integrated neutron cross-sections, which indicates that this difference between neutron and x-ray data is not due to the integration of low-lying phonon modes in the x-ray experiments and that this feature is static in origin. Thus, the observed differences are intrinsic and result from differences in diffuse scattering structure factors due to the disparate scattering lengths of the constituent atoms for these two probes. Scattering from x-rays is dominated by the heavy Pb cations, neutrons are much more sensitive to O anions. Calculations of Bragg structure factors demonstrate the influence of O in tetragonal, Ti-rich compositions where similar modulations can occur. This clearly demonstrates that correlated O displacements play a significant role in *C1*. This is further bolstered by the intensity rule of the interzone modulation, which indicates a 'halving' of the unit cell consistent with the Pb-O distance.

The inter-zone modulation of *C1* is similar to the pattern of Bragg peak splitting due to domain formation in PMN-xPT on the tetragonal side of the MPB, as seen with PMN-50PT in Fig. 3.34. Below T_C, all cubically indexed $h00$ and $hh0$ peaks split due to the tetragonal distortion. Because of the unique c-axis which is larger than the a-axis, both $\langle h00\rangle$ and $\langle 0h0\rangle$ reflections will contribute to a peak with a lower d-spacing than the single $\langle 00h\rangle$ peak with higher d-spacing, leading to a difference in intensity between the split peaks of 2:1 before the structure factor is considered. We observed that the higher-d reflections for the odd

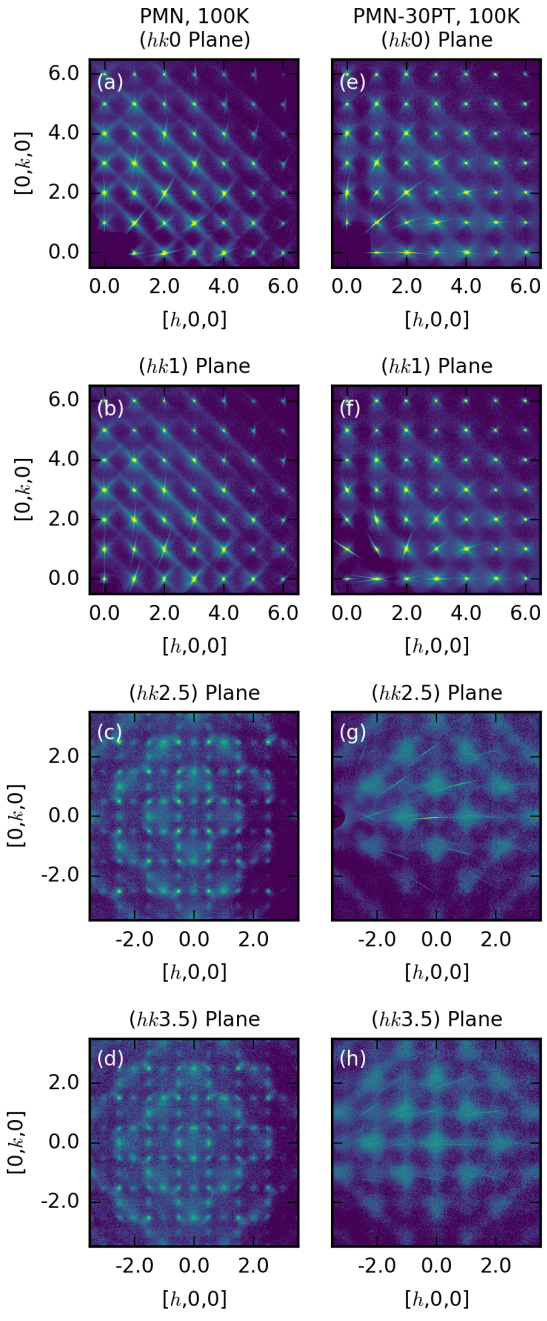

Figure 3.32: Reciprocal space maps of x-ray scattering intensities measured at CHESS at 100 K. Data are shown in the $l = 0$, 1, 2.5, and 3.5 planes in panels (a), (b), (c), and (d) for $x = 0$ and (e), (f), (g), and (h) for $x = 30\%$, respectively. Data have been integrated over a range in l of 0.06 r.l.u.

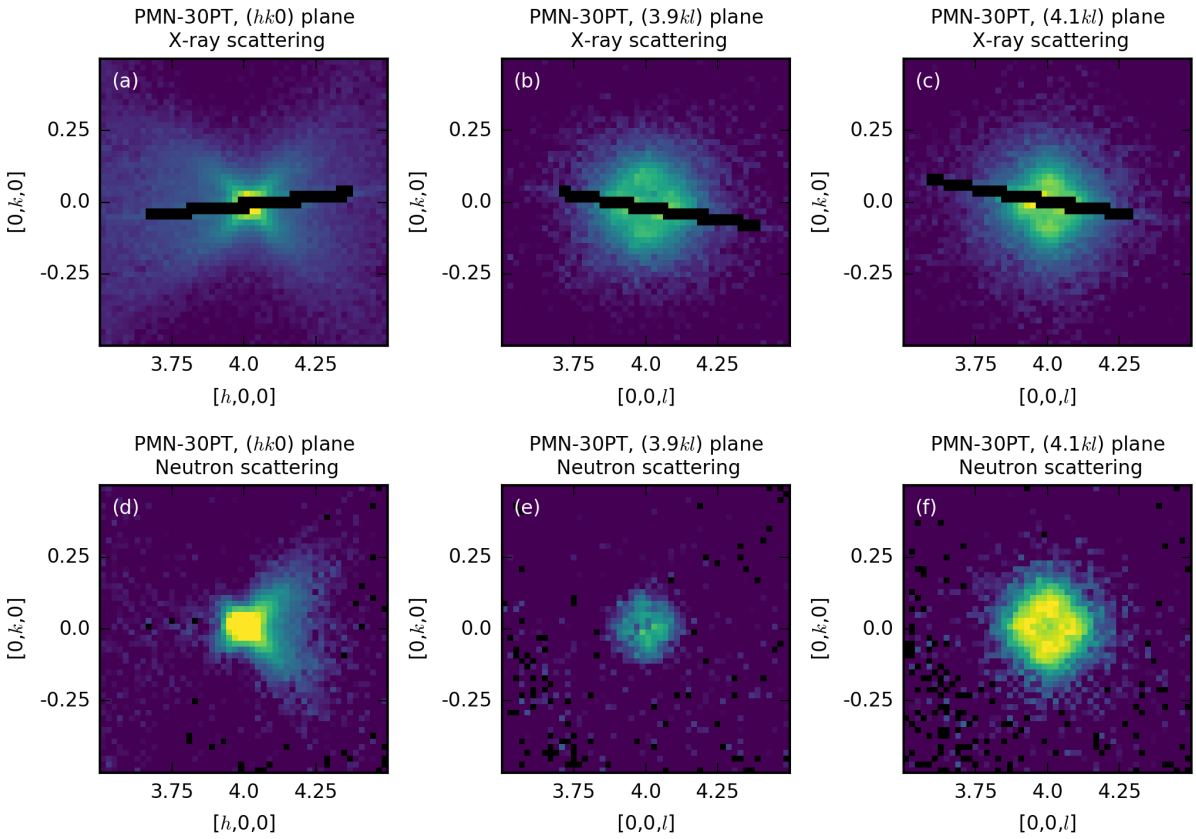

Figure 3.33: Diffuse scattering patterns in the 400 Brillouin zone for x=30. (a-c) $(h, k, 0)$, $(3.9, k, l)$ and $(4.1, k, l)$ planes measured at 100 K with x-rays. (d-f) $(h, k, 0)$, $(3.9, k, l)$ and $(4.1, k, l)$ planes measured at 6 K with neutrons. The $(3.9, k, l)$ and $(4.1, k, l)$ planes show the lobes of scattering in the planes perpendicular to the $(h, k, 0)$ plane as marked in panels (a) and (d). Data have been integrated in the normal direction over a range of 0.02 rlu. Intensity scales are logarithmic. Black bars in (a-c) indicate regions where reliable data were not collected.

$\langle h00 \rangle$ peaks and the lower-d reflection for the even $\langle hh0 \rangle$ peaks are actually stronger, with the weaker reflection almost entirely suppressed in some cases; this is a direct result of the neutron structure factor being more influenced by lighter atoms. This disparity is lessened, though not eliminated, for x-ray scattering; a comparison of neutron scattering data to calculated structure factors is shown in Fig. 3.34. Though this does not necessarily imply that the local displacements behind *C1* are identical to the long-range displacements in the tetragonal phase, the *C1* neutron structure factors are similarly influenced by lighter atoms, suggesting correlated displacements involving lighter atoms are the source of the inter-zone modulation. These structure factor calculations were made using the atomic positions in the tetragonal unit cell for PMN-50PT from Kania *et al.* [34]

The calculation of *C1* diffuse scattering was done by integrating scattering intensity along a [110] cut through one of the diffuse lobes. As may be apparent from examination of this scattering from different samples, the location of this cut has some effect on the compositional dependence. Fig. 3.35 shows how changing the location of this cut changes this compositional dependence. As the cut is taken farther and farther from $\mathbf{q} = 0$, the relative strength of scattering from morphotropic PMN-30PT and PMN-35PT samples diminishes with respect to that from pure PMN. While caution in extracting correlation lengths from this sort of data is advised, this change of reciprocal space extent is consistent with a picture of displacement correlations having a shorter characteristic length in the relaxor PMN than in the Ti-alloyed relaxor ferroelectrics.

While a specific atomic model of displacements is still elusive, a quick simulation of a PMN crystal in *DISCUS* illustrates a toy model that can generate diffuse scattering with similar features to those seen in *C1*, particularly with neutrons. Each oxygen atom is assigned a type based on its two nearest neighbors, and Pb atoms are displaced depending on the oxygen neighbors: toward those O atoms with two Mg neighbors, away from those with two Nb neighbors, and with average distance towards those with one of each type. This

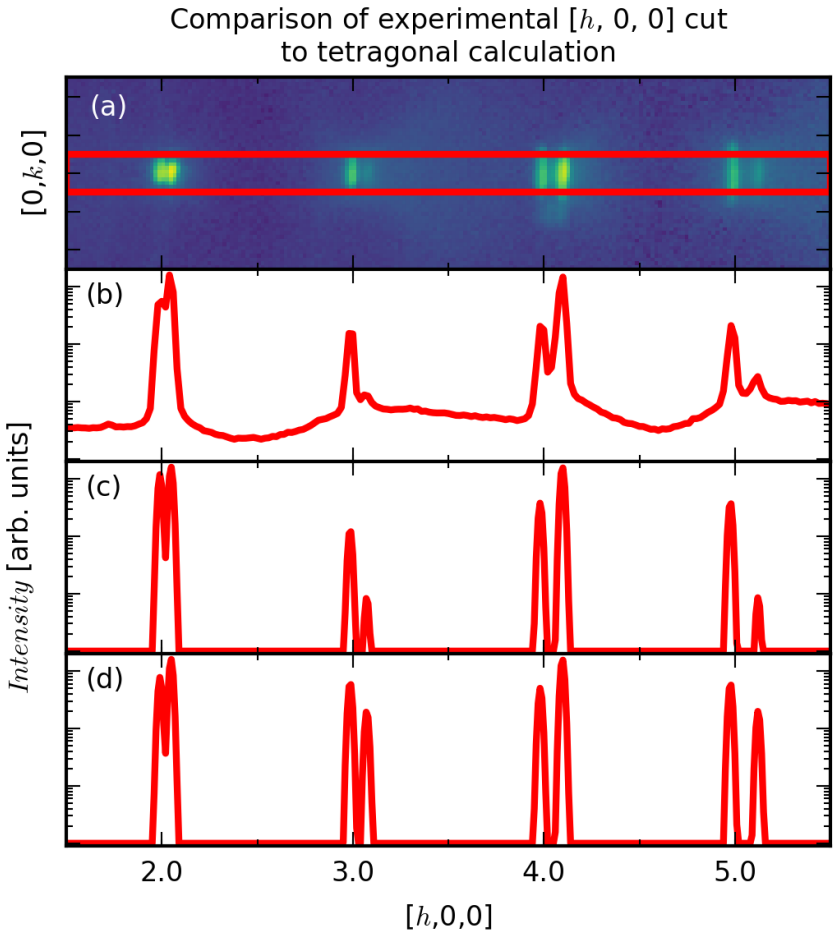

Figure 3.34: Cuts through $h00$ peaks of tetragonal PMN-50PT, measured at 6 K. (a) Area plot of scattering intensity of PMN-50PT. Note splitting of peaks. (b) Cut through Bragg peaks showing experimental split intensity ratios. (c) Calculated neutron Bragg scattering cut using published unit cell of PMN-50PT [34]. (d) Calculated x-ray scattering cut using published unit cell of PMN-50PT. The vertical scale on (b-d) is logarithmic.

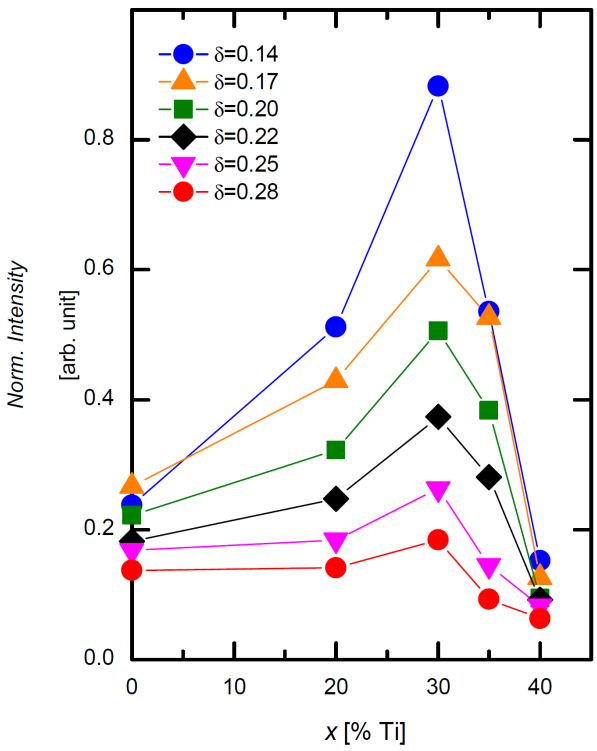

Figure 3.35: Compositional dependence of the numerically integrated intensity of diffuse *C1* as measured with neutrons at 6 K using different offsets from the 200 Bragg reflection. Here, the cuts are made along the [110] direction with $\mathbf{q} = (\delta, \delta, 0)$, so that $\mathbf{Q} = (2 + \delta, \delta, 0)$.

model produces diffuse scattering centered on Bragg peaks with all-even or all-odd Miller indices and displays a marked discrepency between neutron and x-ray scattering. Neutron scattering shows diffuse scattering mainly around Bragg peaks will all even or all odd Miller indices; x-ray scattering is dominated by the Pb to B (Mg, Nb, Ti) size effect scattering (*C4* scattering), a secondary effect of Pb atoms moving closer to Mg atoms and farther away from Nb atoms via their interactions with different types of oxygen atoms. While this is quite far from a complete model from PMN-xPT, adding correlations between oxygen and lead displacements to more realistic models of polar behavior may be sufficient to generate the observed asymmetry in *C1* diffuse scattering.

A connection to the bulk properties of PMN-xPT is found in the compositional dependence of *C1*. Reciprocal space maps of neutron diffuse scattering for the $h00$ set of Brillouin zones for different compositions are shown in Fig. 3.37. The compositional dependence of *C1* is most easily illustrated by the set of linear cuts offset by $k = 0.14$ r.l.u., as shown in Fig. 3.37(f-j). *C1* is clearly present for $0 \leq x \leq 0.35$. At $x = 0.4$, the intensity is drastically weaker, and the tetragonal domain structure appears, which causes the $h00$ Bragg peaks to split. ($x = 0.5$ data is not included due to the large distortion of the Bragg peaks at $T = 6$ K). Qualitatively, *C1* is most extended in $|\mathbf{Q}|$ at $x = 0$ and becomes increasingly centralized (pushed in towards $|\mathbf{q}| = 0$) as x approaches the MPB (though it still extends out well beyond the Bragg peak). The amplitude of *C1*, shown in Fig. 3.29, increases with x from $x = 0.0$ to $x = 0.3$, where it is maximal; it then falls off precipitously upon further increase in x. The enhancement of the $|\mathbf{q}| = 0$ component upon increasing x towards the MPB is consistent with the work of Matsuura et al. [83], and the disappearance of *C1* in the tetragonal phase is consistent with Stock *et al.*'s finding of a lack of diffuse scattering for $x = 0.6$ [81]. Thus, *C1* is present in all compositions on the Ti-poor side of the MPB, peaking in intensity in the MPB and disappearing on the Ti-rich side of the MPB.

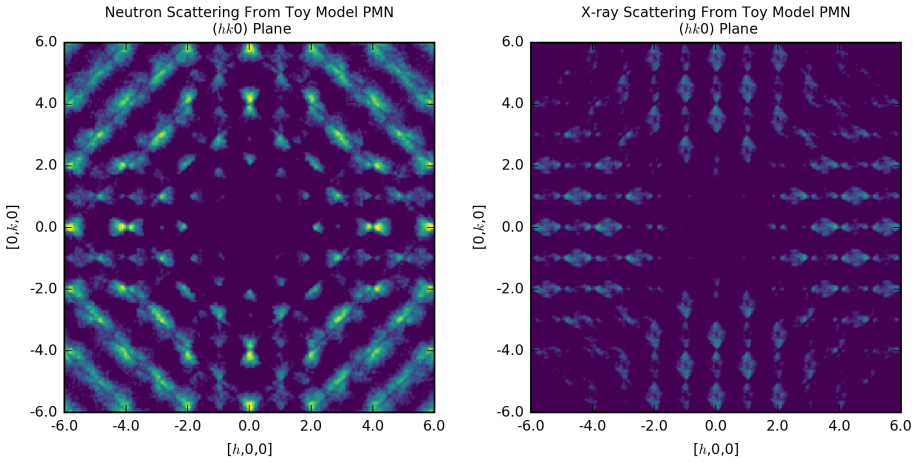

Figure 3.36: Diffuse scattering in the $hk0$ from a Monte Carlo simulated PMN crystal, where Pb atoms are displaced along $\langle 110 \rangle$ directions toward O atoms with two Mg neighbors (average Pb-O distance for this type of O atom is 0.92 times undistorted distance) and away from O atoms with two Nb neighbors (average Pb-O distance for this type of O atom is 1.1 times undistorted distance). Neutron scattering (left) from this simulated crystal show interesting similarities with observed data, while x-ray scattering (right) is dominated by secondary effects; this discrepency is itself tied to the importance of O displacements in the neutron scattering picture.

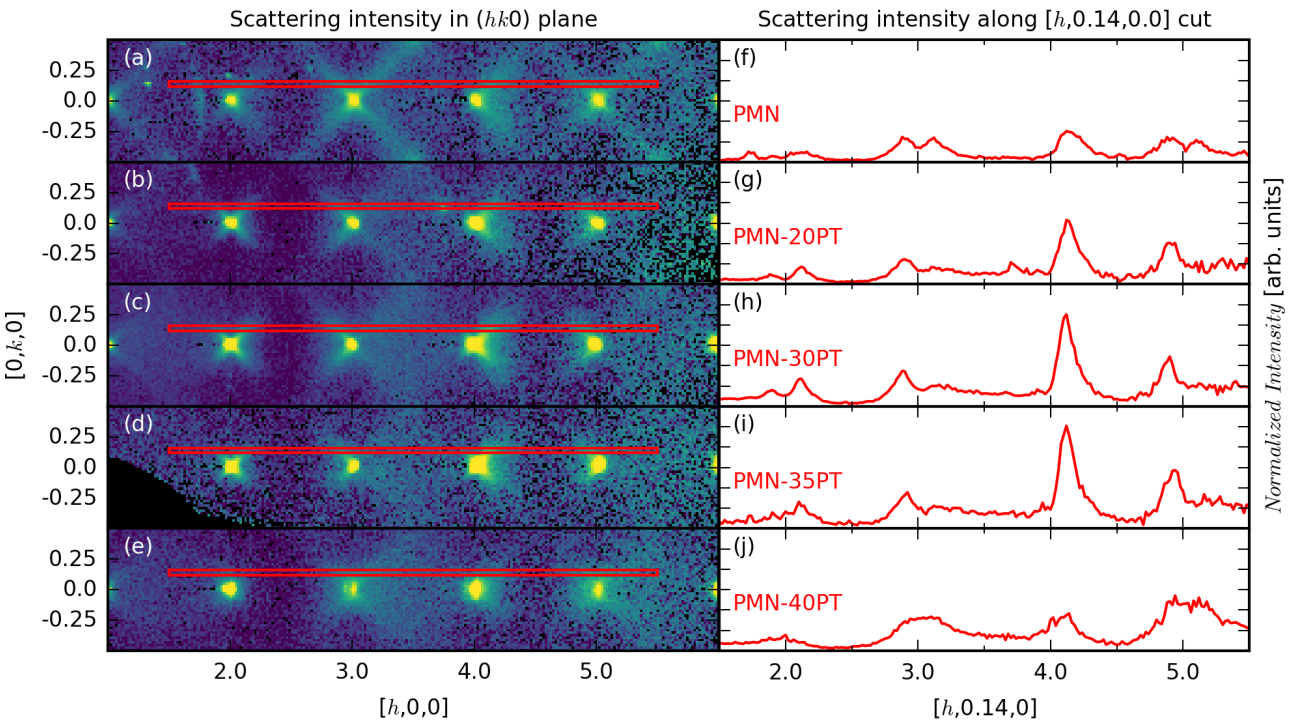

Figure 3.37: (a-e) Reciprocal space maps of the $h00$ set of Brillouin zones in the $(hk0)$ plane measured at 6 K with neutrons for $x = 0, 20, 30, 35$, and 40 respectively, integrated over a range of 0.04 r.l.u. in l. Intensity scales are logarithmic. (f-j) Corresponding cuts through the data in (a)-(e) along $(h, 0.14, 0)$ with intensities integrated along k from 0.12 to 0.16 and along l from -0.02 to 0.02. The vertical scales are linear.

Consideration of temperature dependence further connects this scattering to a low-temperature ferroic state. In both PMN and PMN-30PT, the intensity of *C1* is strongest at low temperatures and decreases as temperature is increased. (PMN-20PT was only measured at 6 K.) The largest range of temperatures was studied in PMN; in this sample, *C1* begins to significantly weaken above $T_m(f)$ in the relaxor state and is fully suppressed between 600 K and 700 K. This coincides with the Burns temperature for PMN, $T_B = 620$ K [8]. While such temperatures were not achieved in experiments on other samples, it may be supposed that the correlations generating *C1* are present in some form below T_B and absent above. It is established in PMN-30PT that *C1* scattering is strongest at low temperature, declines slightly but remains significant for temperatures up to T_C, and declines more quickly above T_C. The combination of *Corelli*'s elastic discrimination, a temperature dependence suggesting that thermal interactions weaken *C1*, and previous neutron spin echo experiments clearly showing this type of diffuse scattering is elastic [73] below 450 K should be a strong argument against *C1* scattering being generated by dynamic processes in PMN-xPT.

Despite significant discussion in the literature relating *C1* diffuse scattering to relaxor physics, a comparison of the compositional dependence of ΔT_{max} (Fig. 3.29(c)) to that of *C1* (Fig. 3.29(d)) shows that *C1* is maximal where the relaxational character is essentially absent. This indicates that *C1* is not directly related to relaxational dielectric behavior. However, it is notable that both d_{33} and *C1* are maximal at the MPB ($x \approx 0.3$). This suggests a physical connection between the electromechanical coupling and *C1*. That said, *C1* is also present in compositions (e.g. $x = 0.0, 0.2$) for which electromechanical properties are poor, so its presence alone cannot account for electromechanical coupling. It is also worth noting that while the intensity of *C1* is reduced for small $\mathbf{q}$ in more relaxational samples, the spatial extent of *C1* appears larger. Strong electromechanical coupling implies a free energy landscape in which multiple states have similar energies such that their populations are influenced by external electric fields. Such a situation would lead to competing mesoscopic

domains that are enhanced at the MPB and thus enhance *C1*. Adaptive phase models [84] and anomalous domain wall densities [52] have been considered as potential mechanisms that could connect electromechanical coupling to *C1*. This study highlights the need to account for oxygen displacements in modelling and understanding strong electromechanical coupling in this system. The recent molecular dynamics simulation of PMN-25PT by Takenaka *et al.* [52] reproduces this changing asymmetry with neutron scattering; other models should also be investigated for this feature.

3.3.2 *C2*: M-point Scattering

A second contribution to the diffuse scattering, *C2*, consists of broad peaks centered on zone-boundary **M** points. These are apparent in Fig. 3.30 for $x = 0$ (indicated by white circles), but they are strongly suppressed for $x = 0.3$. As mentioned above, M-point scattering has been reported in x-ray scattering experiments for crystals with $x = 0.0$ [70, 85] and $x = 0.06$ [70], but it was unresolvable for $x = 0.10$ [70]. These peaks have been attributed to antiferrodistortive Pb displacements [70], and neutron inelastic scattering experiments have shown that they originate from the condensation of unusually damped, soft optic phonons [71]. Comparison between the neutron and x-ray scattering also reveals a likely link between *C2* and O displacements. When measured with x-ray scattering, *C2* is weaker than *C3*; the opposite is true when measured with neutrons. This difference in contrast again points toward the relative difference in the x-ray and neutron scattering lengths for oxygen.

In Fig. 3.38(a-f), diffuse neutron scattering in the $h = 3.5$ plane for all compositions is displayed, and cuts (Fig. 3.38(g-l)) are made through the scattering volumes to illustrate how the amplitude of the M point changes with composition. It is apparent that the M points

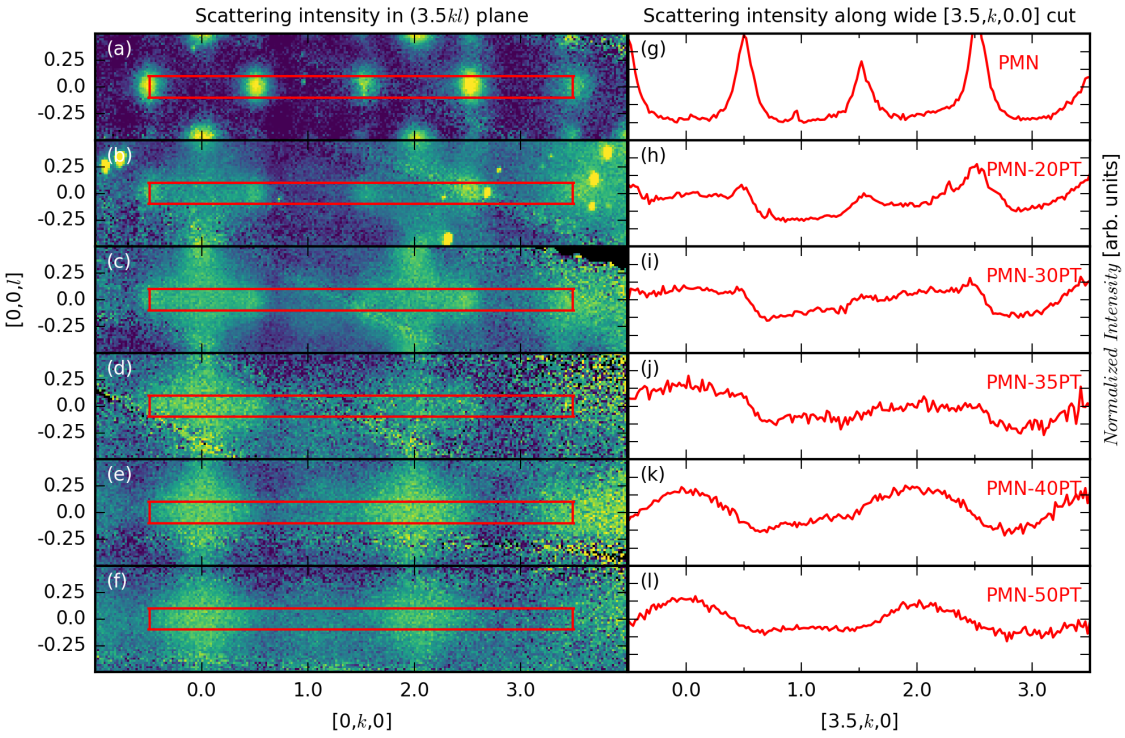

Figure 3.38: (a-f) Reciprocal space maps of the $3.5kl$ set of Brillouin zones in the $(hk0)$ plane measured at 6 K with neutrons for $x = 0\%, 20\%, 30\%, 35\%, 40\%$, and 50% respectively, integrated over a range of 0.2 r.l.u. in h. Intensity scales are logarithmic. (g-l) Corresponding cuts through the data in (a)-(e) along $(3.5, k, 0)$ with intensities integrated along h from 3.4 to 3.6 and along l from -0.1 to 0.1. The vertical scales are linear. Points from PMN-20PT that are dominated by a misaligned crystallite have been removed.

are strongest for $x = 0$, diminish in amplitude with increasing x, and are essentially absent at the MPB. This compositional dependence is displayed in Fig. 3.29(e), and a comparison with ΔT_{max} (Fig. 3.29(c)) shows a clear correlation between the relaxational character and the M-point intensity.

The *C2* compositional dependence thus strongly suggests a link between short-range antiferroelectric displacements and relaxor physics. Whereas *C1* is ferroic, *C2* is antiferroelectric in origin [71]. It is proposed that the compositional dependence revealed from this work supports a picture described by Tkachuk *et al.* [70] in which relaxor physics arises from competing ferroelectric and antiferroelectric interactions [70]. Indeed, this idea is

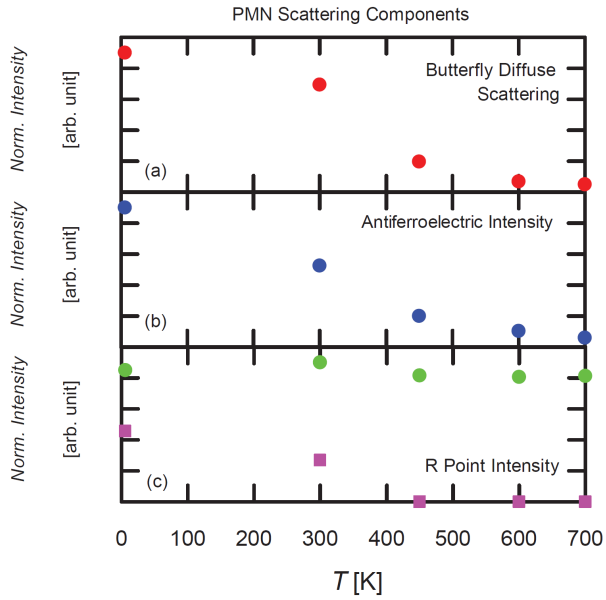

Figure 3.39: Temperature dependence of (a) *C1*, (b) *C2*, and (c) *C3* diffuse scattering components as measured with neutron scattering in PMN. The green circles in (c) show intensity of the (2.5, 0.5, 0.5) peak, and the magenta squares show intensity of the (3.5, 0.5, 0.5) peak. Vertical scales are linear.

consistent with recent theoretical work of Sherrington [55], who described the relaxor state as a soft glass resulting from frustration between competing ferroelectric and antiferroelectric interactions, analogous to a spin glass resulting from frustration between ferromagnetic and antiferromagnetic states. In this picture, which may extend to relaxor systems beyond PMN-xPT such as BZT [56], the ferroic interactions leading to *C1* are inhibited by the antiferroelectric interactions underlying *C2*.

The temperature dependence of *C2* also shows a link to some transitional behavior. High-temperature experiments on PMN indicate a temperature dependence of *C2* similar to that of *C1*, with both being reduced in intensity around $T_m(f)$ and being suppressed entirely above the Burns temperature T_d; this is consistent with the x-ray measurements made over a lesser range.

3.3.3 *C3*: R-point Scattering

Another feature of the diffuse scattering, *C3*, is observed at the zone-boundary R points. This feature is composed of broad peaks somewhat similar to *C2*, but the peaks at the R points have a distinct temperature dependence. The temperature dependence for all *C3* peaks is not identical; for example, the $\frac{7}{2}\frac{1}{2}\frac{1}{2}$ peak is suppressed at higher temperatures, while the $\frac{5}{2}\frac{1}{2}\frac{1}{2}$ peak retains most of its intensity up to 700 K. This suggests two contributions to *C3*: a temperature-dependent part of similar origin to *C2* and a temperature-independent part of chemical origin (see Fig. S4). The temperature-independent scattering, similar to scattering originally revealed in transmission electron microscopy (TEM) studies [72] and later seen in x-ray measurements [70, 85] almost certainly arises from some ordering of B-site cations. While too broad to be produced by highly-ordered large domains, this scattering indicates short-range rock-salt ordering, with nearest-neighbor pairs of Mg-Mg atoms less likely to occur than would be expected from a random distribution. Our neutron measurements show that this ordering diminishes with increasing x (Fig. 3.29(f)) which is consistent with the findings of transmission electron microscopy [72]. Clearly, the B-site (2+/5+) ordering occurs to minimize the local Coulomb energy, as it is impossible for this order to persist over long distances in PMN-xPT and maintain charge neutrality. As Ti^{4+} ions are introduced with increasing x, the propensity for the charge ordering is diminished.

Burton *et al.* have discussed the importance of chemical short-range order in seeding locally polar regions in $PbSc_{1/2}Nb_{1/2}O_3$ [54]; however, while there certainly is a correlation between the local cation ordering (Fig. 3.29(f)) and the relaxational dielectric behavior (Fig. 3.29(c)), there is no obvious correlation to *C1*, which is often associated with polar nanoregions (Fig. 3.29(d)). Recent theoretical work by Prosandeev *et al.* has suggested that local cation ordering is associated with increased antiferroelectric activity [86]. While

this may explain the similar dependence of *C2* and *C3* intensities on Ti concentration, it is important to note the absence of *C3* intensity near the MPB. This indicates that where ferroic properties are maximal, B-site cations are randomly distributed, and a highly-ordered arrangement of these atoms cannot be responsible for the large d_{33} in morphotropic PMN-xPT.

A type of B-site order typically proposed for PMN uses an ordered, two-sublattice model, with two sites, S and S', each having $c_j = 0.5$ [86]. The S lattice in this case is occupied entirely by Nb atoms, and the S' site is randomly occupied by $\frac{2}{3}$ Mg atoms and $\frac{1}{3}$ Nb atoms. This arrangement can be shown to map linearly onto a description of chemical short-range order defined directly by correlations between Mg and Nb occupancies; in this more natural description, one has $\alpha_{100}^{Mg-Nb} = -\alpha_{110}^{Mg-Nb} = -0.5$, with the $|\alpha_{lmn}^{Mg-Nb}| = 0.5$ for all $lmn \to \infty$. Such an arrangement could be considered to be the maximally ordered case for PMN. Simulated in *DISCUS*, this maximal order case results in R point peaks far sharper than the ones observed experimentally: calculated scattering from a simulated crystal of maximally ordered PMN shows R point peaks with full-width half-maximum of at most 0.004 r.l.u., while observed *C3* peaks have a much larger reciprocal space full-width half-maximum of roughly 0.074 r.l.u. An arrangmement more consistent with the observed data will clearly have a reduced α_{100}^{Mg-Nb} that decays to zero for finite lmn.

A simple model, setting only α_{100}^{Mg-Nb} and allowing larger lmn to follow, produces peaks on R points with width inversely proportional to $\alpha_{\langle 100\rangle}^{Mg-Nb}$. Table 3.3 shows these results, with an $\alpha_{\langle 100\rangle}^{Mg-Nb} = -0.25$ coming closest to the experimental result. While this model is certainly too simple to quantitatively reproduce *C3*, it does show that relatively small short-range chemical ordering of the B site can produce something like what is observed experimentally. Further investigation is likely to show some important correlations for $\alpha_{\langle 110\rangle}^{Mg-Nb}$ or $\alpha_{\langle 111\rangle}^{Mg-Nb}$ beyond what would be expected to result from the nearest-neighbor $\alpha_{\langle 100\rangle}^{Mg-Nb}$ alone.

Table 3.3: Using a Levenberg-Marquardt least-squares fitting algorithm provided by the lmfit package for Python, Gaussian widths were assigned to the $\frac{3}{2}\frac{1}{2}\frac{1}{2}$ peak as measured with x-ray scattering from PMN at 100 K and also to the same peak from PMN crystals simulated by DISCUS. The simulated crystals had $\alpha^{Mg-Nb}_{\langle 100\rangle}$ set to a given value and were then generated via a Monte Carlo process optimized for the target α^{Mg-Nb}_{100}.

$\alpha^{Mg-Nb}_{\langle 100\rangle}$	Gaussian Width (r.l.u.)
-0.10	0.260
-0.15	0.131
-0.20	0.139
-0.25	0.069
-0.30	0.053
-0.35	0.028
-0.40	0.029
-0.45	0.037
-0.50	0.037
-0.50^*	0.004

*Maximally-ordered crystal, with $\alpha^{Mg-Nb}_{\langle lmn\rangle} = \pm 0.5$ for all lmn.

3.3.4 *C4*: Size-Effect Scattering

A fourth diffuse scattering component, titled here as *C4*, was observed in both our neutron and x-ray measurements. This component appears as extremely broad scattering that has a pseudo-octahedral shape centered at X points $\frac{1}{2}(2h+1, 2k, 2l)$ as marked by the yellow circles in Fig. 3.30. The compositional dependence is apparent from the broad humps centered at the X points in the cuts shown in Fig. 3.38 (see, e.g., panel (j)), and the compositional dependence is displayed in Fig. 3.29(g). This feature has its own modulation across Brillouin zones, with strong and weak octahedra forming a checkerboard pattern in reciprocal space. It is important to note that this modulation is not identical to that of *C1*.

While *C4* scattering appears in very similar forms in PMN-20PT through PMN-50PT, it is weaker and less well-defined in pure PMN.

This feature has been previously observed in numerous experiments [57, 63] as a "lock" into which *C1* scattering fits into as a "key," but its origin does not seem to have been investigated; indeed, it had not been appreciated as a feature independent from other diffuse scattering. An immediately relevant point is that *C4* exists for all compositions measured ($x = 0$ to $x = 0.5$); it grows initially upon increasing x, and is thus not directly correlated to the dielectric properties, electromechanical coupling, nor the long-range polar order. It exists independently of both *C1* and *C2*, clearly having a distinct temperature and compositional dependence from either of these other features while it impinges upon these other features in reciprocal space.

C4 is reminiscent of the diffuse scattering that arises in binary alloys due to atomic size mismatch – indeed, a formal treatment of Cu_3Au found as an example in [10] shows a slowly-varying background alternating in intensity between zones quite similar to that seen in PMN-xPT. This suggests that differences between the average Pb-Mg, Pb-Nb, and Pb-Ti nearest-neighbor distances produce this feature. Further supporting this conclusion is the fact that this scattering is much more clearly seen with x-rays than it is with neutrons; this is well-explained by the x-ray scattering lengths of Pb and the possible B site cations being relatively larger than their corresponding neutron scattering lengths.

Within the region of study, this feature has only weak temperature dependence; at least, the background underneath *C4* seems to change more quickly than the feature itself does. The high-temperature data from PMN was not sufficient to accurately resolve this feature. Comparison between cuts at low temperature and high temperature in x-ray scattering from PMN-30PT shows little change in intensity from 100 K to 400 K; the background changes more than the feature itself does, . While this feature is much weaker when measured with neutrons, *C4* seems to slightly change above T_C in various compounds, particularly in regions

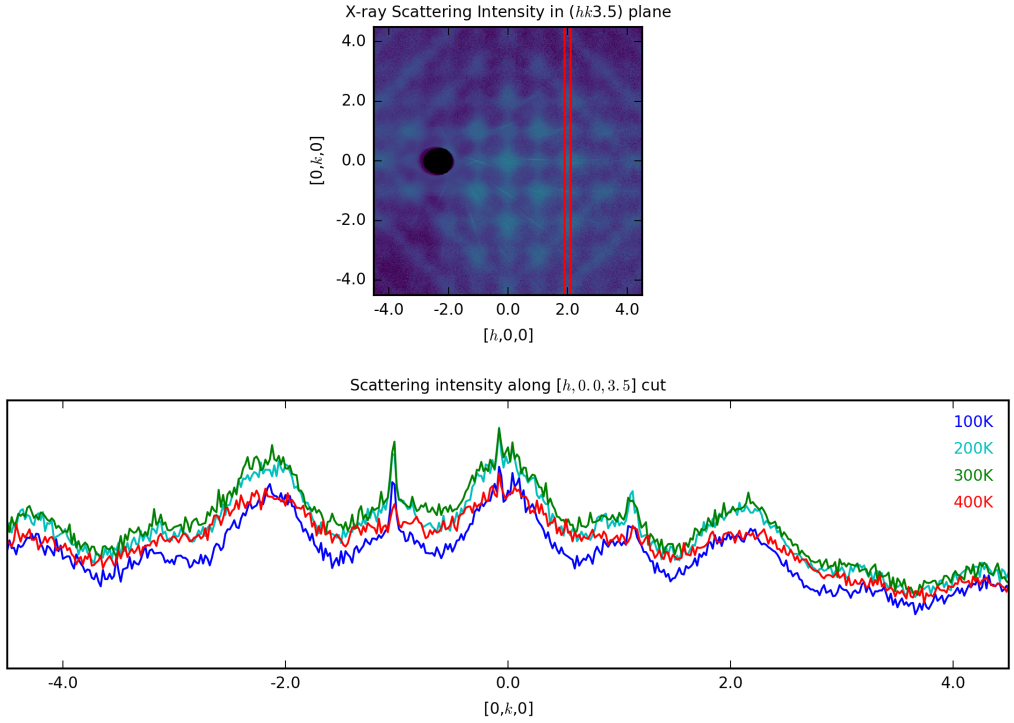

Figure 3.40: Diffuse x-ray scattering near $h00$ zones. The asymmetry between low-$|\mathbf{Q}|$ and high-$|\mathbf{Q}|$ diffuse scattering is significantly larger for neutron scattering than it is for x-ray scattering, indicating a role for correlated oxygen displacements.

far from $\langle h00 \rangle$ directions, which may indicate a weakening of the local chemical size effect in comparison to thermal effects. It may be that this scattering is suppressed more noticeably above the Burns temperature T_B; further measurements would be helpful in this regard.

The scattering can be fit to diffuse scattering terms defined in Ch. 1.2. I_1 and I_2 terms were generated using lmn vectors corresponding to Pb to B-site and B-site to B-site distances, within a four unit cell cube, with the $\langle X^{ij}_{lmn} \rangle$ set proportional to their projection along lmn. These terms were then fit to observed and symmetrized x-ray scattering from PMN-30PT at 100 K in a relatively small region of reciprocal space bounded by the $h = \pm 2$, $k = \pm 2$, $l = 2$, and $l = 6$; Bragg peaks and surrounding *C1* scattering were also removed from this data and replaced with interpolated background, so that only *C4* scattering was used for fitting.

As the scattering is not symmetric across Bragg peaks but also not entirely antisymmetric, both I_1 and I_2 terms are required to model the observed scattering. The sum of terms qualitatively reproduce the checkerboard pattern of weak and strong octahedra (Fig. 3.41).

Table 3.4: Using a Levenberg-Marquardt least-squares fitting algorithm provided by the lmfit package for Python, the sum of a series of I_1 and I_2 diffuse scattering terms plus a linear background term was fitted to observed diffuse x-ray scattering data from PMN-30PT. The coefficient value for each term are normalized to the largest I_1 term, associated with $\langle lmn \rangle = \frac{1}{2}\langle 111 \rangle$ interactomic vectors, and only displayed if its absolute value is greater than 3% of that term.

$\langle lmn \rangle$ for I_1 term	Coefficient for I_1 term	$\langle lmn \rangle$ for I_2 term	Coefficient for I_2 term
$\frac{1}{2}\langle 111 \rangle$	1.0	$\langle 100 \rangle$	-0.520
$\langle 111 \rangle$	0.265	$\langle 110 \rangle$	-0.162
$\langle 110 \rangle$	0.183	$\frac{1}{2}\langle 111 \rangle$	-0.088
$\langle 100 \rangle$	-0.103	$\langle 200 \rangle$	-0.072
$\langle 200 \rangle$	0.079	$\langle 111 \rangle$	-0.044
$\langle 211 \rangle$	-0.046		
$\frac{1}{2}\langle 533 \rangle$	-0.031		

As expected, the largest terms by far are the ones within the unit cell (Tab. 3.4); as these results show, a decent qualitative fit can be obtained only using terms with a range within a few unit cells, with the most important terms being associated within a single unit cell and between. Unfortunately, the fit parameters are only the coefficients for the various terms. Each type of atomic pair will contribute to each of these terms, and without some contrasting images with different scattering lengths, disentangling the contributions from different atomic pairs is not possible. This is bad enough for I_1 terms, which only depend on Pb to B site displacement correlations; for the I_2 term, contributions from the B site sublattice and Pb sublattice cannot even be separated! While this technique does yield the reasonable

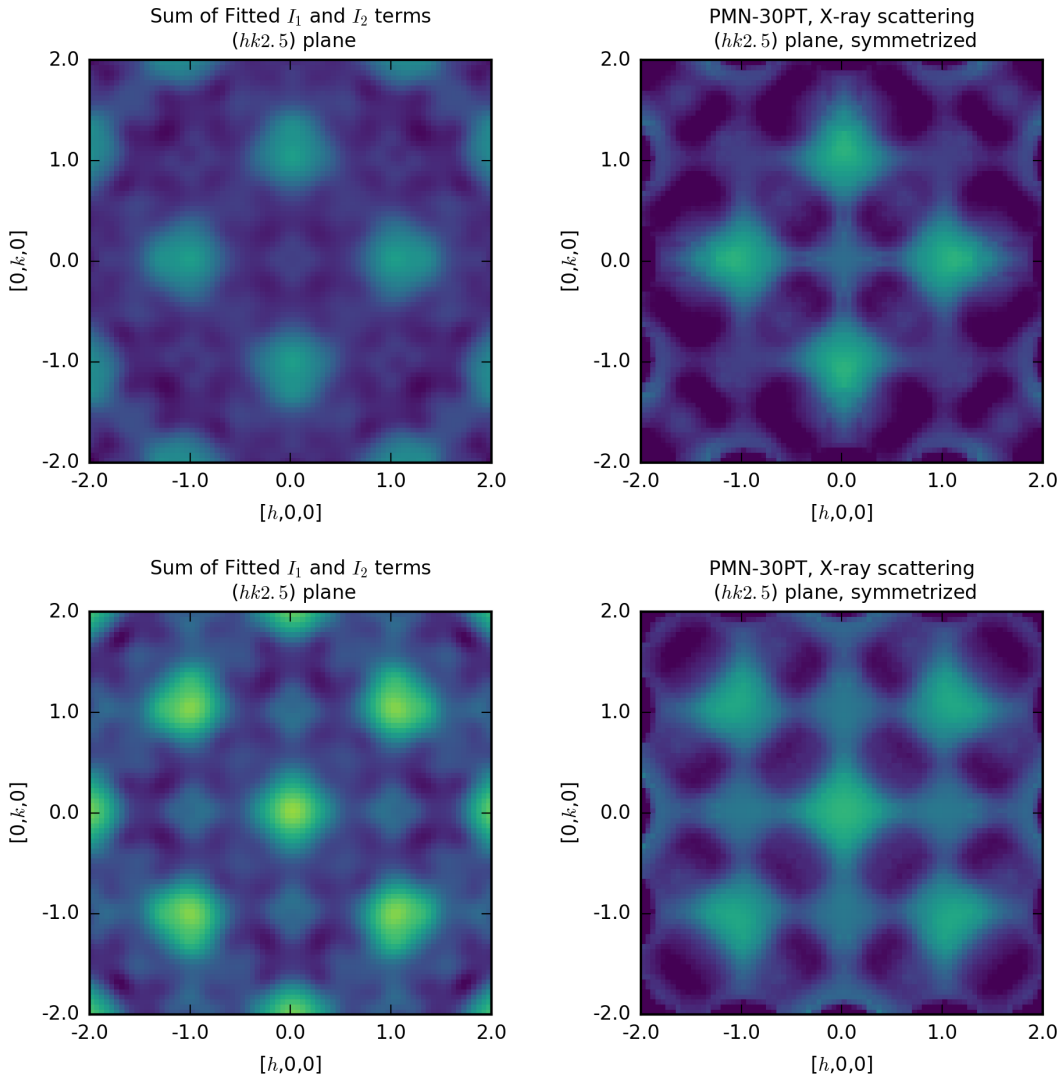

Figure 3.41: A series of I_1 and I_2 scattering terms with $lmn < (4, 4, 4)$ were generated, and their sum was fit to symmetrized *C4* x-ray scattering from PMN-30PT.

and valuable result that distortions within a few unit cells are capable of reproducing the observed *C4* scattering, it cannot plausibly yield any more specific information.

A simulation is again instructive. Using *DISCUS*, a PMN-30PT crystal is generated and oxygen atoms eliminated for efficiency in calculation. The average Pb atom to B site distance is then made dependent upon the occupancy of the B site: Pb atoms move away from Nb^{5+} cations and towards both Mg^{2+} and Ti^{4+} cations. This qualitatively replicates the observed pattern of diffuse octahedra of *C4* (Fig. 3.42). The Monte Carlo simulation used to generate the model crystal uses a Lennard-Jones potential between Pb atoms and their eight nearest-neighbor B sites. In the simulation, compared to the average Pb to B site distance, the Pb-Mg nearest-neighbor distance is 2% smaller, the Pb-Nb distance is 2% larger, and the Pb-Ti distance is 3% smaller. While only nearest-neighbor distances are considered in the Monte Carlo simulation, more distant pairs are also affected 3.5. This model reproduces the same checkerboard pattern of strong and weak diffuse octahedra observed in experiment.

C4 scattering might be expected to be absent in pure $PbTiO_3$, but the amount expected in the inherently inhomogeneous $PbMg_{1/3}Nb_{2/3}O_3$ is less clear. While *C4* scattering in PMN is clearly weaker than it is in more Ti-rich materials, it seems odd that the difference between Pb-Mg and Pb-Nb nearest-neighbor distances producing *C4* in PMN-30PT would not be present in PMN. Repeating the *DISCUS* simulation for pure PMN while varying the chemical ordering of the B site is instructive. If the B site is randomly occupied, a simple Pb to B-site size effect will produce scattering similar to that observed in PMN-30PT. Adding chemical short-range order by setting $\alpha_{100}^{Mg-Nb} = -0.25$ weakens the resulting pattern considerably, and imposing the maximum amount of B-site order changes the scattering further still, while adding the expected sharp superlattice peaks at R points. This simulation suggests that the weaker *C4* scattering seen in pure PMN compared to samples containing Ti is not necessarily due to weaker local distortions, but rather to the effect of chemical order on the scattering produced by local distortions.

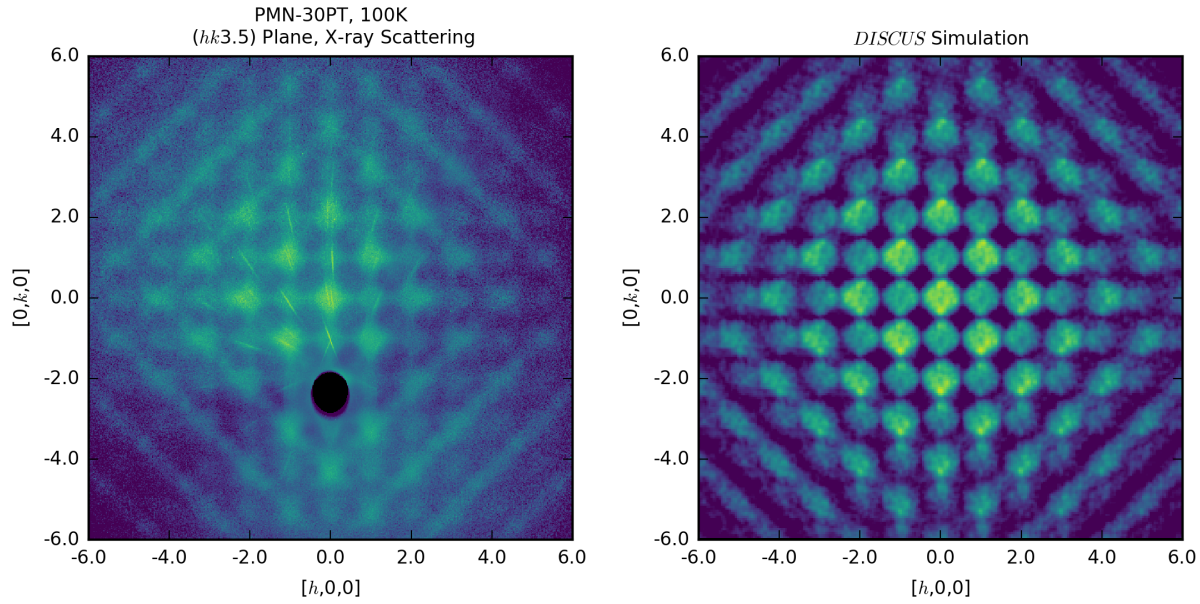

Figure 3.42: Simulated x-ray scattering data (right) reproduces the *C4* feature seen in experimental x-ray scattering from PMN-30PT. The simulated crystal makes average Pb-Nb nearest neighbor distances larger than average by 2.6%, and Pb-Mg and Pb-Ti distances smaller by 1.2% and 2.2% respectively. While only nearest-neighbor potentials are considered for the Monte Carlo simulation, larger interatomic vectors are also affected.

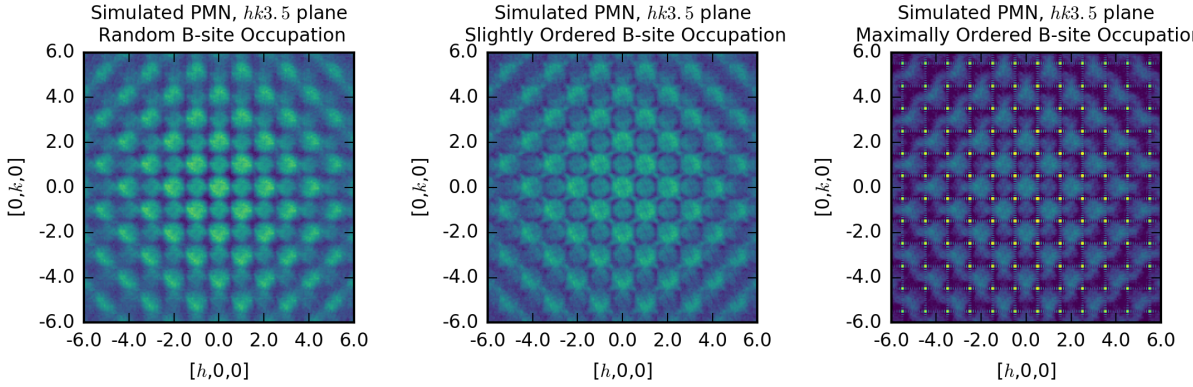

Figure 3.43: Simulated x-ray scattering from PMN crystals with differing levels of chemical order on the B site. On the left, Mg and Nb atoms are randomly distributed; in the center, Mg and Nb atoms have an $\alpha^{\text{Mg-Nb}}_{\langle 100\rangle} = -0.25$; on the right, Mg and Nb atoms are maximally ordered as described in Ch. 3.3.3, with $|\alpha^{\text{Mg-Nb}}_{lmn}| = 0.5$ for all lmn. Strong lines connecting R points in the maximally-ordered panel are a artifact of the finite size of the simulated crystal.

Table 3.5: Distances between various atomic pairs in the simulated PMN-30PT crystal used to generate Fig. 3.42. The distance $d^{ij}_{\langle lmn\rangle}$ represents the average distance between an ij pair of atoms separated by vector $\langle lmn\rangle$ in an undistorted crystal; $D_{\langle lmn\rangle}$ represents the undistorted distance.

d^{ij}_{lmn}	d^{ij}_{lmn}/D_{lmn}	d^{ij}_{lmn}	$d^{ij}_{lmn}/\ D_{lmn}$	d^{ij}_{lmn}	$d^{ij}_{lmn}/\ D_{lmn}$
$d^{\text{Pb-Nb}}_{\frac{1}{2}\langle 111\rangle}$	1.026	$d^{\text{Pb-Mg}}_{\frac{1}{2}\langle 111\rangle}$	0.988	$d^{\text{Pb-Ti}}_{\frac{1}{2}\langle 111\rangle}$	0.977
$d^{\text{Pb-Nb}}_{\frac{1}{2}\langle 311\rangle}$	1.000	$d^{\text{Pb-Mg}}_{\frac{1}{2}\langle 311\rangle}$	1.001	$d^{\text{Pb-Ti}}_{\frac{1}{2}\langle 311\rangle}$	1.001
$d^{\text{Pb-Nb}}_{\frac{1}{2}\langle 331\rangle}$	1.002	$d^{\text{Pb-Mg}}_{\frac{1}{2}\langle 331\rangle}$	1.000	$d^{\text{Pb-Ti}}_{\frac{1}{2}\langle 331\rangle}$	0.999
$d^{\text{Pb-Nb}}_{\frac{1}{2}\langle 333\rangle}$	1.002	$d^{\text{Pb-Mg}}_{\frac{1}{2}\langle 333\rangle}$	0.999	$d^{\text{Pb-Ti}}_{\frac{1}{2}\langle 333\rangle}$	0.998
$d^{\text{Pb-Nb}}_{\frac{1}{2}\langle 555\rangle}$	1.000	$d^{\text{Pb-Mg}}_{\frac{1}{2}\langle 555\rangle}$	1.000	$d^{\text{Pb-Ti}}_{\frac{1}{2}\langle 555\rangle}$	1.000
$d^{\text{Nb-Nb}}_{\langle 100\rangle}$	0.988	$d^{\text{Mg-Mg}}_{\langle 100\rangle}$	1.008	$d^{\text{Ti-Ti}}_{\langle 100\rangle}$	1.012
$d^{\text{Nb-Ti}}_{\langle 100\rangle}$	1.002	$d^{\text{Nb-Mg}}_{\langle 100\rangle}$	0.999	$d^{\text{Mg-Ti}}_{\langle 100\rangle}$	1.011
$d^{\text{Nb-Nb}}_{\langle 110\rangle}$	1.007	$d^{\text{Mg-Mg}}_{\langle 110\rangle}$	0.995	$d^{\text{Ti-Ti}}_{\langle 110\rangle}$	0.992
$d^{\text{Nb-Ti}}_{\langle 110\rangle}$	1.001	$d^{\text{Nb-Mg}}_{\langle 110\rangle}$	1.003	$d^{\text{Mg-Ti}}_{\langle 110\rangle}$	0.994
$d^{\text{Nb-Nb}}_{\langle 111\rangle}$	1.013	$d^{\text{Mg-Mg}}_{\langle 111\rangle}$	0.993	$d^{\text{Ti-Ti}}_{\langle 111\rangle}$	0.990
$d^{\text{Nb-Ti}}_{\langle 111\rangle}$	0.999	$d^{\text{Nb-Mg}}_{\langle 111\rangle}$	1.002	$d^{\text{Mg-Ti}}_{\langle 111\rangle}$	0.992
$d^{\text{Nb-Nb}}_{\langle 200\rangle}$	0.999	$d^{\text{Mg-Mg}}_{\langle 200\rangle}$	1.000	$d^{\text{Ti-Ti}}_{\langle 200\rangle}$	1.001
$d^{\text{Nb-Ti}}_{\langle 200\rangle}$	1.000	$d^{\text{Nb-Mg}}_{\langle 200\rangle}$	1.000	$d^{\text{Mg-Ti}}_{\langle 200\rangle}$	1.001

One model that reproduces something like *C4* scattering is the molecular dynamics simulation presented by Takenaka *et al.* [52]. While this type of scattering was not investigated by the authors, individual frames from their molecular dynamics simulation were made available for study. To resolve *C4* scattering in this model, scattering was calculated using *DISCUS* from Pb atoms only and with only oxygen atoms removed. By subtracting the Pb-only scattering from the oxygen-free total, the Pb to B-site and B site to B-site correlations thought to underlie *C4* were isolated from other contributions. At each of the three temperatures for which data was provided, a feature like *C4* was found in the isolated scattering.

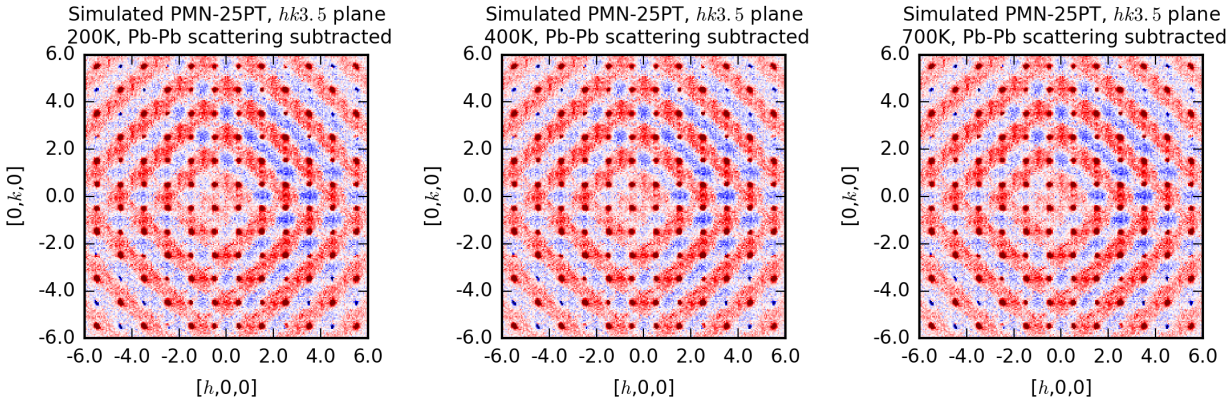

Figure 3.44: Simulated x-ray scattering a single frame from the molecular dynamics simulation from Ref. [52] at 200 K, 400 K, and 700 K; shown is the scattering from all Pb, Mg, Nb, and Ti atoms, with Pb only scattering subtracted. At all temperatures, the positive (red) regions include size-effect scattering similar to that observed in PMN.

While somewhat different from *C4* scattering found in PMN-20PT or PMN-30PT, it should be noted that the model imposed strong chemical order on the B site, with two sublattices forming a rock-salt structure; one sublattice is entirely occupied by Nb atoms, and the other randomly occupied by Mg and Ti atoms. This chemical ordering produces sharp superlattice peaks at R points, and as previously shown, chemical ordering suppresses the intensity of *C4*. It can thus be expected that *C4* scattering from this model of PMN-25PT will be more like that from PMN, which appears to be the case.

While further study is needed to better understand *C4*, this scattering feature shows that Pb displacements are correlated to B-site neighbors. While not obviously connected to any bulk properties, it is important to recognize the presence of *C4* because it can easily lead to confusion when interpreting diffuse scattering measurements made within a single Brillouin zone. The presence of this scattering also highlights the inhomogeneity of chemical environment within PMN-xPT.

CHAPTER 4

ELECTRIC FIELD EFFECTS ON DIFFUSE SCATTERING FROM PMN-30PT

The most useful property of PMN-xPT is its large piezoelectric coupling for compositions near the morphotropic phase boundary. The effect of an applied electric field on diffuse scattering from PMN-xPT is thus a natural avenue for investigation. Previous studies have clearly shown the connection between *C1* scattering and electric fields; indeed, this connection fundamentally shows that *C1* scattering is ferroic in nature. With the new structure of *C1* and the existence of *C4* size-effect scattering established in the previous chapter, new questions arise. How does the asymmetry of *C1* change with the application of an electric field – do oxygen displacements continue to have an effect? Do the changes in *C1* previously observed in low-$|\mathbf{Q}|$ zones manifest similarly in a wider range of Brillouin zones? How do the chemically-driven displacements causing *C4* change – are local displacement correlations overwhelmed by the external field?

Additional experiments were conducted in an attempt to answer these questions. Both neutron and x-ray diffuse scattering experiments were performed on PMN-30PT with and without an electric field applied along high-symmetry directions so that changes in the diffuse scattering could be measured.

4.1 X-ray Scattering Experiments

To investigate diffuse x-ray scattering from PMN-30PT under an applied field, two single crystals previously procured for unrelated experiments were used. Each single crystal consisted of a large plate, originally 10 mm × 10 mm × 0.5 mm, with the large surfaces cut along the [010] and [111] faces. These large surfaces were coated with a thin layer of Pt, allowing for the application of an appoximately uniform electric field. To allow for an x-ray scattering experiment, pieces chipped away from the samples, leaving a rough rectangular prism 0.5 mm thick and approximately 2 mm wide as a target for the incident beam (Fig. 4.1). The sample was then clamped at its base by copper contacts, across which a potential difference could be applied. The voltage source used had a maximum potential difference of 300 V; for each sample, scattering was measured with applied fields of 0 kV/cm, 1.5 kV/cm, 3 kV/cm, 6 kV/cm, and finally with the voltage source set back to 0 V to check for hysteresis. Experiments were conducted at room temperature in ambient atmosphere; samples were assumed to be unpolarized prior to the beginning of the experiment, and no effort was made to depolarize them by raising their temperature above T_C. At the beginning of the scattering experiment, samples were not carefully field-cooled or zero-field-cooled; it was assumed that time and handling sufficed to bring them to an unpolarized state.

The leads through which the voltage was applied made a full 360° rotation inaccessible on the available goniometer, so data were collected over a 200° range. Multiple scans were performed at each voltage to improve statistics. Some artifacts from an insulated wire eventually creeping into the incident beam path are observed during some runs, particularly in the data collected from the [010] oriented crystal. For each field examined, four sets of three scans were performed, with each set taking approximately two hours to complete. Counts were normalized to the incident beam monitor.

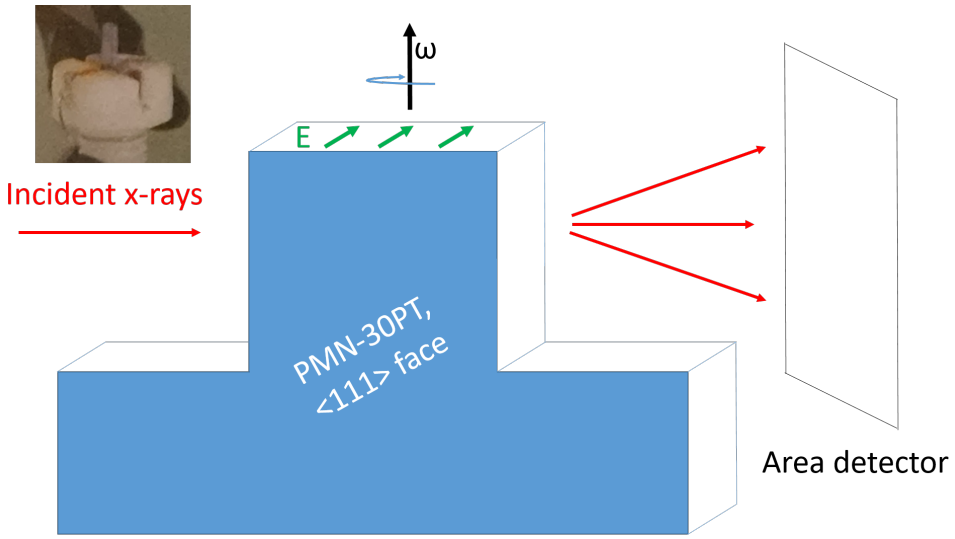

Figure 4.1: Schematic and inset photo of [111]-cut sample and goniometer used for diffuse x-ray scattering measurements from PMN-30PT with applied electric field. The x-ray beam (red) was incident upon the rectangular region jutting up from the goniometer, while copper contacts clamped the lower part of the sample into place and allowed for a potential difference to be applied to the thin platinum contacts deposited on the surfaces (blue). The sample was then rotated about the ω axis to survey a volume of reciprocal space.

Measurements taken from the sample with surfaces cut along [111] faces proved most useful. Measurements before the application of an electric field showed diffuse scattering like that seen in the experiment where no field could be applied (Ch. 3.2); it can be safely concluded that the sample began in an unpolarized state. Under an applied electric field in the [111] direction (i.e., parallel to the normal vector to the crystal faces), *C1* scattering showed a clear redistribution. Lobes of *C1* scattering features parallel to [110], [101], and [011] were enhanced and sharpened, while lobes parallel to $[1\bar{1}0]$, $[10\bar{1}]$, and $[01\bar{1}]$ were suppressed (Fig. 4.2). This effect is clearly established even at 1.5 kV/cm, the lowest applied field, and clearly establishes the link between *C1* and ferroelectric behavior.

C4 scattering also shows some redistribution under an applied field. The effect is more subtle than that seen in *C1*; it is almost impossible to see with the naked eye given the variations in background, and even line cuts show only small variations. A plot of the

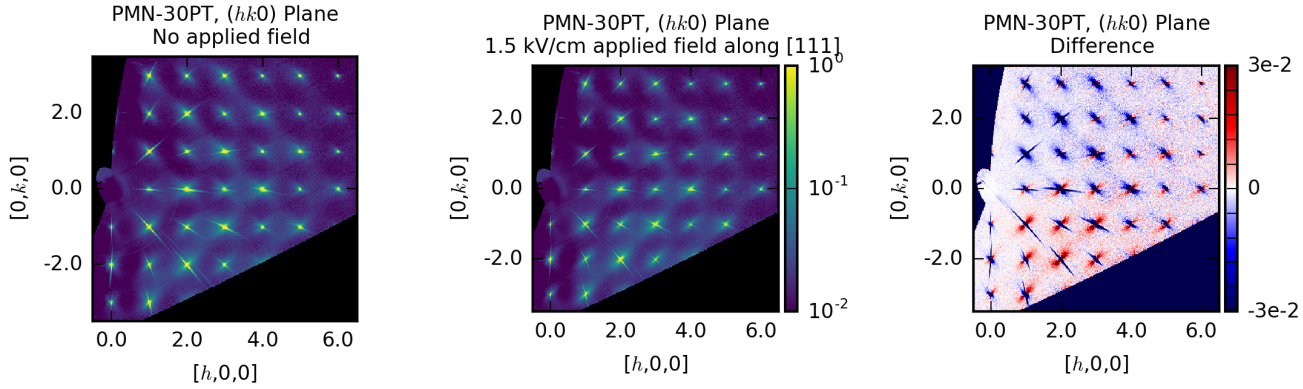

Figure 4.2: *C1* diffuse scattering in the $hk0$ plane is redistributed under an applied field in the [111] direction. Left panel shows scattering with no applied field, the middle panel with a field strength of 1.5 kV/cm, and the right panel shows the difference between the two, with blue indicating regions with stronger scattering with no applied field and red indicating regions with stronger scattering under the applied field.

difference between scattering under no applied field and scattering under an applied field shows a small but systematic change in *C4* diffuse scattering (Fig. 4.3).

The experiments on the [010]-cut sample appeared to show some redistribution of ferroic intensity. While initially intriguing, further examination of these data at the highest applied field showed that the redistribution displayed differently around $[h00]$ peaks than around $[00l]$ peaks, which should be equivalent under an applied field along the [010] direction (Fig. 4.9). As the field is thus likely not well-approximated as being along [010] and is in fact of undetermined direction, useful conclusions cannot be drawn from these data. Indeed, while the symmetry broken in the observed scattering around $h00$ peaks appeared to be consistent with that broken by the applied [010] field, this would in fact break Friedel's Law; it would be distinguishable from that generated from the opposite applied field, which would presumably differ only by reflection across the $k = 0$ plane and thus be an inversion of the original structure.

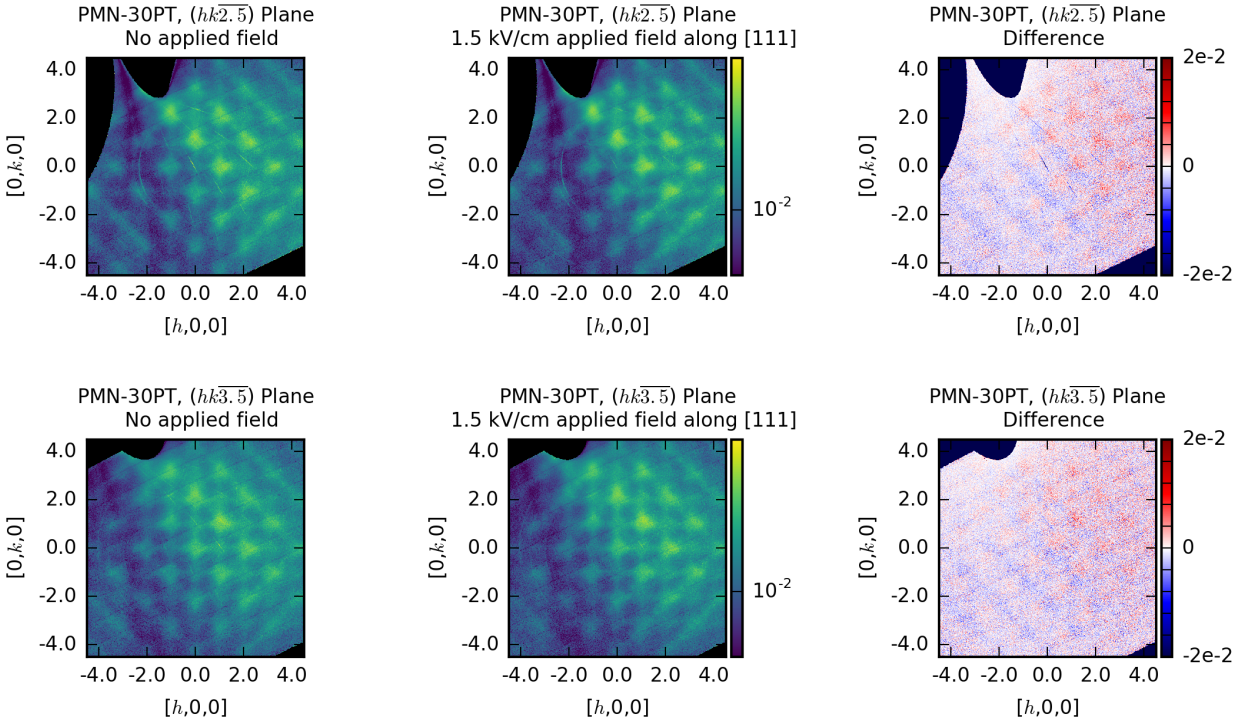

Figure 4.3: *C4* diffuse scattering in the $hk\overline{2.5}$ and $hk\overline{3.5}$ planes changes slightly under an applied field in the [111] direction. Left panel shows scattering with no applied field, the middle panel with a field strength of 1.5 kV/cm, and the right panel shows the difference between the two, with blue indicating regions with stronger scattering with no applied field and red indicating regions with stronger scattering under the applied field.

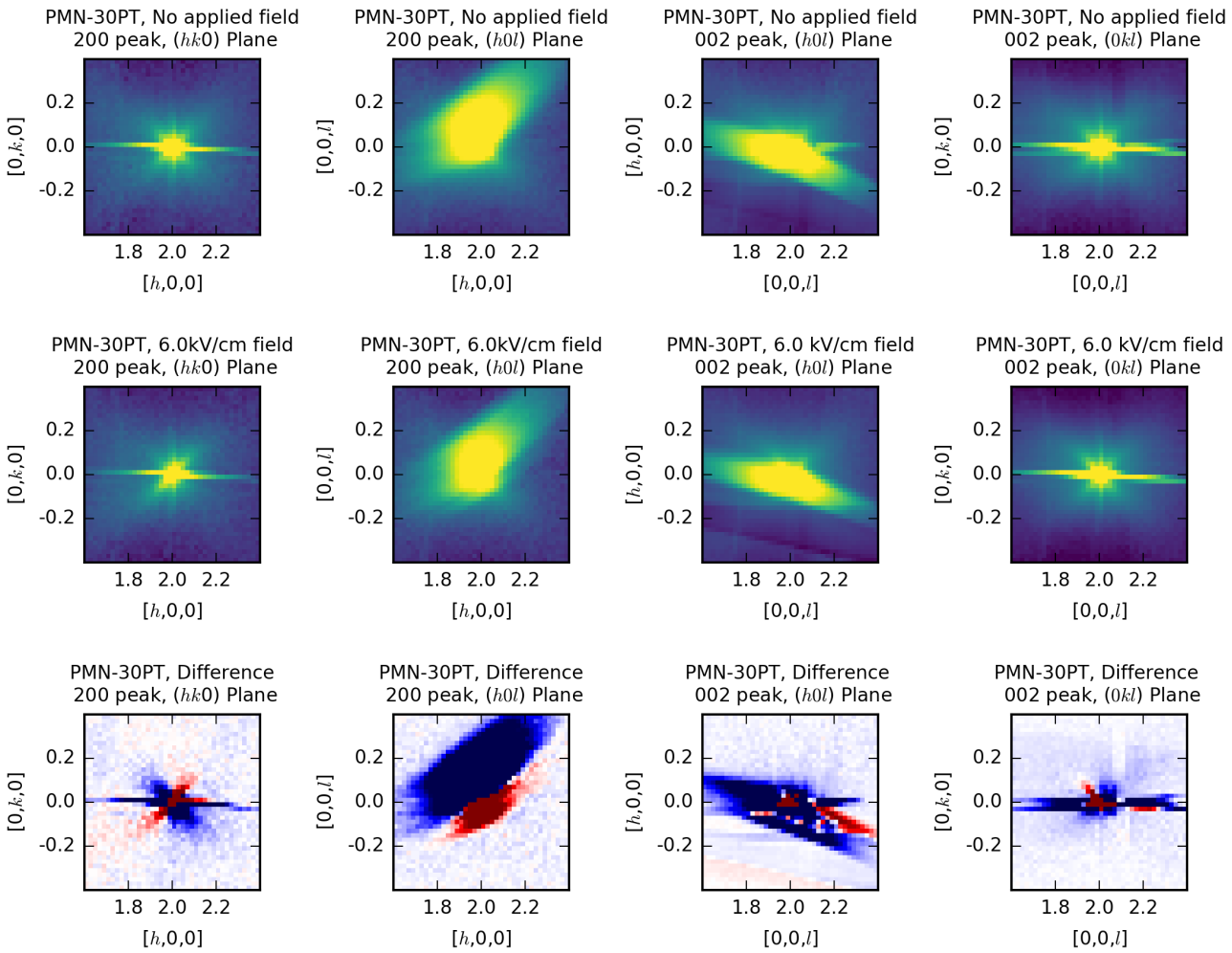

Figure 4.4: *C1* diffuse scattering is redistributed by an electric field of 6.0 kV/cm, nominally applied along the [010] direction. Compton scattering artifacts obscure some planes, but the $(hk0)$ plane around the 200 peak and the $(0kl)$ plane around the 002 peak should show equivalent scattering if the only broken symmetry is along [010]; this is clearly not the case.

4.2 Neutron Scattering Experiments

Neutron scattering experiments were performed using the triple-axis diffractometer BT-7 at the NCNR. BT-7 provides a number of advantages over *Corelli*, including well-understood sample environments for the application of an electric field and exceptional energy resolution in elastic mode. New samples, much larger than the samples used in x-ray scattering measurements and better suited for neutron scattering measurements , were procured for this purpose. However, BT-7 is built to take point scans[1] and is thus inherently ill-suited to measuring volumes of diffuse scattering. Given how well diffuse scattering from the material has been characterized, the strategy was to use a small number of well-chosen 'cuts' showing the relevant features of diffuse scattering and see how these proxy features changed under the field. With these features already well-characterized in PMN-30PT by the zero-field *Corelli* experiments, the qualitative change under an electric field can be well-contextualized.

Two single crystals of PMN-30PT were available for the experiment, both 10 mm x 10 mm x 5 mm, with thin gold contacts applied to the opposing 10 mm x 10 mm faces. One sample was cut along [010] faces, and the other was cut along [110] faces. Each crystal was heated to 500 K, above T_C for PMN-30PT, for an hour prior to mounting. Each crystal was then mounted to a boron nitride post with binary epoxy, with leads to a voltage source soldered to the contacts; the leads and the post were then shielded with cadmium to reduce background. The post was then placed in an closed-cycle refrigerator and mounted in BT-7; while the temperature was kept at room temperature, the sample was under a vacuum during measurements. An incident beam energy of 41.0 meV was used to access scattering

[1] BT-7 *does* have a position-sensitive detector, but it had not been characterized at the higher energies utilized for this experiment and was thus not recommended for use by the instrument scientists present for these experiments.

near higher-$|Q|$ peaks, horizontal collimations were set to 10' - 80' - 25' - 25,' and the final energy detected was set to 41.0 meV, meaning only elastic scattering was measured.

For the [110] sample, scans were taken around four Bragg peaks: 300, 400, 220, and $2\bar{2}0$ (Fig. 4.5). A 'circle scan' measured scattered intensity at points of constant $|\mathbf{q}| = 0.08$ r.l.u. around each peak. and line scans were taken at $h \pm 0.08$ for each peak. Each scan was performed first under no applied field, again after a potential of +2.5 kV was applied to the electrodes, and once more with a potential of -2.5 kV, for applied fields of 0 kV/cm, +5 kV/cm, and -5 kV/cm.

These scans show a change in the intensity of different lobes of *C1* scattering (Fig 4.6). Some lobes are sharpened and grow in intensity under the applied field, while other lobes are suppressed. The lobes that are sharpened and intensified are parallel to the applied [110] field; the lobes that are weakened are parallel to $[1\bar{1}0]$. The asymmetry in diffuse lobes observed with *Corelli* in zero-field scans is seen again in these measurements, with both suppressed and enhances lobes of scattering maintaining the asymmetry of scattering intensity between high-$|\mathbf{Q}|$ and low-$|\mathbf{Q}|$ regions.

For the [010] sample, scans were taken around five Bragg peaks: 300, 400, 030, 040, and 220. For each peak, a 'circle scan' measured scattered intensity at 36 points of constant $|\mathbf{q}| = 0.08$ r.l.u. around the peak; additional line scans were taken at $h \pm 0.08$ for the 300, 400, and 220 peaks and at $k \pm 0.08$ for the 030 and 040 peaks. The scans are graphically represented in Fig. 4.7. These scans were chosen to best investigate the change in *C1* diffuse scattering, as each would intersect with a lobe of this type of diffuse scattering. These scans were conducted with an applied potentials of 0 kV, 2.5 kV, and -5 kV; across the 0.5 cm width of the sample, this led to applied fields of 0 kV/cm, 5 kV/cm, and -10 kV/cm.

Compared to the [110] field, the [010] field has little effect on diffuse neutron scattering (Fig. 4.8). While there are shifts in diffuse intensity seen in the circle scans, no lobe of scattering appears to be suppressed by the application of the field. This is consistent with a

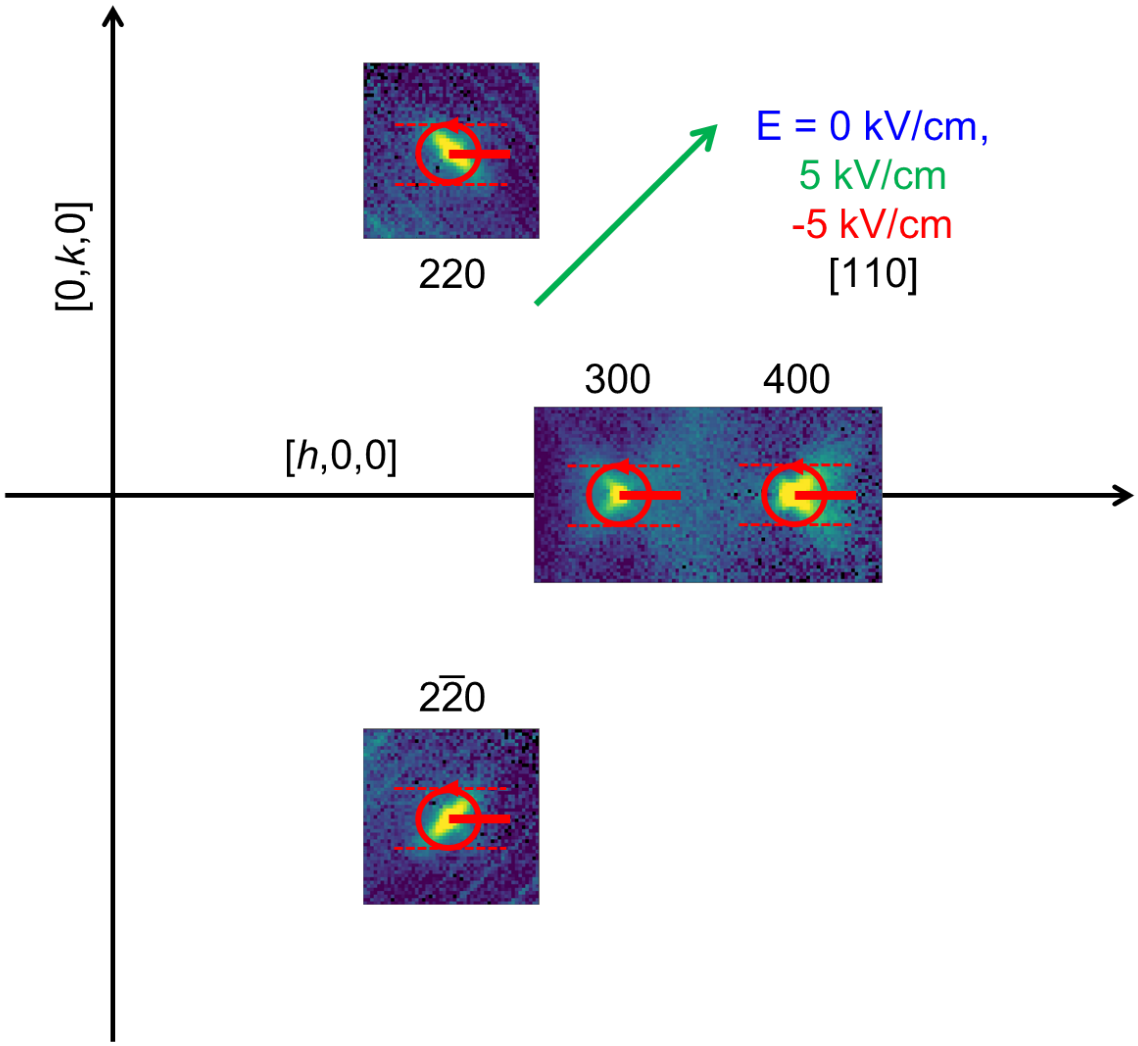

Figure 4.5: Point scans of neutron scattering taken from [110] cut of PMN-30PT using BT-7. Color images of diffuse scattering at each point are from *CORELLI* experiment to show zero-field measurement, dashed red lines show line scans taken, solid red circles show the constant $|\mathbf{q}|$ scan taken around each Bragg peak, and the solid red line define the $\theta = 0$ for each circle scan.

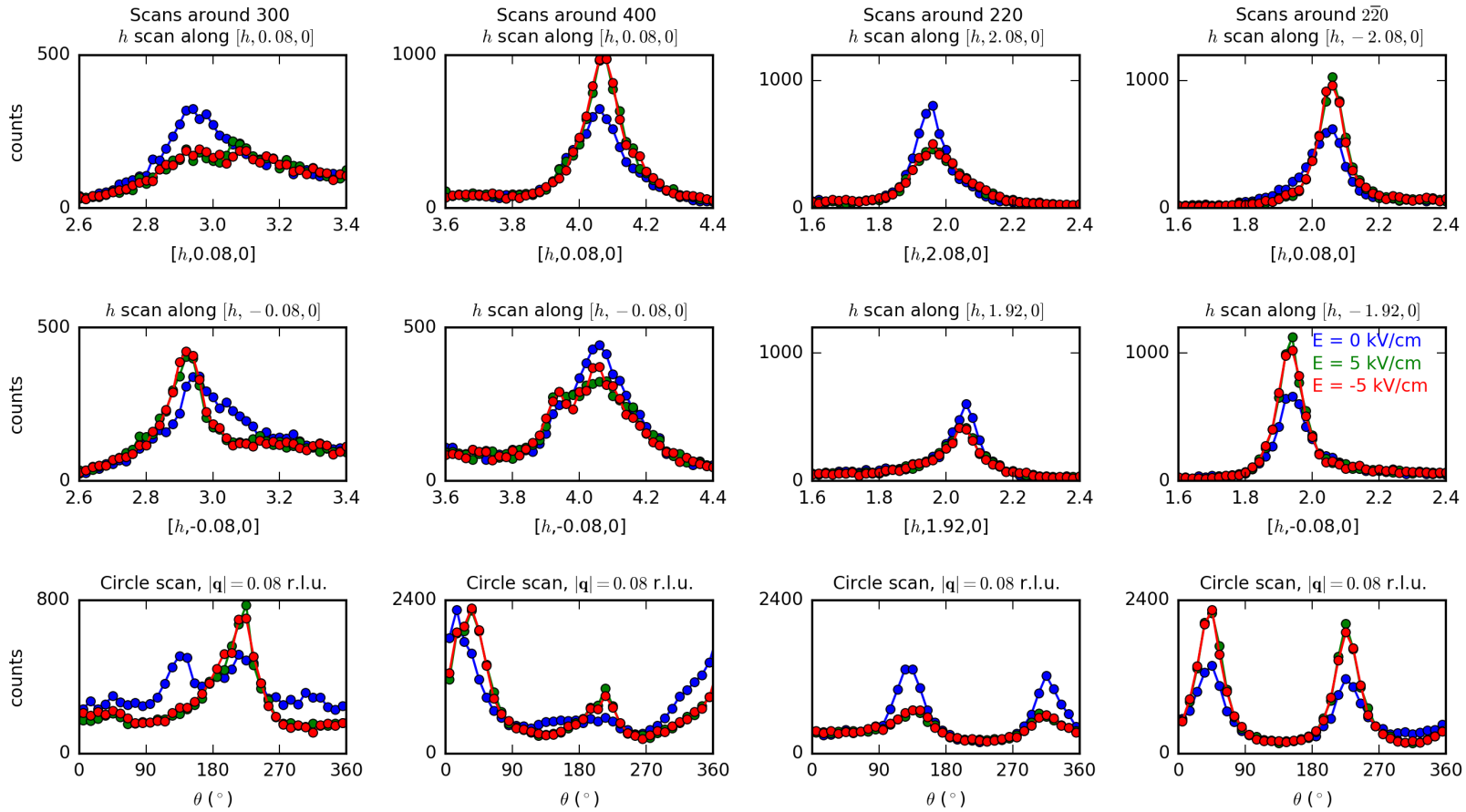

Figure 4.6: *C1* diffuse scattering is affected by an electric field applied in the [110] direction. For each panel, the field applied for each scan is shown by color: blue for the zero-field scan, green for the +5 kV/cm scan, and red for the -5 kV/cm scan.

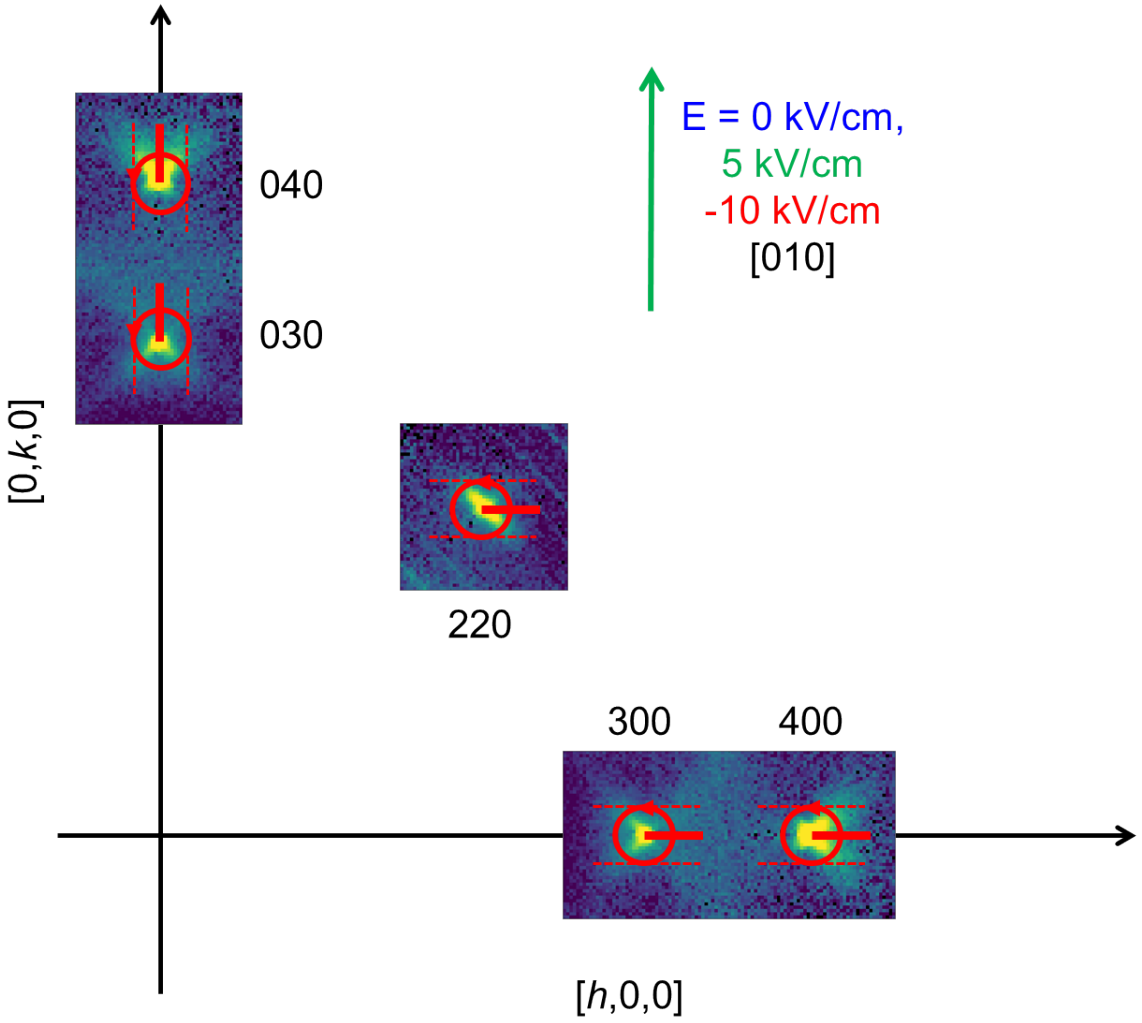

Figure 4.7: Point scans of neutron scattering taken from [010] cut of PMN-30PT using BT-7. Color images of diffuse scattering at each point are from *CORELLI* experiment to show zero-field measurement, dashed red lines show line scans taken, solid red circles show the constant $|\mathbf{q}|$ scan taken around each Bragg peak, and the solid red line define the $\theta = 0$ for each circle scan.

previous study of diffuse scattering from PMN-32PT finding spurious and non-reproducible changes in diffuse scattering under an applied [001] field [87].

4.3 Effect of Electric Fields on Ferroic Diffuse Scattering

Between the x-ray and neutron experiments, three different field configurations were attempted. Neutron scattering experiments makes clear that the asymmetry in *C1* persists under an applied field, further displaying that asymmetry in diffuse neutron scattering is intrinsic to this feature.

C1 can be said to be comprised of six lobes, one for each ⟨110⟩-type direction. The experiments performed here suggest these directions are natural direction for correlations related to ferroic order. Considering the established importance of oxygen atoms in this ordering, it may be inferred that Pb-O distances are directly related to local ferroic structure.

The relative lack of effect in the [010] oriented crystals is also explained if ⟨110⟩ directions are a natural direction for ferroic correlations. The ⟨100⟩ directions can only be expressed as a sum of the ⟨110⟩ directions by using two directions related by reflection across ⟨100⟩ mirror planes (e.g., the [100] direction must be expressed as a combination of [110] and $[1\bar{1}0]$). If correlations in one such ⟨110⟩ direction must be suppressed for a correlations in another ⟨110⟩ direction to be strengthened, a field in which these directions are symmetrically equivalent will not strengthen or weaken correlations in either direction. This supports the concept that polar correlations are not created by an applied field; rather, unpolarized PMN-30PT crystals contain regions of polar correlations across all ⟨110⟩ directions, and an applied field strengthens parallel components and weakens those component which are not parallel. The effect on *C1* diffuse scattering is saturated by 1.5 kV/cm, with higher fields showing little

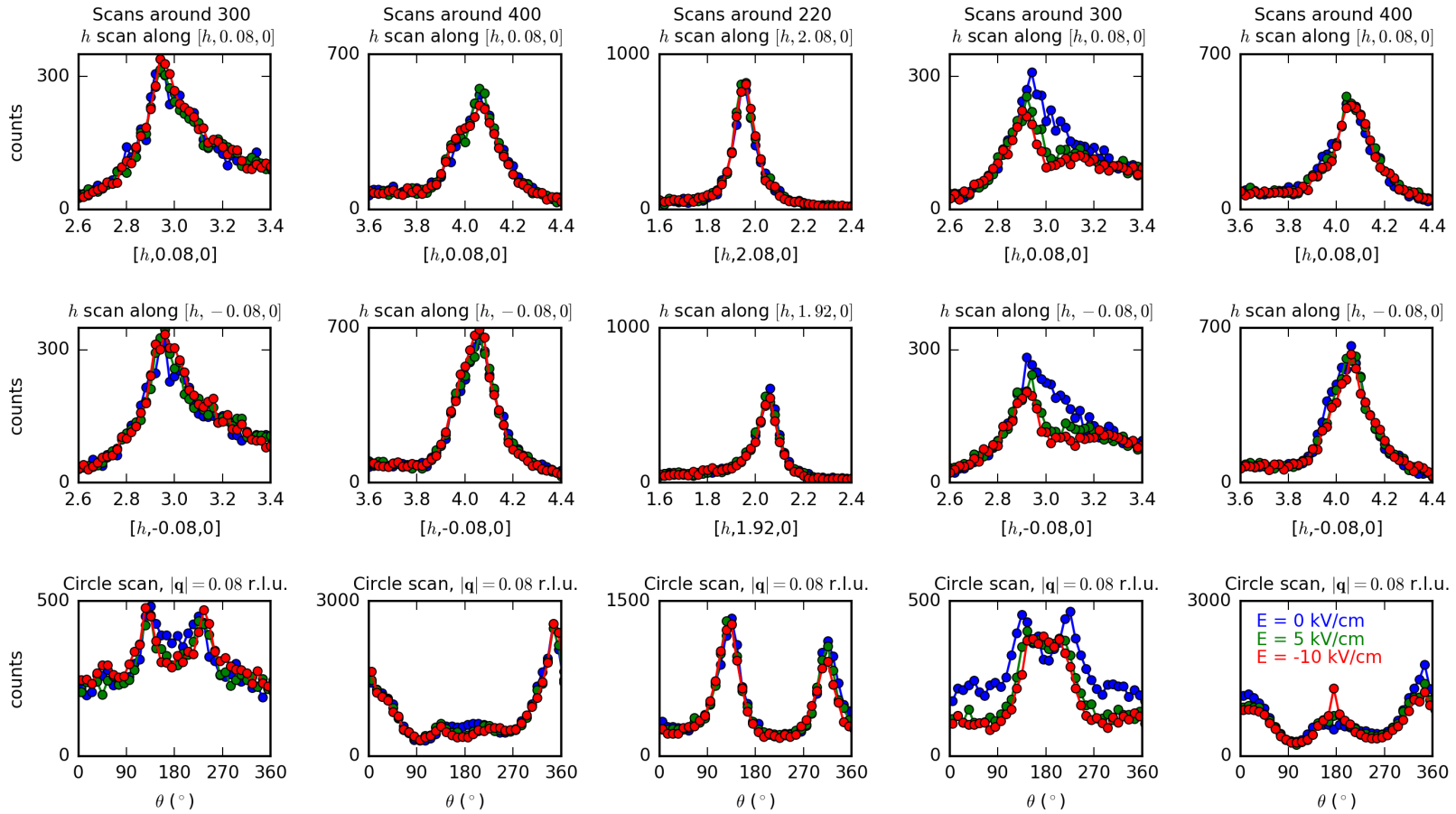

Figure 4.8: *C1* diffuse scattering is not dramatically affected by an electric field applied in the [010] direction. For each panel, the field applied for each scan is shown by color: blue for the zero-field scan, green for the +5 kV/cm scan, and red for the -5 kV/cm scan.

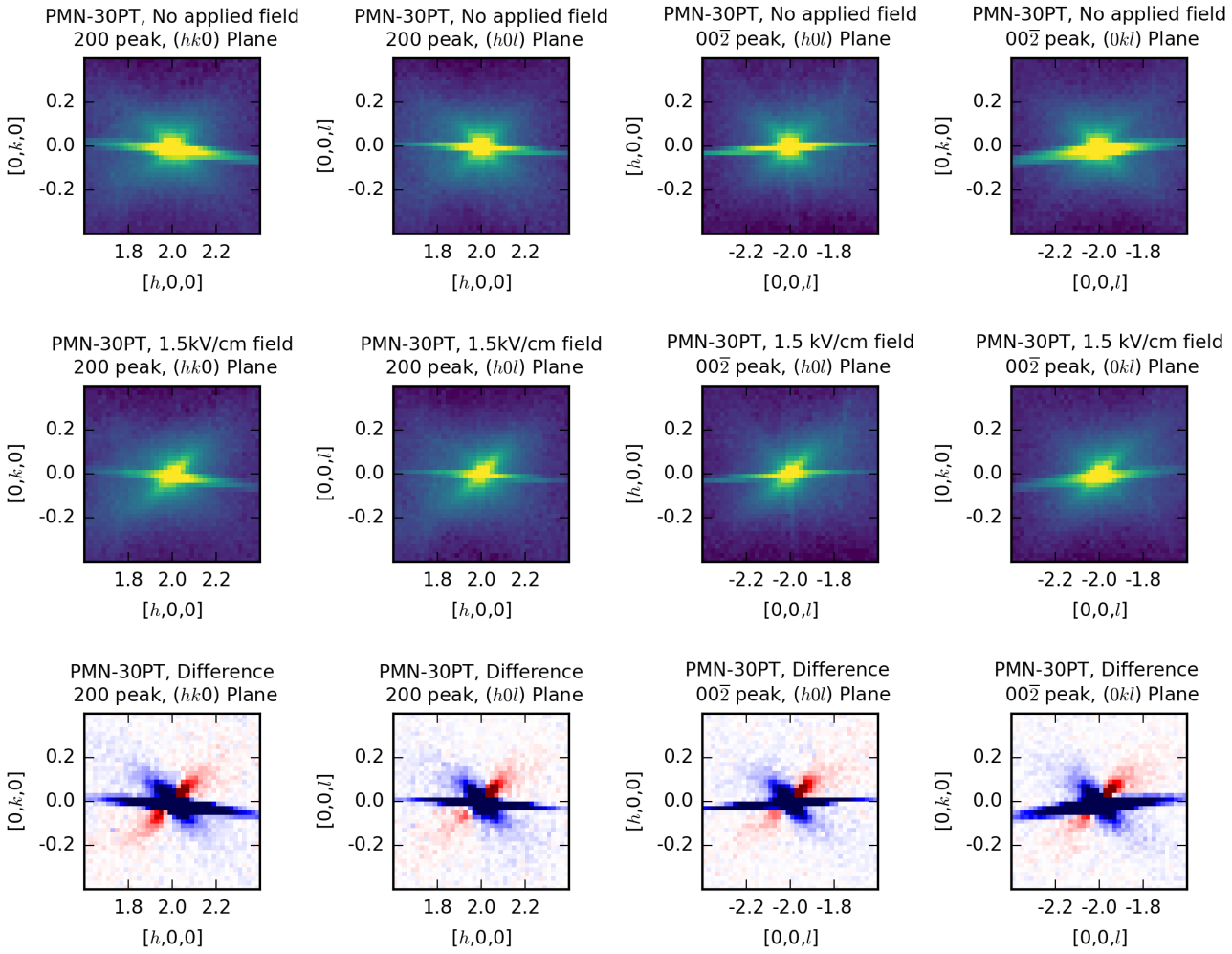

Figure 4.9: *C1* diffuse scattering is redistributed by an electric field of 1.5 kV/cm applied along the [111] direction, viewed near ⟨200⟩ peaks. Components parallel to [110], [101], and [011] are strengthened under the applied field, while the other componenents are weakened. Data has not been symmetrized.

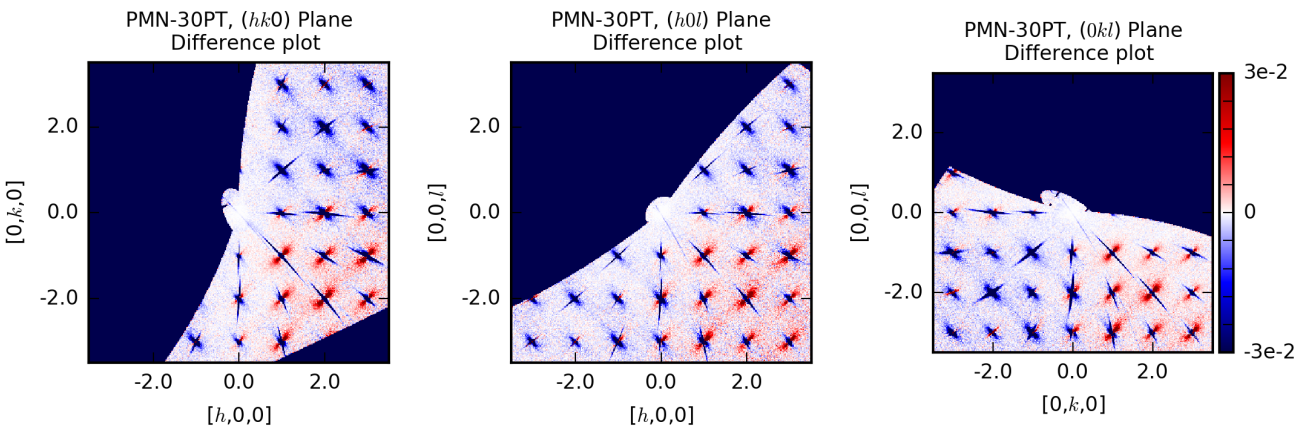

Figure 4.10: *C1* diffuse scattering is redistributed by an electric field of 1.5 kV/cm applied along the [111] direction, viewed in $hk0$-type planes. Components parallel to [110], [101], and [011] are strengthened under the applied field, while the other componenents are weakened. Data have not been symmetrized.

change from this value (Fig. 4.11). This may indicate that the correlations responsible for bulk polarization do not significantly change once a polar state has been established.

4.4 Effect of Electric Fields on Size-Effect Diffuse Scattering

Information on *C4* diffuse scattering was only accessed by the diffuse x-ray scattering measurements. These were sufficient to provide a view at how the local displacements causing the size effect scattering are affected by an applied electric field. Interestingly, *C4* is nearly constant in an applied field, even under a large 6 kV/cm field that is sufficient to significantly change the *C1* intensity. The total intensity of the broad scattering comprising *C4* is only subtly changed; line cuts through *C4* show a clear but small redistribution of scattering intensity.

The systematic change of *C4* intensity is best appreciated with the data symmetrized using six proper and improper rotations of 120° about the [111] direction coincident with the

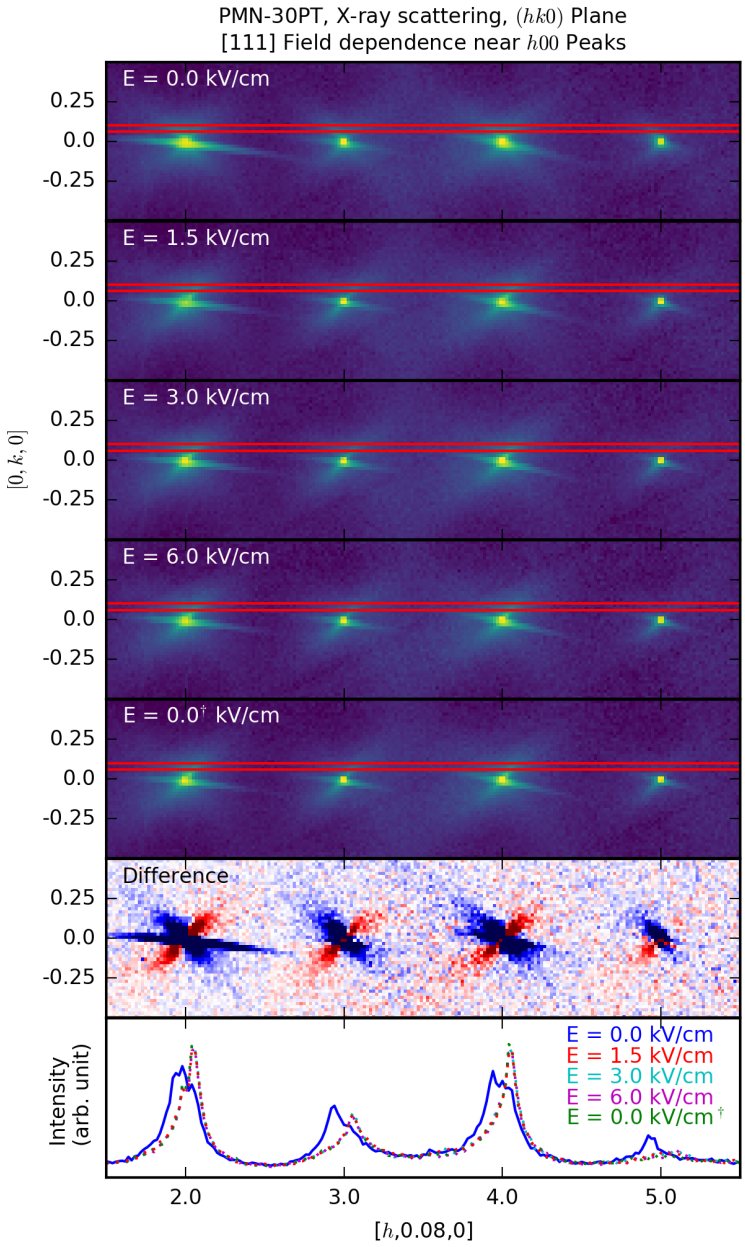

Figure 4.11: *C1* diffuse scattering is redistributed by an electric field of 1.5 kV/cm applied along the [111] direction. The lobe parallel to [110] is strengthened under a field, while the lobe parallel to $[\bar{1}10]$ is weakened. The effect is immediately apparent at 1.5 kV/cm; increasing the field to 6 kV/cm produced no further change. The difference plot shows intensities with E=0.0 kV/cm subtracted from intensities measured with E=1.5 kV/cm. Returning the field to 0 kV/cm (as indicated by the green 0 kV/cm† scan in the legend) does not remove the effect, indicating the polarized state has a decay time significantly greater than the two hour measurement time.

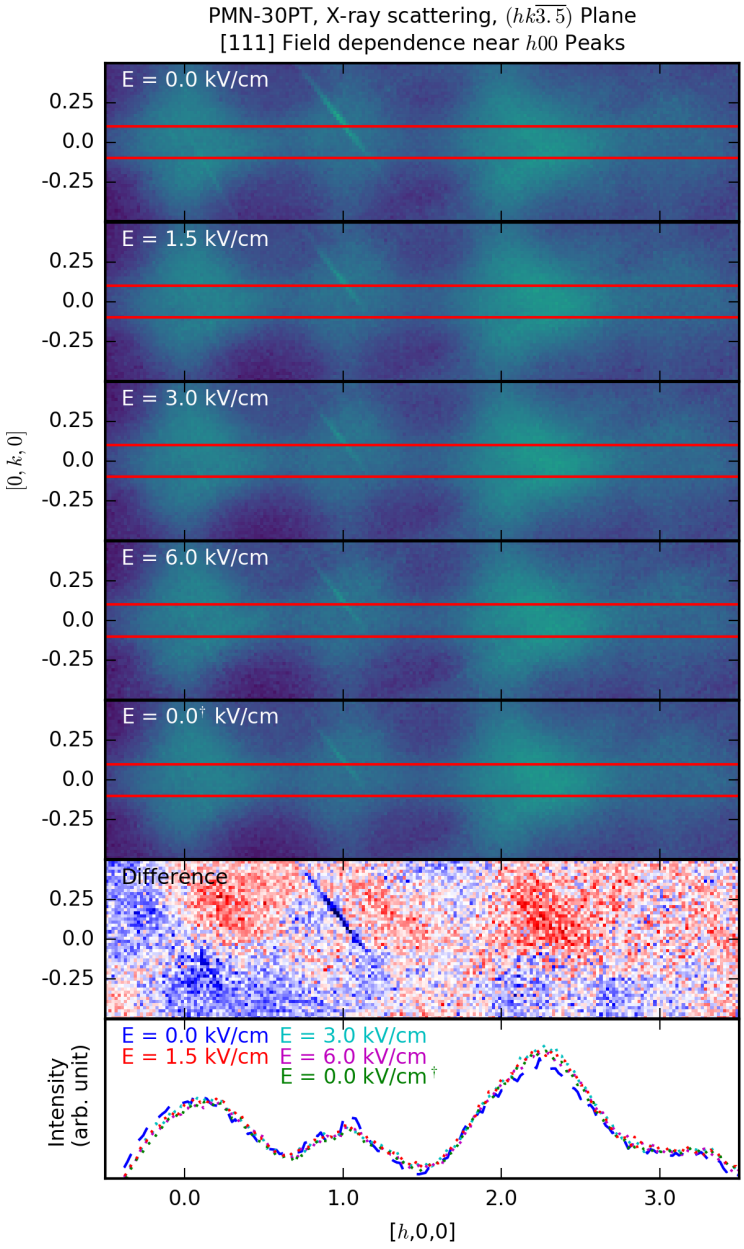

Figure 4.12: This view of *C4* intensity shows little change under an applied field. Similar to the changes in *C1* scattering, a field of 1.5 kV/cm is sufficient to shift *C4* scattering, with increasing electric field producing little further change, and the return of the external field to 0 kV/cm did not return *C4* to its original form.

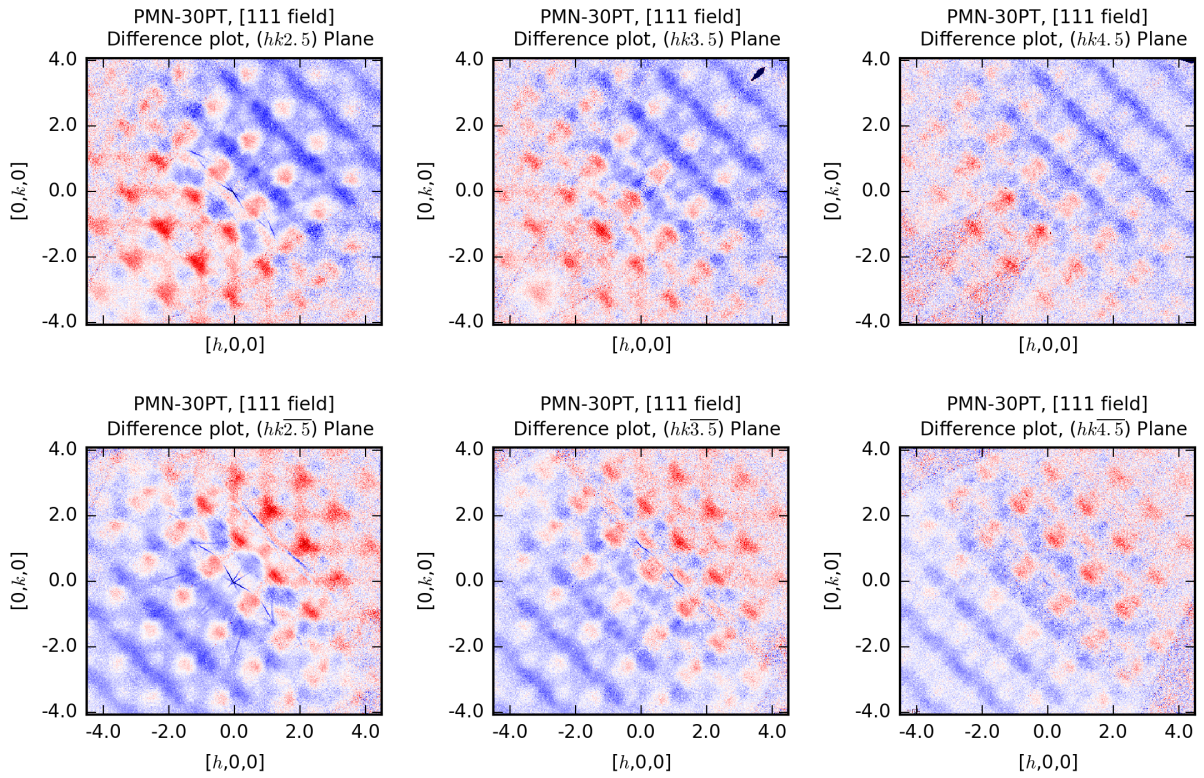

Figure 4.13: Symmetrized scattering of half-planes shows a systematic difference after applying an electric field in the [111] direction. Data have been integrated over a ±0.1 r.l.u. range.

applied field. In this picture, it can be more easily seen that the broad scattering features in this quadrant are suppressed, with these regions gaining in intensity.

The small change in *C4* diffuse scattering under an applied field suggests that the atomic size effect causing *C4* remains significant even when PMN-30PT is in a polarized state, indicating strongly local and electric fields within the material are not overwhelmed even in the polarized state.

CHAPTER 5

DIFFUSE SCATTERING FROM PZT

With a better understanding of how diffuse scattering reveals short-range order and local correlations in PMN-xPT, it is worth considering what similar studies could reveal about related systems. One such related system is $PbZr_{1-x}Ti_xO_3$, commonly referred to as PZT.

PZT is another lead-based perovskite oxide with a morphotropic phase boundary (near $x = 0.5$ for PZT) (Fig. 5.1) where electromechanical coupling is greatly enhanced [88]. However, unlike the relaxor PMN, the end material $PbZrO_3$ is an antiferroelectric [89]. In the solid solution, this provides a different kind of order to compete with the ferroelectric order in $PbTiO_3$. As established in other work [90], the phase diagram for PZT displays a large range of behaviors even within the Ti-poor region. However, the overall picture of a Ti-poor region with behavior more similar to that of $PbZrO_3$ and a Ti-rich region with behavior more similar to $PbTiO_3$ separated by an MPB with greatly enhanced piezoelectric coupling is analogous to that of PMN-xPT, and diffuse scattering from morphotropic PZT provides a different perspective on the same forms of local order seen in PMN-xPT. Experiments for this work were limited to a single composition, $PbZr_{0.54}Ti_{0.46}O_3$, near the MPB.

5.1 Diffuse Neutron Scattering from $PbZr_{0.54}Ti_{0.46}O_3$

Diffuse scattering from a single crystal of $PbZr_{0.54}Ti_{0.46}O_3$ of mass =0.06 g was measured using *Corelli* following initial diffuse scattering measurements of PMN-30PT. The crystal was mounted using superglue and a boron nitride shield, and measurements were taken at 6

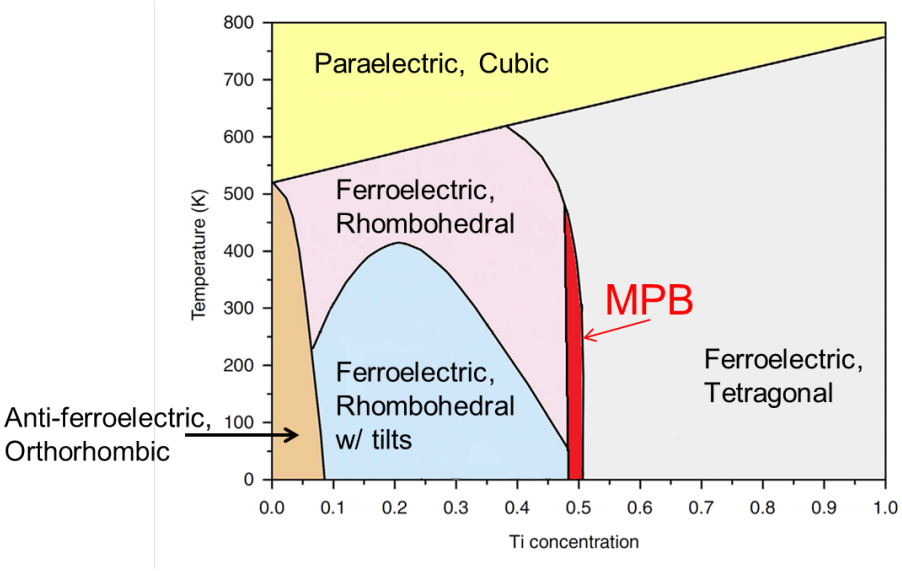

Figure 5.1: Phase diagram of PZT, adapted from [90]. Adapted by permission from Nature, ©2014.

K and 300 K. An area of coverage similar to that from the various PMN-xPT was obtained, although the small crystal size reduced the overall signal strength considerably.

Neutron scattering from $PbZr_{0.54}Ti_{0.46}O_3$ is shown from representative scattering planes $l = 0$, $l = 1$, $h = 2.5$, and $h = 3.5$ measured at 6 K (Fig. 5.2) and 300 K (Fig. 5.3). A small crystallite closely aligned with the main phase is apparent but shouldn't have much effect on the diffuse scattering; it is possible that this is a result of low-temperature distortion from the high-temperature cubic phase, similar to the peak broadening seen in PMN-40PT and PMN-50PT. While the signal from this compsition of PZT is obviously weaker than that from the PMN-xPT systems studied, diffuse scattering like *C1* can be observed around Bragg peaks. This scattering is again stronger at low temperature than it is at higher temperature. Broad scattering like *C4* can also be observed, although the octahedron-like shapes now appear "hollow," with little diffuse intensity around the X point itself, and temperature again has a limited effect on this feature. There are also sharp peaks at R points visible at 6 K, but these peaks are not apparent at 300 K; this finding is consistent with [91].

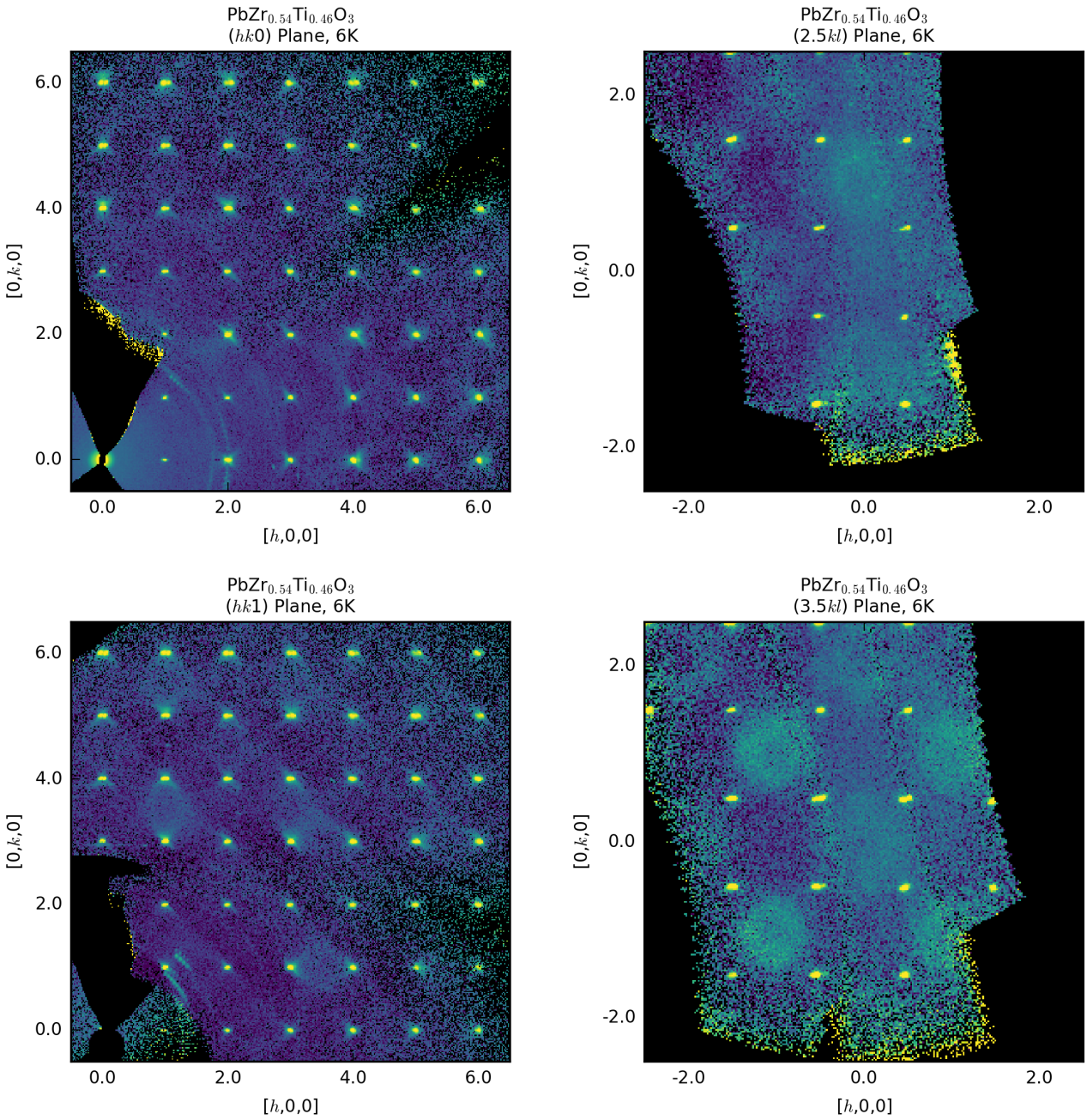

Figure 5.2: Diffuse scattering from $PbZr_{0.54}Ti_{0.46}O_3$ at 6 K, shown in the $l = 0$, $l = 1$, $h = 2.5$, and $h = 3.5$ planes.

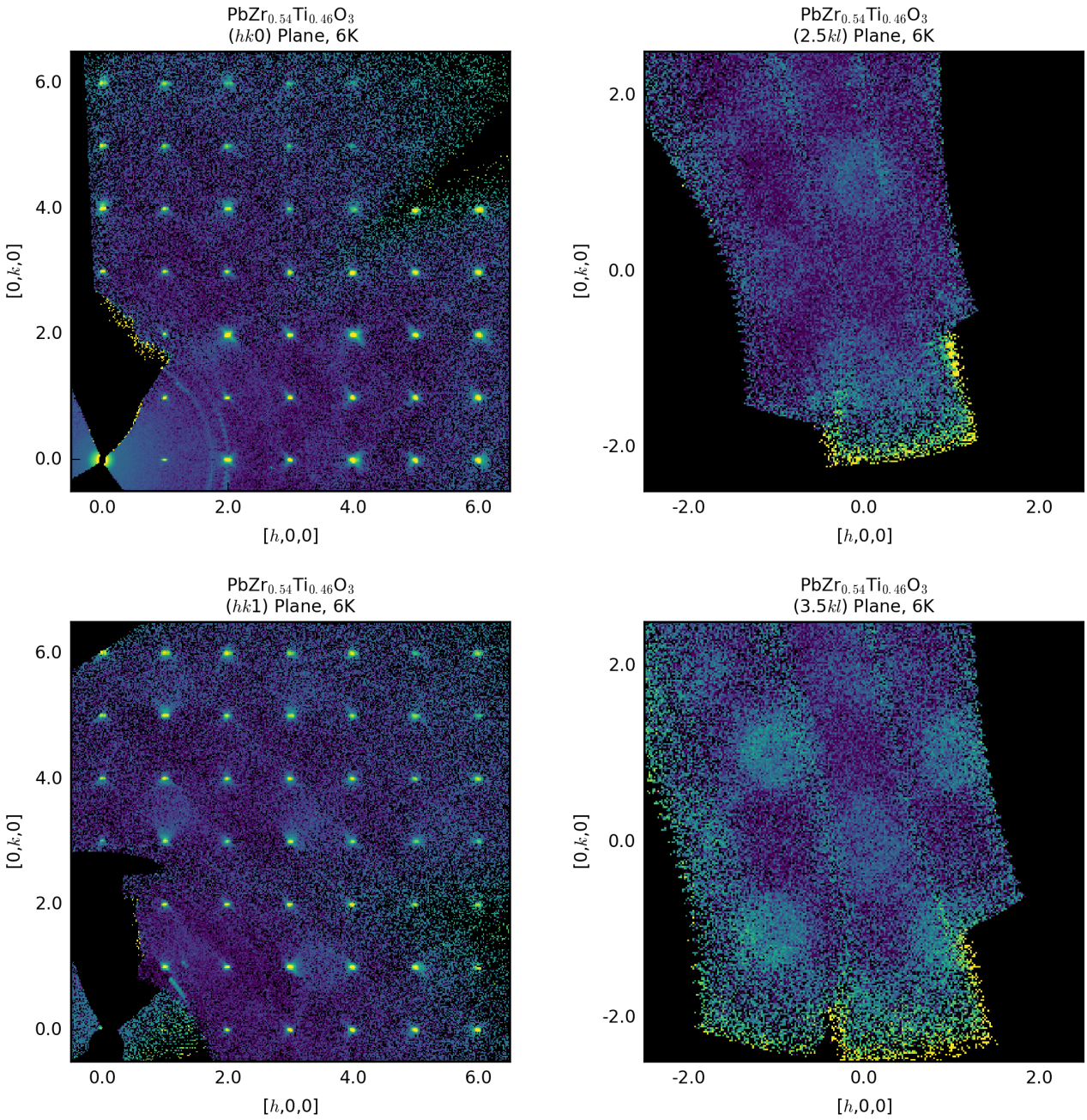

Figure 5.3: Diffuse scattering from $PbZr_{0.54}Ti_{0.46}O_3$ at 300 K, shown in the $l = 0$, $l = 1$, $h = 2.5$, and $h = 3.5$ planes.

5.2 Diffuse X-ray Scattering from $PbZr_{0.54}Ti_{0.46}O_3$

A small piece was removed from the larger crystal studied for diffuse neutron scattering. This small piece was etched in hot HCl to ensure a clean surface and then used for diffuse x-ray scattering experiments at beamline A2 at CHESS. Temperatures were limited to between 100 K (Fig. 5.4) and 400 K (Fig. 5.5), below the transition temperature of 550 K; as such, there is no comparison between the high-temperature paraelectric phase and the low-temperature phases. Measurements were also taken at 200 K and 300 K. The refinement procedure used to generate a mapping between detector images and oriented hkl space found that the pseudocubic lattice parameter used to fit the system actually decreased with increasing temperature (Table 5.1). This observation of negative thermal expansion is consistent with [92].

Table 5.1: $PbZr_{0.54}Ti_{0.46}O_3$ lattice parameter extracted from x-ray scattering peaks fit to a cubic unit cell.

Temperature (K)	a (Å)
100	4.0852
200	4.0843
300	4.0830
400	4.0815

The large flux of synchrotron x-rays provides a considerably cleaner signal and clearer features than are seen in the neutron scattering measurements. *C1*-like scattering is now quite apparent around Bragg peaks, and the differences between the *C4* scattering in PMN-xPT and its analog here can be easily seen, along with subtle changes between 100 K and 400 K. The sharp R point peaks are again visible at the lowest temperature, now 100 K, but not visible at the highest temperature of 400 K.

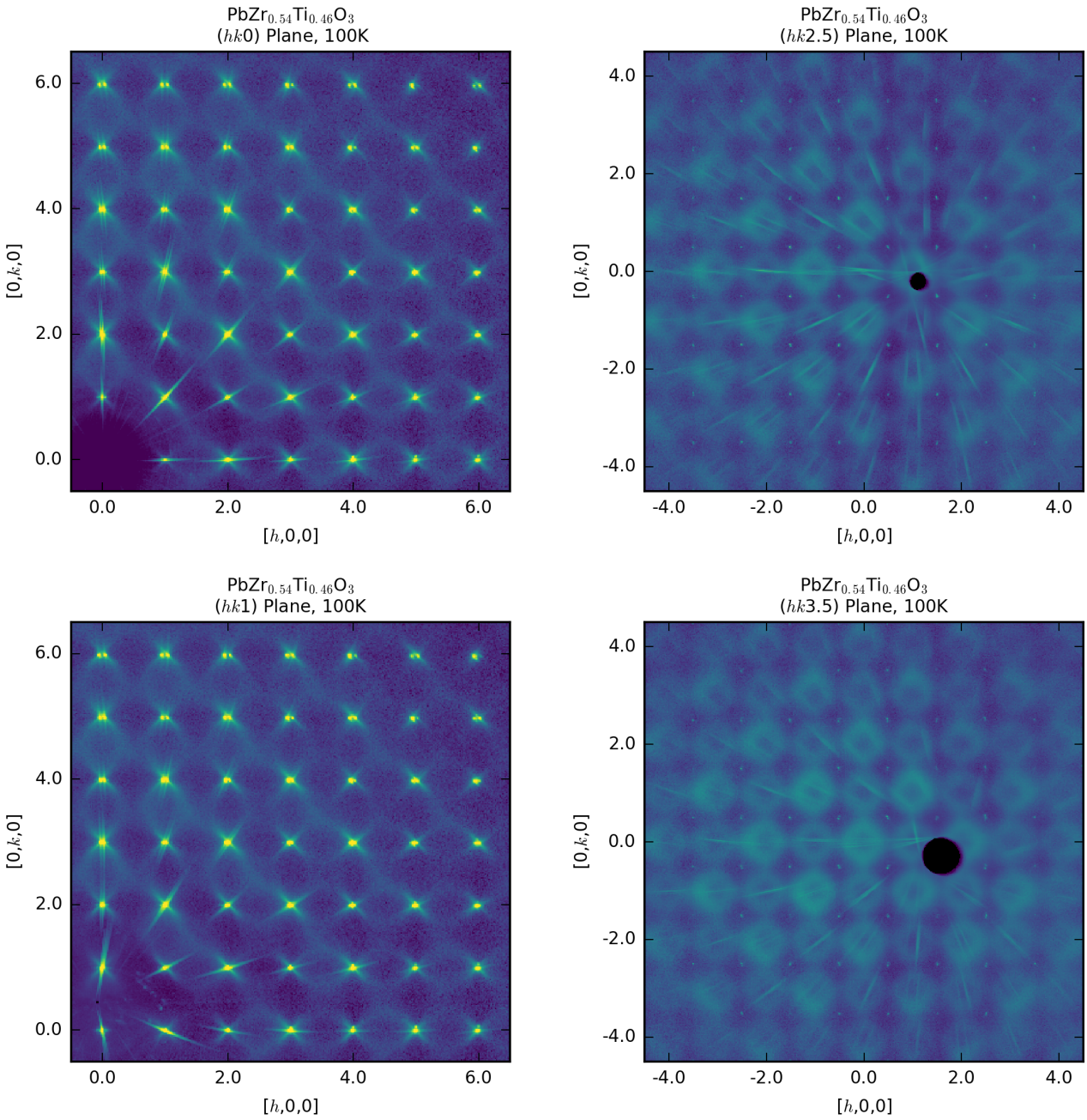

Figure 5.4: Diffuse x-ray scattering from $PbZr_{0.54}Ti_{0.46}O_3$ at 100 K, shown in the $l = 0$, $l = 1$, $l = 2.5$, and $l = 3.5$ planes.

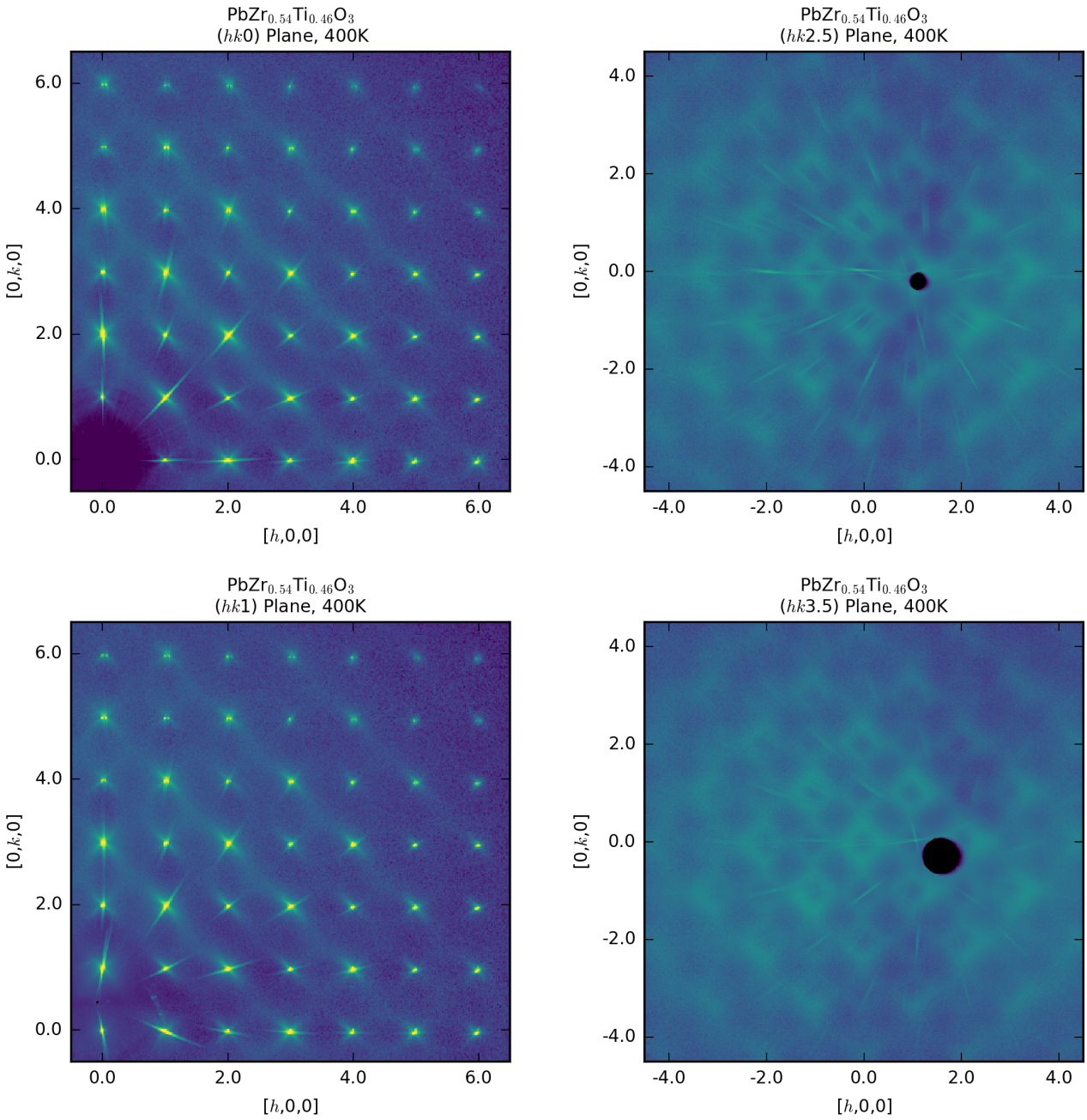

Figure 5.5: Diffuse x-ray scattering from $PbZr_{0.54}Ti_{0.46}O_3$ at 400 K, shown in the $l = 0$, $l = 1$, $l = 2.5$, and $l = 3.5$ planes.

5.3 Components of Diffuse Scattering from PZT

With only one composition measured over a limited temperature range, the diffuse scattering from PZT is best understood in comparison to that from PMN-xPT. In accordance with this comparison, the two components of diffuse scattering that dominate in morphotropic PMN-xPT, *C1* and *C4*, are also present in morphotropic PZT. Strong diffuse scattering centered on Bragg peaks with lobes extending along $\langle 110 \rangle$, similar to the *C1* scattering in PMN-xPT, is clearly observed in $PbZr_{0.54}Ti_{0.46}O_3$. While the range of temperatures accessed is insufficient to make this conclusion definitive, it appears that this scattering is strongest at low temperatures and weakens with increasing temperature. Its origin in PZT may be safely conjectured to be similar to that in PMN-xPT, and this work will refer to this scattering as *ferroic* diffuse scattering.

C4 scattering also has its analogue in PZT. The similarity in parity and overall structure again hint at a common origin of an atomic size effect between Pb atoms and the various B-site occupants, and the difference in shape suggests a difference in local environments for Pb atoms. Because the Zr and Ti atoms each have a valence of 4+ in this material, the presence of a size effect here indicates that a difference in valence is not necessary to generate this kind of size effect.

In addition to these two features, a third feature appears in $PbZr_{0.54}Ti_{0.46}O_3$. This feature consists of sharp superlattice peaks at R points in the Brillouin zone. These peaks are quite sharp compared to those comprising *C3* in PMN, and display a completely different kind of temperature dependence. The origin of these peaks is an octahedral tilt system that appears at low temperatures, doubling the unit cell. Curiously, this tilt system does not have much effect on the other two forms of diffuse scattering present in these measurements, and no

temperature-independent component exists, suggesting that chemical ordering is not a factor in $PbZr_{0.54}Ti_{0.46}O_3$.

5.3.1 Ferroic Diffuse Scattering from PZT

The comparison between *C1* scattering in PMN-30PT and ferroic diffuse scattering in PZT is easily made, as the patterns have an immediate qualitative similarity (Fig. 5.6). The diffuse scattering surrounding Bragg peaks extends in $\langle 110 \rangle$ directions.. A common origin of this diffuse scattering seems likely, particularly given the chemical and structural similarities between PMN-xPT and PZT. $PbZr_{0.54}Ti_{0.46}O_3$ is near the MPB for the PZT system, and the similarity between the ferroic scattering from $PbZr_{0.54}Ti_{0.46}O_3$ and the *C1* scattering from PMN-30PT, itself close to the MPB for its system, may imply that the association between *C1* and d_{33} in PMN-xPT extends to PZT and other similar systems.

Of particular interest is the presence of the same asymmetry between low-$|\mathbf{Q}|$ and high-$|\mathbf{Q}|$ diffuse lobes, particularly evident in neutron scattering (Fig. 5.7). Similar to *C1* scattering in PMN-xPT, ferroic scattering from PZT is stronger on the high-$|\mathbf{Q}|$ side near Bragg peaks with all-even or all-odd Miller indices and stronger on the low-$|\mathbf{Q}|$ side near Bragg peaks with mixed even and odd Miller indices. While there may be differences betweeen the two systems in the mechanism that generates this diffuse scattering, oxygen atoms must play a similar role in each.

With all temperatures measured below T_C, it is perhaps unsurprising that little change is seen in the ferroic diffuse scattering from $PbZr_{0.54}Ti_{0.46}O_3$ over the temperatures investigated (temperature dependence of x-ray scattering shown in Fig. 5.8). This feature may perhaps become slightly less sharp as temperature increases, but the scattering remains qualitatively similar between 6 K and 400 K. As with PMN-xPT, this is consistent with the ferroic diffuse

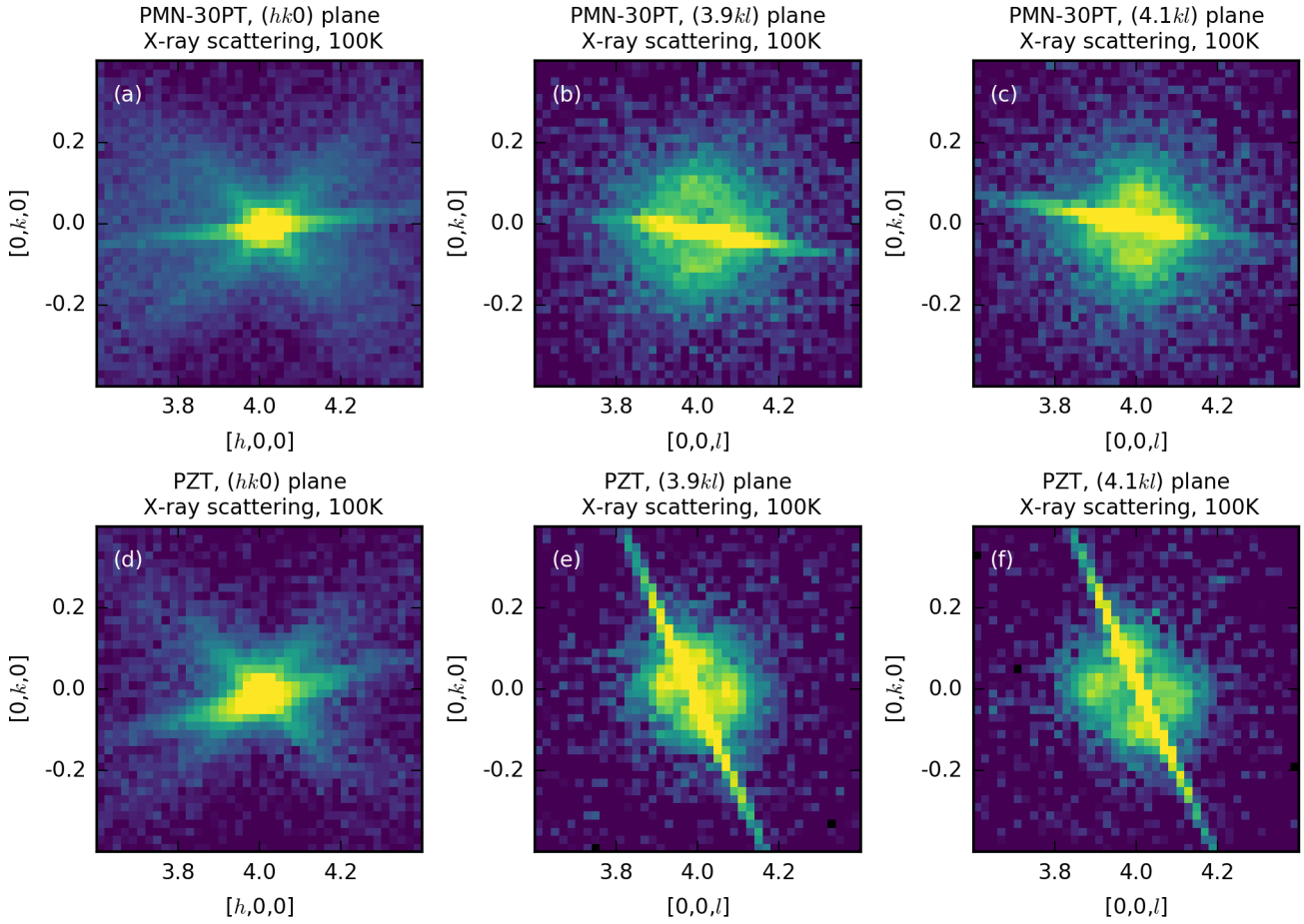

Figure 5.6: Diffuse x-ray scattering in the 400 Brillouin zone. (a-c) From PMN-30PT, $(h, k, 0)$, $(3.9, k, l)$ and $(4.1, k, l)$ planes measured at 100 K with x-rays. (d-f) From $PbZr_{0.54}Ti_{0.46}O_3$, $(h, k, 0)$, $(3.9, k, l)$ and $(4.1, k, l)$ planes measured at 100 K with x-rays. The $(3.9, k, l)$ and $(4.1, k, l)$ planes show the lobes of scattering in the planes perpendicular to the $(h, k, 0)$ plane as marked in panels (a) and (d). Data have been integrated in the normal direction over a range of 0.02 rlu. Intensity scales are logarithmic.

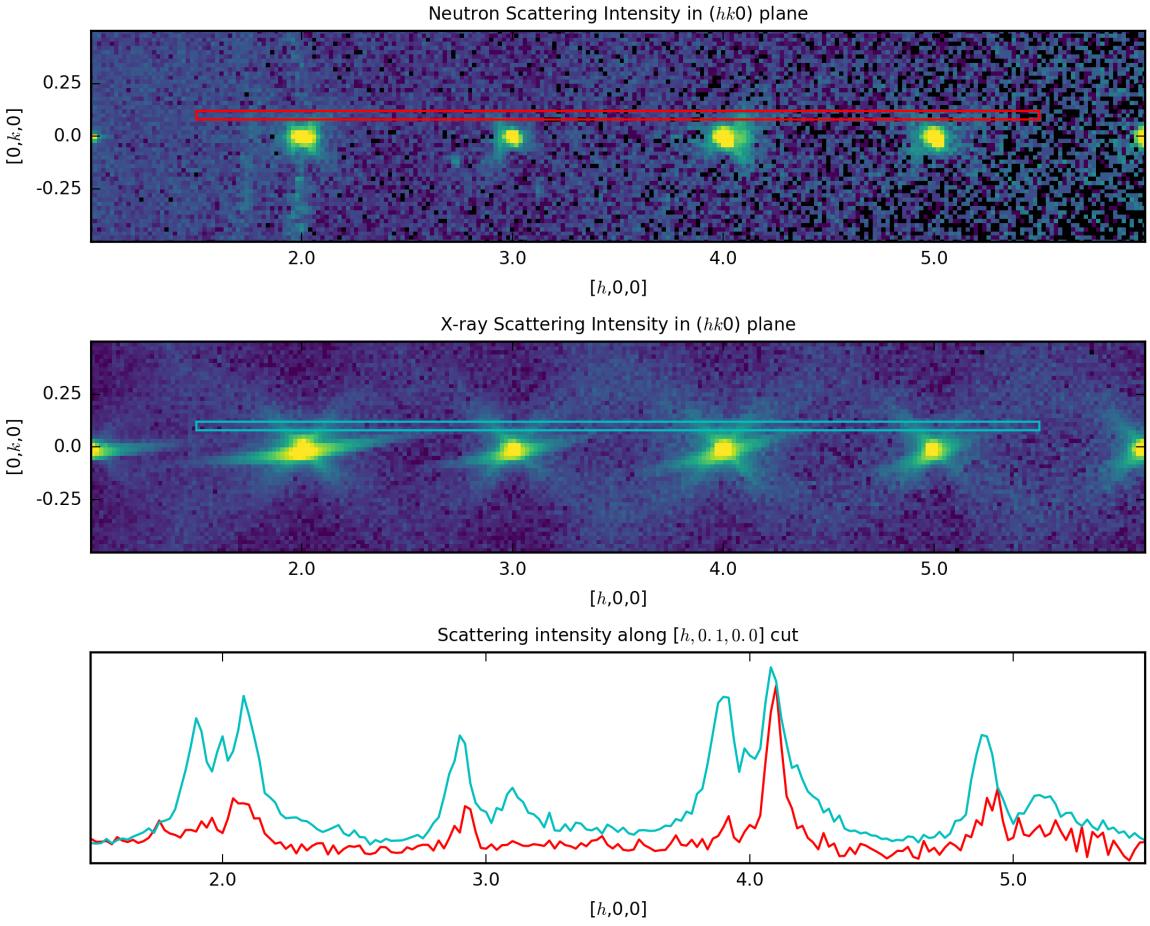

Figure 5.7: Diffuse x-ray and neutron scattering near $h00$ zones. The asymmetry between low-$|\mathbf{Q}|$ and high-$|\mathbf{Q}|$ diffuse scattering is significantly larger for neutron scattering than it is for x-ray scattering, indicating a role for correlated oxygen displacements.

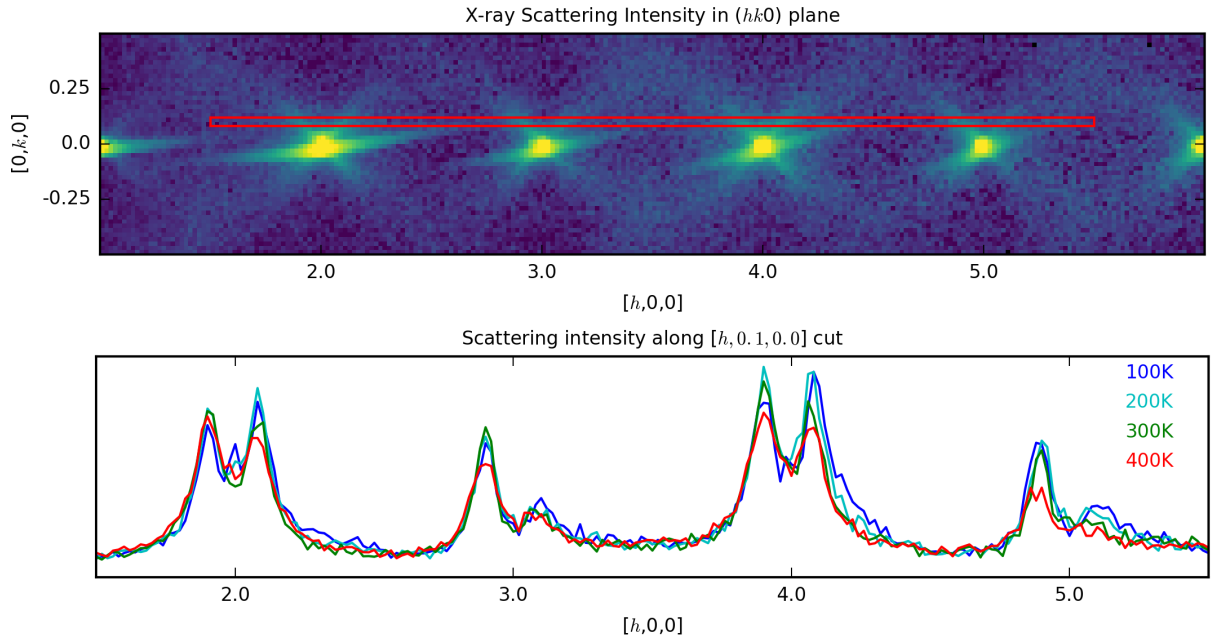

Figure 5.8: Temperature dependence of diffuse x-ray scattering near $h00$ zones. This type of scattering weakens with increasing temperature, but is still present at 400 K; this is consistent with a link between this scattering and ferroic behavior, as 400 K is below $T_C \approx 630K$ for this material.

scattering being correlated with the ferroelectric behavior of PZT; it may be expected that above T_C, this scattering will diminish more significantly.

5.3.2 Size-Effect Scattering from PZT

Perhaps the most obvious diffuse feature in x-ray scattering from $PbZr_{0.54}Ti_{0.46}O_3$, the broad diffuse scattering between the Bragg peaks has many of the same characteristics as the *C4* scattering from PMN-xPT. The outline of the shape seems almost identical, as does the three-dimensional checkerboard pattern of strong and weak features in reciprocal space.

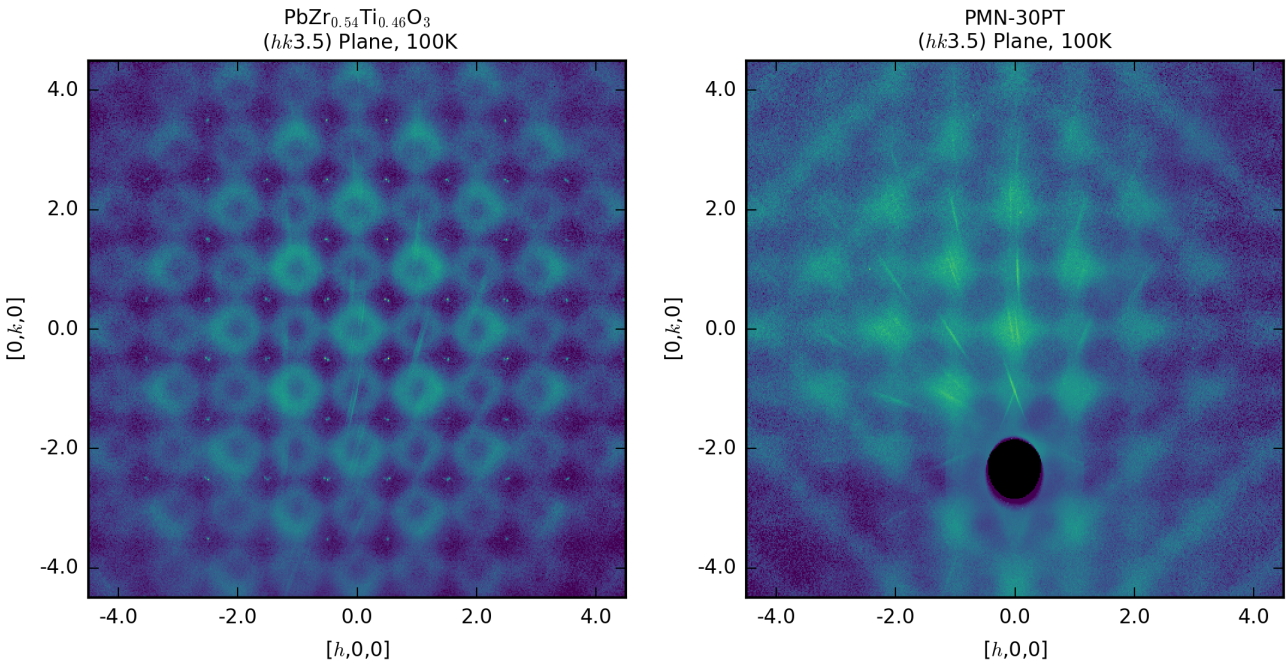

Figure 5.9: Diffuse x-ray scattering in the $(hk3.5)$ plane measured at 100 K, $PbZr_{0.54}Ti_{0.46}O_3$ on the left and PMN-30PT on the right.

These similarities clearly indicate a similar origin of a size effect between Pb atoms and possbile B-site occupants, with Pb atoms tending to be farther away from the heavier Zr atoms and closer to the lighter Ti atoms.

However, as seen in Fig. 5.9, the broad octahedra of size-effect scattering in PMN-30PT are not reproduced in $PbZr_{0.54}Ti_{0.46}O_3$, where the octahedra are 'hollow,' with little diffuse intensity at the X point itself. This clearly indicates a significant difference in the manifestation of the size effect between the two systems.

Calculated scattering from a model produced via Monte Carlo simulation is able to reproduce something like this difference using a model like the one used for PMN-xPT (Fig. 5.10). Slightly increasing the difference between the possible B site occupants to 1.03 times average for Pb to Zr and 0.97 times average for Pb to Ti diminishes intensity at the center of the octahedral features. However, this does not quite capture the complete lack of diffuse

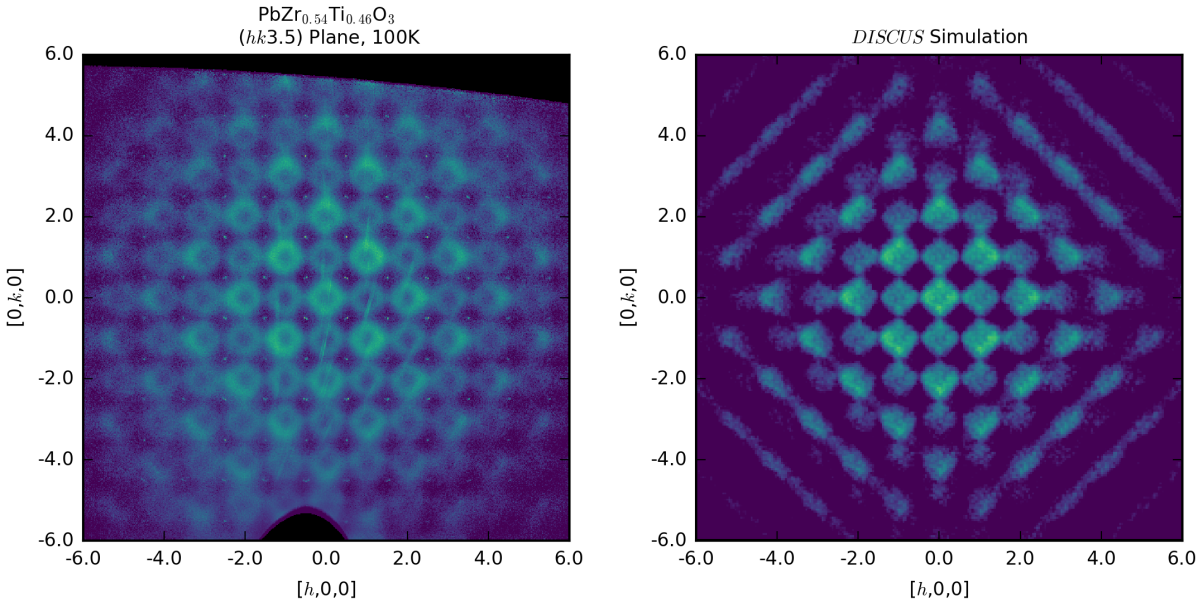

Figure 5.10: Diffuse x-ray scattering in the $(hk3.5)$ plane measured at 100 K, $PbZr_{0.54}Ti_{0.46}O_3$ on the left, with calculated scattering from a crystal simulated in *DISCUS* on the right.

intensity surrounding the center of the feature, and attempting to place a more extreme disparity in the Monte Carlo process tends to destabilize the simulated crystal entirely. It is possible that a more careful set of parameters may better reproduce the observed scattering; for now, the qualitative difference in size effect scattering between PMN-xPT and PZT may be said to result from PZT having larger and more consistent displacement correlations between Pb atoms and B site occupants.

The nature of Monte Carlo simulations makes it difficult to assess which displacement correlations in the simulated crystal are important to generating any specific feature or if that correlation uniquely does so. However, from looking at the distances generated in the simulated crystal, it is clear that displacements only need to differ from the average over a few unit cells to reproduce the observed pattern of scattering. The most extreme distortions

bewteen Pb atoms and B site atoms are along $\langle 111 \rangle$, with other interatomic vectors featuring little to no distortion at all. This suggests that this size effect can be quite short-range while still reproducing the observed scattering. While the only potential used in the Monte Carlo system was between Pb atoms and B site atoms, displacements between B site atom pairs were also distorted within the distance of a few unit cells.

Table 5.2: Distances between various atomic pairs in the simulated $PbZr_{0.54}Ti_{0.46}O_3$ crystal used to generate Fig. 5.10. The distance d^{ij}_{lmn} represents the average distance between an ij pair of atoms separated by vector lmn in an simulated crystal; D_{lmn} represents the undistorted distance.

d^{ij}_{lmn}	d^{ij}_{lmn}/D_{lmn}	d^{ij}_{lmn}	$d^{ij}_{lmn}/\ D_{lmn}$
$d^{\text{Pb-Ti}}_{\frac{1}{2}\langle 111\rangle}$	0.974	$d^{\text{Pb-Zr}}_{\frac{1}{2}\langle 111\rangle}$	1.032
$d^{\text{Pb-Ti}}_{\frac{1}{2}\langle 311\rangle}$	1.003	$d^{\text{Pb-Zr}}_{\frac{1}{2}\langle 311\rangle}$	1.003
$d^{\text{Pb-Ti}}_{\frac{1}{2}\langle 331\rangle}$	1.001	$d^{\text{Pb-Zr}}_{\frac{1}{2}\langle 331\rangle}$	1.004
$d^{\text{Pb-Ti}}_{\frac{1}{2}\langle 333\rangle}$	0.998	$d^{\text{Pb-Zr}}_{\frac{1}{2}\langle 333\rangle}$	1.002
$d^{\text{Ti-Ti}}_{\langle 100\rangle}$	1.017	$d^{\text{Zr-Zr}}_{\langle 100\rangle}$	0.987
$d^{\text{Zr-Ti}}_{\langle 100\rangle}$	1.004	$d^{\text{Zr-Ti}}_{\langle 110\rangle}$	1.002
$d^{\text{Ti-Ti}}_{\langle 110\rangle}$	0.990	$d^{\text{Zr-Zr}}_{\langle 110\rangle}$	1.009
$d^{\text{Ti-Ti}}_{\langle 111\rangle}$	0.987	$d^{\text{Zr-Zr}}_{\langle 111\rangle}$	1.015
$d^{\text{Zr-Ti}}_{\langle 111\rangle}$	0.998	$d^{\text{Zr-Ti}}_{\langle 200\rangle}$	1.001
$d^{\text{Ti-Ti}}_{\langle 200\rangle}$	1.002	$d^{\text{Zr-Zr}}_{\langle 200\rangle}$	0.999

As with PMN-xPT, only subtle changes are seen in diffuse scattering with increasing temperature. This may hint at a small reduction in the length scales over which the size effect is relevant as temperature is increased. It is also worth noting that the intensity in the center of the octahedra increases relative to that at the edges as temperature increase. The greater intricacy of the size effect scattering does invite speculation as how this feature evolves above T_C and T_B. One would expect that this diffuse scattering might be suppressed entirely at a sufficiently high temperature, but might there be an intermediate temperature

where the size effect scattering from $PbZr_{0.54}Ti_{0.46}O_3$ closely resembles that of PMN-xPT? The answer may help shed light on how important the size effect is to the behavior of the system.

5.3.3 R-point Superlattice Peaks in PZT

Many perovskites have been shown to have octahedral tilt systems, forming larger supercells [93, 94]. Such tilting is clearly present in $PbZr_{0.54}Ti_{0.46}O_3$. As discussed in [90], morphotropic PZT shows an $a^-a^-a^-$ type tilt system, effectively doubling the cubic unit cell in all three dimensions and leading to sharp superlattice peaks at R points. This is confirmed in both the x-ray and neutron diffuse scattering studies at temperatures below 300 K. A detailed temperaure dependence of these peaks was not obtained in either study, but the temperature steps used for the x-ray study confirm that these peaks are much stronger at 100 K than at 200 K (Fig 5.12). These well-defined peaks are strongly diminished at 200 K and disappear by 300 K, consistent with the onset of the tilt system. It is noteworthy that the diffuse scattering components *C1* and *C4* are not appreciably changed around this temperature. While the sharp peaks are strong evidence for the octahedral tilt system in PZT, it appears that long-range tilting order has little effect on the other forms of local order in the system.

The lack of R-point scattering at higher temperatures does indicate a lack of chemical ordering of the type indicated by *C3* in PMN, where possible B site occupants tend to alternate. It should be noted that if $\alpha_{100}^{Zr-Ti} > 0$ for PZT (i.e., if like atoms tended to cluster instead of alternate), this would produce diffuse scattering at Bragg positions instead of R points, so the absence of R point scattering cannot rule out this possibility. That said, clustering would likely produce a system that looks more like a superposition of the long-

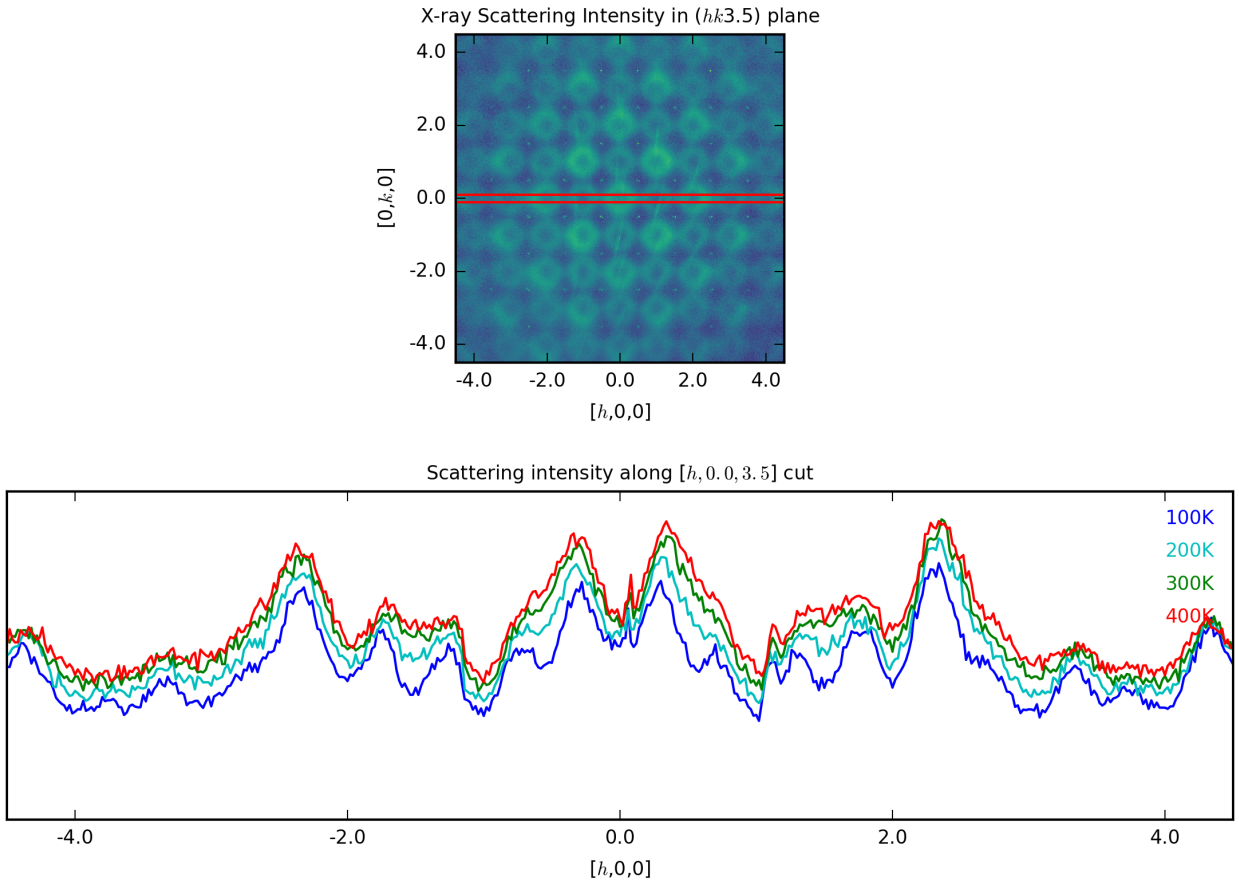

Figure 5.11: Diffuse x-ray scattering from $PbZr_{0.54}Ti_{0.46}O_3$ in the (hk3.5) plane measured at 100 K, with cuts from 100 K, 200 K, 300 K, and 400 K.

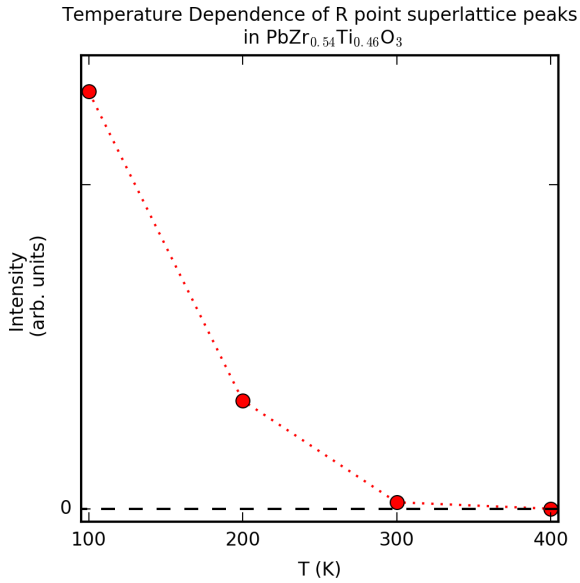

Figure 5.12: Intensity of R point superlattice peaks in $PbZr_{0.54}Ti_{0.46}O_3$ measured with x-rays. Vertical scale is linear.

range ordered antiferroelectric $PbZrO_3$ and ferroelectric $PbTiO_3$ instead of the morphotropic phase diagram actually seen.

CHAPTER 6

CONCLUSIONS AND FUTURE WORK

The local orders of PMN-xPT give rise to four major components of diffuse scattering, each one possessing its own compositional and temperature dependence. Ferroic (i.e. polar) distortions give rise to diffuse scattering centered at $\mathbf{q} = 0$, which is highly temperature- and electric-field dependent, and measurements show that this scattering possesses a rich structure that strongly varies between Brillouin zones and can only be explained by considering both cation and oxygen displacements. Existing models of *C1* need to be reconsidered with this in mind; there is an entire network of atoms in PMN-xPT, and approximating ferroic behavior through Pb^{2+} displacements alone will at best miss the structural contributions from O^{2-} displacements. The zone-dependent shapes of the diffuse scattering identified in this work should serve as a guideline for judging both existing and future models. More generally, this is a clear demonstration of how the reproduction of diffuse scattering shapes in only one or two Brillouin zones is inadequate to judge the validity of a model. *C1* scattering correlates with electromechanical coupling, and this may be understood by the presence of multiple competing ferroic domain states near the MPB. Despite the correlation that has commonly been drawn between this form of diffuse scattering and relaxor physics, the compositional dependence shows that the ferroic diffuse scattering is greatest at the MPB, where the relaxational properties are negligible. On the other hand, antiferroelectric distortions, which give rise to scattering at the zone-boundary M points and are also temperature-dependent, possess a compositional dependence that strongly correlates to frequency-dependent susceptibilities. Regions of short-range antiferroelectric order are likely seeded by chemical short-range ordering, which possesses a very similar compositional dependence. Our work suggests a picture

of relaxors in which competition between local ferroelectric and antiferroelectric correlations leads to relaxational dielectric properties in Pb-based oxides due to frustration. As chemical ordering and antiferroelectric correlations are reduced, relaxational properties dissipate. Charge (Mg^{2+}/Nb^{5+}) ordering occurs locally in PMN, and this ordering diminishes upon increasing Ti^{4+} substitution. Ionic size mismatch leads to broad diffuse components that are only weakly temperature-dependent below T_B, present for all compositions, centered at X points, and have been reproduced in simulations.

An avenue of future work should be to apply the combination of neutron scattering and x-ray diffraction techniques described here with compositional studies in systems beyond PMN-xPT. The preliminary work presented here on a single composition of PZT provides an interesting contrast; this could be filled out in a similar study spanning the phase diagram of PZT. Similar studies on $PbZn_{1/3}Nb_{2/3}O_3$ and $PbSc_{1/2}Nb_{1/2}O_3$ are similarly indicated, as would be studies of lead-free relaxors such as $Na_{1/2}Bi_{1/2}TiO_3$. A rough explanation for the large d_{33} here may be a balance between the strong double-well potential of ferroelectric PTO and the strong local antiferroelectric interactions in PMN; a relatively flat energy landscape with small local minima could provide a large range of energetically different states with significant structural differences within a narrow band of potential energy. Several morphotropic systems share this general picture of ferroelectric behavior mixing with some competing type of polar ordering; it is likely that the competition between different kinds of short-range order is what defines these systems.

Even as this work is produced, methods for collecting diffuse scattering data improve, particulary with x-rays, where a method of adjusting goniometer angles has shown remarkable promise in removing scattering artifacts from Pilatus data. New detectors allow for greater efficiency yet in collecting x-ray data, and techniques will improve as more experiments of this kind are performed. The Compton artifact so obviously marring the x-ray scattering data can be removed by utilizing more highly absorbing x-ray detector materials such as

CdTe, and the offending pixels can be resampled entirely by changing goniometer angles as well as detector positions between scans. Recent detector tests at Sector 6 of the Advanced Photon Source included a scan of PMN, where these techniques provided a superior diffuse scattering dataset (alas, too late for inclusion in this work!).

The diffuse scattering analysis presented here is relatively crude and limited to qualitative models and observations. Quantitative models will be difficult to produce given the complexity of diffuse scattering data, but newer methods of analysis may provide further insights. In particular, new developments in the 3D-ΔPDF method [95, 96] should provide significant information regarding length scales and the exact nature of local distortions, especially given the contrast between neutron scattering and x-ray scattering data. With different components of scattering identified, a 'divide-and-conquer' approach, with each component separated and transformed individually to take advantage of the linearity of the Fourier transform, might be able to isolate the the different kinds of local distortions.

REFERENCES

[1] B. J. Campbell, R. Osborn, D. N. Argyriou, L. Vasiliu-Doloc, J. F. Mitchell, S. K. Sinha, U. Ruett, C. D. Ling, Z. Islam, and J. W. Lynn. Structure of nanoscale polaron correlations in $La_{1.2}Sr_{1.8}Mn_2O_7$. *Phys. Rev. B*, 65:014427, Dec 2001.

[2] S-H Lee, Collin Broholm, William Ratcliff, G Gasparovic, Q Huang, T H Kim, and S-W Cheong. Emergent excitations in a geometrically frustrated magnet. *Nature*, 418:856–8, 09 2002.

[3] M T Hutchings, K Clausen, M H Dickens, W Hayes, J K Kjems, P G Schnabel, and C Smith. Investigation of thermally induced anion disorder in fluorites using neutron scattering techniques. *Journal of Physics C: Solid State Physics*, 17(22):3903, 1984.

[4] Roger Cowley, S N. Gvasaliya, Sergey Lushnikov, B Roessli, and Gelu Rotaru. Relaxing with relaxors: A review of relaxor ferroelectrics. 60:229–327, 2011.

[5] M. A. Krivoglaz. *Diffuse scattering of x-rays and neutrons by fluctuations*. Berlin ; New York : Springer-Verlag, 1996.

[6] P. H. Dederichs. Theory of diffuse scattering from crystals with point defects. *Journal of Applied Crystallography*, 8(2):142, 1975.

[7] Malcolm E. Lines and A. M. Glass. *Principles and applications of ferroelectrics and related materials*. Oxford Eng. : Clarendon Press, 1977.

[8] Gerald Burns and F.H. Dacol. Glassy polarization behavior in ferroelectric compounds $Pb(Mg_{1/3}Nb_{2/3})O_3$ and $Pb(Zn_{1/3}Nb_{2/3})O_3$. *Solid State Communications*, 48(10):853 – 856, 1983.

[9] T. R. Welberry. *Diffuse X-ray Scattering and Models of Disorder*. Oxford University Press, 2004.

[10] B. E. Warren. *X-Ray Diffraction*. Dover Publications, 1990.

[11] Albert Furrer, Joël Mesot, and Thierry Strässle. *Neutron Scattering in Condensed Matter Physics*. World Scientific Press, 2009.

[12] B. Fultz and J. Howe. *Transmission Electron Microscopy and Diffractrometry of Materials*. Springer Science & Business Media, 2013.

[13] G. Harburn, C. A. Taylor, and T. R. Welberry. *Atlas of Optical Transforms*. G. Bell & Sons Ltd., 1975.

[14] B. Borie and C. J. Sparks. The interpretation of intensity distributions from disordered binary alloys. *Acta Crystallographica A*, 27(3):198–201, 1971.

[15] Victoria M. Nield and David A. Keen. *Diffuse Neutron Scattering from Crystalline Materials*. Oxford University Press, 2001.

[16] J. M. Cowley. An approximate theory of order in alloys. *Phys. Rev.*, 77:669–675, 1950.

[17] J. M. Cowley. *Diffraction Physics*. North-Holland Pub. Co. ; American Elsevier Amsterdam : New York, 1975.

[18] G. L. Squires. *Introduction to the Theory of Thermal Neutron Scattering*. Cambridge University Press Cambridge ; New York, 1978.

[19] Stephan Rosenkranz and Raymond Osborn. Corelli: Efficient single crystal diffraction with elastic discrimination. *Pramana*, 71(4):705–711, 2008.

[20] Feng Ye, Yaohua Liu, Ross Whitfield, Ray Osborn, and Stephan Rosenkranz. Implementation of cross correlation for energy discrimination on the time-of-flight spectrometer CORELLI. *Journal of Applied Crystallography*, 51(2):315–322, 2018.

[21] Tara M. Michels-Clark, Andrei T. Savici, Vickie E. Lynch, Xiaoping Wang, Michal Chodkiewicz, Thomas Weber, Hans-Beat Bürgi, and Christina M. Hoffmann. Expanding Lorentz and spectrum corrections to large volumes of reciprocal space for single-crystal time-of-flight neutron diffraction. Corrigendum. *Journal of Applied Crystallography*, 50(5):1559, 2017.

[22] O. Arnold, J.C. Bilheux, J.M. Borreguero, A. Buts, S.I. Campbell, L. Chapon, M. Doucet, N. Draper, R. Ferraz Leal, M.A. Gigg, V.E. Lynch, A. Markvardsen, D.J. Mikkelson, R.L. Mikkelson, R. Miller, K. Palmen, P. Parker, G. Passos, T.G. Perring, P.F. Peterson, S. Ren, M.A. Reuter, A.T. Savici, J.W. Taylor, R.J. Taylor, R. Tolchenov, W. Zhou, and J. Zikovsky. Mantid - data analysis and visualization package for neutron scattering and μsr experiments. *Nuclear Instruments and Methods in Physics Research Section A: Accelerators, Spectrometers, Detectors and Associated Equipment*, 764:156 – 166, 2014.

[23] CCTW - Crystal Coordinate Transformation Workflow.

[24] M. Paściak, A. P. Heerdegen, D. J. Goossens, R. E. Whitfield, A. Pietraszko, and T. R. Welberry. Assessing local structure in $PbZn_{1/3}Nb_{2/3}O_3$ using diffuse scattering and reverse monte carlo refinement. *Metallurgical and Materials Transactions A*, 44(1):87–93, 2013.

[25] T. Proffen and R. B. Neder. *DISCUS*: a program for diffuse scattering and defect-structure simulation. *Journal of Applied Crystallography*, 30(2):171–175, 1997.

[26] R. B. Neder and T. Proffen. *Diffuse Scattering and Defect Structure Simulations*. Oxford University Press, 2008.

[27] M. J. Krogstad, P. Gehring, S. Rosenkranz, R. Osborn, F. Ye, Y. Liu, J. P. C. Ruff, W. Chen, J. M. Wozniak, H. Luo, O. Chmaissem, Z.-G. Ye, and D. Phelan. The relation of local order to material properties in relaxor ferroelectrics. *Nature Materials*, 17:718–724, 2018.

[28] Raffaele Resta. Macroscopic polarization in crystalline dielectrics: the geometric phase approach. *Rev. Mod. Phys.*, 66:899–915, 1994.

[29] Raffaele Resta. Electrical polarization and orbital magnetization: the modern theories. *Journal of Physics: Condensed Matter*, 22(12):123201, 2010.

[30] Neil W. Ashcroft and N. D. Mermin. *Solid State Physics*. New York, Holt, Rinehart and Winston, 1976.

[31] George Samara. Ferroelectricity revisited—advances in materials and physics. *Solid State Physics*, 56:239–458, 12 2001.

[32] A. L. Kholkin, N. A. Pertsev, and A. V. Goltsev. *Piezoelectricity and Crystal Symmetry*, pages 17–38. Springer US, Boston, MA, 2008.

[33] Gen Shirane and Sadao Hoshino. On the phase transition in lead titanate. *Journal of the Physical Society of Japan*, 6(4):265–270, 1951.

[34] A Kania, P Daniel, and A Słodczyk. Cubic–tetragonal–orthorhombic phase transition sequence in 0.5pb($mg_{1/3}nb_{2/3}$)o_3-0.5pbtio_3 and 0.36pb($mg_{1/3}nb_{2/3}$)o_3-0.64pbtio_3 single crystals. *Journal of Physics: Condensed Matter*, 18(42):9625, 2006.

[35] R. Blinc. *Advanced Ferroelectricity*. Oxford University Press, 2011.

[36] Kazuma Hirota, Shuichi Wakimoto, and David E. Cox. Neutron and x-ray scattering studies of relaxors. *Journal of the Physical Society of Japan*, 75(11):111006, 2006.

[37] Wolfgang Kleemann. Random fields in relaxor ferroelectrics - a jubilee review. *Journal of Advanced Dielectrics*, 02(02):1241001, 2012.

[38] P Bonneau, P Garnier, G Calvarin, E Husson, Jean-Raymond Gavarri, A Hewat, and Morell AJ. X-ray and neutron diffraction studies of the diffuse phase transition in $PbMg_{1/3}Nb_{2/3}O_3$ ceramics. 91:350–361, 04 1991.

[39] D. Phelan, E.E. Rodriguez, J. Gao, Y. Bing, Z.-G. Ye, Q. Huang, Jinsheng Wen, Guangyong Xu, C. Stock, M. Matsuura, and P.M. Gehring. Phase diagram of the relaxor ferroelectric (1-x)pb($mg_{1/3}nb_{2/3}$)o_3-xpbtio_3 revisited: a neutron powder diffraction study of the relaxor skin effect. *Phase Transitions*, 88(3):283–305, 2015.

[40] Ilya Grinberg, Pavol Juhás, Peter K. Davies, and Andrew M. Rappe. Relationship between local structure and relaxor behavior in perovskite oxides. *Phys. Rev. Lett.*, 99:267603, 2007.

[41] N de Mathan, E Husson, G Calvarn, J R Gavarri, A W Hewat, and A Morell. A structural model for the relaxor $PbMg_{1/3Nb2/3}O_3$ at 5 k. *Journal of Physics: Condensed Matter*, 3(42):8159, 1991.

[42] Z.-G. Bokov, A. A.and Ye. Recent progress in relaxor ferroelectrics with perovskite structure. *Journal of Materials Science*, 41(1):31–52, 2006.

[43] Yiping Guo, Haosu Luo, Di Ling, Haiqing Xu, Tianhou He, and Zhiwen Yin. The phase transition sequence and the location of the morphotropic phase boundary region in (1-x)[Pb ($Mg_{1/3}$ $Nb_{2/3}$) O_3]-x$PbTiO_3$ single crystal. *Journal of Physics: Condensed Matter*, 15(2):L77, 2003.

[44] Guangyong Xu. Probing local polar structures in PZN-xPT and PMN-xPT relaxor ferroelectrics with neutron and x-ray scattering. 320:012081, 2011.

[45] Peter Gehring. Neutron diffuse scattering in lead-based relaxor ferroelectrics and its relationship to the ultra-high piezoelectricity. 2:1241005, 2012.

[46] V. Westphal, W. Kleemann, and M. D. Glinchuk. Diffuse phase transitions and random-field-induced domain states of the 'relaxor' ferroelectric $PbMg1_{/3}Nb_{2/3}O_3$. *Phys. Rev. Lett.*, 68:847–850, 1992.

[47] Desheng Fu, Hiroki Taniguchi, Mitsuru Itoh, Shin-ya Koshihara, N. Yamamoto, and Shigeo Mori. Relaxor $Pb(Mg_{1/3}Nb_{2/3})\mathbf{O}_3$: A ferroelectric with multiple inhomogeneities. *Phys. Rev. Lett.*, 103:207601, 2009.

[48] Y. Ni, H. T. Chen, Y. P. Shi, L. H. He, and A. K. Soh. Modeling of polar nano-regions dynamics on the dielectric response of relaxors. *Journal of Applied Physics*, 113(22):224104, 2013.

[49] Fei Li, Shujun Zhang, Tiannan Yang, Zhuo Xu, N Zhang, Gang Liu, Jianjun Wang, Jianli Wang, Z Cheng, Zuo-Guang Ye, Jun Luo, Thomas R. Shrout, and Long-Qing Chen. The origin of ultrahigh piezoelectricity in relaxor-ferroelectric solid solution crystals. 7:13807, 12 2016.

[50] Fei Li, Zhuo Xu, and Shujun Zhang. The effect of polar nanoregions on electromechanical properties of relaxor-$PbTiO_3$ crystals: Extracting from electric-field-induced polarization and strain behaviors. *Applied Physics Letters*, 105(12):122904, 2014.

[51] R. Pirc, R. Blinc, and V. S. Vikhnin. Effect of polar nanoregions on giant electrostriction and piezoelectricity in relaxor ferroelectrics. *Phys. Rev. B*, 69:212105, 2004.

[52] Hiroyuki Takenaka, Ilya Grinberg, Shi Liu, and Andrew M. Rappe. Slush-like polar structures in single-crystal relaxors. *Nature*, 546:391–395, 2017.

[53] J Hlinka. Do we need the ether of polar nanoregions? 2:1241006, 2012.

[54] Benjamin Paul Burton, Eric Cockayne, and Umesh V. Waghmare. Correlations between nanoscale chemical and polar order in relaxor ferroelectrics and the lengthscale for polar nanoregions. *Phys. Rev. B*, 72:064113, 2005.

[55] David Sherrington. Bzt: A soft pseudospin glass. *Phys. Rev. Lett.*, 111:227601, Nov 2013.

[56] A. R. Akbarzadeh, S. Prosandeev, Eric J. Walter, A. Al-Barakaty, and L. Bellaiche. Finite-temperature properties of $Ba(Zr,Ti)O_3$ relaxors from first principles. *Phys. Rev. Lett.*, 108:257601, 2012.

[57] Darren J. Goossens. Diffuse scattering from lead-containing ferroelectric perovskite oxides. *ISRN Materials Science*, (17):107178, 2013.

[58] Guangyong Xu, Z. Zhong, H. Hiraka, and G. Shirane. Three-dimensional mapping of diffuse scattering in $Pb(Zn_{1/3}Nb_{2/3})O_3$-x$PbTi_{O3}$. *Phys. Rev. B*, 70:174109, 2004.

[59] Daniel Phelan, Christopher Stock, Jose A. Rodriguez-Rivera, Songxue Chi, Juscelino Leão, Xifa Long, Yujuan Xie, Alexei A. Bokov, Zuo-Guang Ye, Panchapakesan Ganesh, and Peter M. Gehring. Role of random electric fields in relaxors. *Proceedings of the National Academy of Sciences*, 2014.

[60] C. Stock, Guangyong Xu, P. M. Gehring, H. Luo, X. Zhao, H. Cao, J. F. Li, D. Viehland, and G. Shirane. Neutron and x-ray diffraction study of cubic [111] field-cooled $Pb(Mg_{1/3}Nb_{2/3})O_3$. *Phys. Rev. B*, 76:064122, 2007.

[61] G. Xu, Z. Zhong, Y. Bing, Z.-G. Ye, and G. Shirane. Electric-field-induced redistribution of polar nano-regions in a relaxor ferroelectric. *Nature Materials*, 5:134–140, 2006.

[62] Guangyong Xu, G. Shirane, J. R. D. Copley, and P. M. Gehring. Neutron elastic diffuse scattering study of $Pb(Mg_{1/3}Nb_{2/3})O_3$. *Phys. Rev. B*, 69:064112, 2004.

[63] H. Hiraka, S.-H. Lee, P. M. Gehring, Guangyong Xu, and G. Shirane. Cold neutron study on the diffuse scattering and phonon excitations in the relaxor $Pb(Mg_{1/3}Nb_{2/3})O_3$. *Phys. Rev. B*, 70:184105, 2004.

[64] P. M. Gehring, H. Hiraka, C. Stock, S.-H. Lee, W. Chen, Z.-G. Ye, S. B. Vakhrushev, and Z. Chowdhuri. Reassessment of the burns temperature and its relationship to the diffuse scattering, lattice dynamics, and thermal expansion in relaxor $Pb(Mg_{1/3}Nb_{2/3})O_3$. *Phys. Rev. B*, 79:224109, 2009.

[65] C. Stock, R. J. Birgeneau, S. Wakimoto, J. S. Gardner, W. Chen, Z.-G. Ye, and G. Shirane. Universal static and dynamic properties of the structural transition in $Pb(Zn_{1/3}Nb_{2/3})O_3$. *Phys. Rev. B*, 69:094104, Mar 2004.

[66] Marek Paściak, Marek Wołcyrz, and Adam Pietraszko. Interpretation of the diffuse scattering in pb-based relaxor ferroelectrics in terms of three-dimensional nanodomains of the ⟨110⟩-directed relative interdomain atomic shifts. *Phys. Rev. B*, 76:014117, 2007.

[67] Sergey Vakhrushev, A Ivanov, and Jiri Kulda. Diffuse neutron scattering in relaxor ferroelectric $pb(mg_{1/3}nb_{2/3})o_3$. 7:2340–5, 06 2005.

[68] A. Bosak, D. Chernyshov, Sergey Vakhrushev, and M. Krisch. Diffuse scattering in relaxor ferroelectrics: true three-dimensional mapping, experimental artefacts and modelling. *Acta Crystallographica A*, 68(1):117–123.

[69] Hiroyuki Takenaka, Ilya Grinberg, and Andrew M. Rappe. Anisotropic local correlations and dynamics in a relaxor ferroelectric. *Phys. Rev. Lett.*, 110:147602, 2013.

[70] A. Tkachuk and Haydn Chen. Anti-ferrodistortive nanodomains in pmn relaxor. *AIP Conference Proceedings*, 677(1):55–64, 2003.

[71] I. P. Swainson, C. Stock, P. M. Gehring, Guangyong Xu, K. Hirota, Y. Qiu, H. Luo, X. Zhao, J.-F. Li, and D. Viehland. Soft phonon columns on the edge of the Brillouin zone in the relaxor $Pb(Mg_{1/3}Nb_{2/3})O_3$. *Phys. Rev. B*, 79:224301, 2009.

[72] A. D. Hilton, D. J. Barber, C. A. Randall, and T. R. Shrout. On short range ordering in the perovskite lead magnesium niobate. *Journal of Materials Science*, 25(8):3461–3466, Aug 1990.

[73] Masato Matsuura, Hitoshi Endo, Mitsuyoshi Matsushita, Yoshihito Tachi, Yosuke Iwasaki, and Kazuma Hirota. Study of slow lattice dynamics in relaxor ferroelectric PMN–30%PT by neutron spin echo technique. *Journal of the Physical Society of Japan*, 79(3):033601, 2010.

[74] P M Gehring, W Chen, Z-G Ye, and G Shirane. The non-rhombohedral low-temperature structure of PMN–10% PT. *Journal of Physics: Condensed Matter*, 16(39):7113, 2004.

[75] Varley F. Sears. Neutron scattering lengths and cross sections. *Neutron News*, 3(3):26–37, 1992.

[76] G. Xu, P. M. Gehring, C. Stock, and K. Conlon. The anomalous skin effect in single crystal relaxor ferroelectric PZN-xPT and PMN-xPT. *Phase Transitions*, 79(1-2):135–152, 2006.

[77] Akhilesh Kumar Singh, Dhananjai Pandey, and Oksana Zaharko. Powder neutron diffraction study of phase transitions in and a phase diagram of (1-x)$Pb(Mg_{1/3}Nb_{2/3})O_3$-x$PbTiO_3$. *Phys. Rev. B*, 74:024101, 2006.

[78] Darren J. Goossens. Local ordering in lead-based relaxor ferroelectrics. *Accounts of Chemical Research*, 46(11):2597–2606, 2013.

[79] Q. Li, S. Danilkin, G. Deng, J. Wang, Z. L. R. L. Withers, Z. Xu, and Y. Liu. Soft Phonon Modes and Diffuse Scattering in $Pb(In_{1/2}Nb_{1/2})O_3$-$Pb(Mg_{1/3}Nb_{2/3})O_3$-$PbTiO_3$ Relaxor Ferroelectrics. *ArXiv e-prints*, 2016.

[80] T. R. Welberry, M. J. Gutmann, Hyungje Woo, D. J. Goossens, Guangyong Xu, C. Stock, W. Chen, and Z.-G. Ye. Single-crystal neutron diffuse scattering and Monte Carlo study of the relaxor ferroelectric $PbZn_{1/3}Nb_{2/3}O_3$ (PZN). *Journal of Applied Crystallography*, 38(4):639–647, 2005.

[81] C. Stock, D. Ellis, I. P. Swainson, Guangyong Xu, H. Hiraka, Z. Zhong, H. Luo, X. Zhao, D. Viehland, R. J. Birgeneau, and G. Shirane. Damped soft phonons and diffuse scattering in 40 *Phys. Rev. B*, 73:064107, 2006.

[82] Guangyong Xu, D. Viehland, J. F. Li, P. M. Gehring, and G. Shirane. Evidence of decoupled lattice distortion and ferroelectric polarization in the relaxor system PMN $-$ xPT. *Phys. Rev. B*, 68:212410, Dec 2003.

[83] M. Matsuura, K. Hirota, P. M. Gehring, Z.-G. Ye, W. Chen, and G. Shirane. Composition dependence of the diffuse scattering in the relaxor ferroelectric compound (1-x)$Pb(Mg_{1/3}Nb_{2/3})O_3$-x$PbTiO_3$ ($0 \leq x \leq 0.40$). *Phys. Rev. B*, 74:144107, 2006.

[84] Y. M. Jin, Y. U. Wang, A. G. Khachaturyan, J. F. Li, and D. Viehland. Conformal miniaturization of domains with low domain-wall energy: Monoclinic ferroelectric states near the morphotropic phase boundaries. *Phys. Rev. Lett.*, 91:197601, 2003.

[85] S. Vakhrushev, A. Nabereznov, S.K. Sinha, Y.P. Feng, and T. Egami. Synchrotron x-ray scattering study of lead magnoniobate relaxor ferroelectric crystals. *Journal of Physics and Chemistry of Solids*, 57(10):1517 – 1523, 1996. Proceeding of the 3rd Williamsburg Workshop on Fundamental Experiments on Ferroelectrics.

[86] Sergey Prosandeev and L. Bellaiche. Effects of atomic short-range order on properties of the $PbMg_{1/3}Nb_{2/3}O_3$ relaxor ferroelectric. *Phys. Rev. B*, 94:180102, 2016.

[87] Jinsheng Wen, Guangyong Xu, C. Stock, and P. M. Gehring. Response of polar nanoregions in 68%$Pb(Mg_{1/3}Nb_{2/3})O_3$-32%$PbTiO_3$ to a [001] electric field. *Applied Physics Letters*, 93(8):082901, 2008.

[88] Y. Cao, G. Sheng, J. X. Zhang, S. Choudhury, Y. L. Li, C. A. Randall, and L. Q. Chen. Piezoelectric response of single-crystal $PbZr_{1-x}Ti_xO_3$ near morphotropic phase boundary predicted by phase-field simulation. *Applied Physics Letters*, 97(25):252904, 2010.

[89] F. Jona, G. Shirane, F. Mazzi, and R. Pepinsky. X-ray and neutron diffraction study of antiferroelectric lead zirconate, $pbzro_3$. *Phys. Rev.*, 105:849–856, Feb 1957.

[90] Nan Zhang, Hiroko Yokota, Anthony Michael Glazer, Zhipeng Ren, David A Keen, Donald S Keeble, Pam A. Thomas, and Z. Ye. The missing boundary in the phase diagram of $PbZr_{1-x}Ti_xO_3$. *Nature communications*, 5:5231, 2014.

[91] D. Phelan, X. Long, Y. Xie, Z.-G. Ye, A. M. Glazer, H. Yokota, P. A. Thomas, and P. M. Gehring. Single crystal study of competing rhombohedral and monoclinic order in lead zirconate titanate. *Phys. Rev. Lett.*, 105:207601, 2010.

[92] Gen Shirane, Kazuo Suzuki, and Akitsu Takeda. Phase transitions in solid solutions of $PbZrO_3$ and $PbTiO_3$ (ii) x-ray study. *Journal of the Physical Society of Japan*, 7(1):12–18, 1952.

[93] A. M. Glazer. The classification of tilted octahedra in perovskites. *Acta Crystallographica Section B*, 28(11):3384–3392, 1972.

[94] P. M. Woodward. Octahedral Tilting in Perovskites. I. Geometrical Considerations. *Acta Crystallographica Section B*, 53(1):32–43, 1997.

[95] Thomas Weber and Arkadiy Simonov. The three-dimensional pair distribution function analysis of disordered single crystals: Basic concepts. 227:238–247, 2012.

[96] A. Simonov, T. Weber, and W. Steurer. *Yell*: a computer program for diffuse scattering analysis *via* three-dimensional delta pair distribution function refinement. *Journal of Applied Crystallography*, 47(3):1146–1152, 2014.

APPENDIX A

TRANSFORMING X-RAY DETECTOR IMAGES INTO ORIENTED HKL SPACE

A stack of x-ray detector images can be transformed into hkl space via a series of linear transforms plus a non-linear transform to change from real space to reciprocal space – essentially, many changes of basis for a three-dimensional vector space. This treatment was originally developed by Branton Campbell in an attempt to generate something compatible with Bruker software; it has since been adapted by Guy Jennings for use in the CCTW software and is used in the NXRefine package for analysis of x-ray scattering data. The following treatment has been slightly adapted to account for a detector that is *not* physically coupled to the sample goniometer via a 2θ arm, i.e., the detector tilts are independent of the goniometer tilts, and the detector is always normal to the incident beam, modified by the detector tilts.

The direct lab coordinate system is defined with $+\hat{\boldsymbol{x}}$ coinciding with the incident beam direction, $+\hat{\boldsymbol{z}}$ pointing along the direction from the base of the goniometer circle to the sample position (usually vertical from the floor), and $+\hat{\boldsymbol{y}}$ so as to define a right-handed coordinate system. The goniometer has three adjustable (and perhaps partial) angles, ω at the base of the goniometer, χ a mounted on the ω circle, and ϕ the motor closest to the sample (and usually the only motor moving during a scan). When $\omega = \chi = 0$, the axis about which ϕ rotates is coincident with $+\hat{\boldsymbol{z}}$ within some small angle of error about $\hat{\boldsymbol{y}}$, called *goniometer pitch* and denoted here as ψ. Errors in angle about $\hat{\boldsymbol{x}}$ and $\hat{\boldsymbol{z}}$ can be incorporated into other goniometer angles.

The plane of the detector is ideally normal to the incident beam, with any deviation defined by yaw (rotation about $+\hat{\boldsymbol{z}}$), pitch (rotation about $+\hat{\boldsymbol{y}}$, and roll (rotation about $+\hat{\boldsymbol{x}}$). The distance from the sample to the detector is l.

There are several coordinate systems that define the relation between reciprocal space and the detector:

1) Pixel coordinates; measured in pixels from the beam center incident on the detector face. In this system, $+\hat{\boldsymbol{x}}$ is horizontal, left-to-right as viewed on the detector face (corre-

sponding to direct lab $+\hat{\boldsymbol{y}}$) and $+\hat{\boldsymbol{x}}$ is vertical (corresponding to direct lab $+\hat{\boldsymbol{z}}$). Pixels are squares of length s_p. With x_{cen} and y_{cen} being the beam center location on the detector in pixels, the vector $\mathbf{t}_{pd}$ is defined

$$\mathbf{t}_{pd} = \begin{bmatrix} x_{cen} \\ y_{cen} \\ 0 \end{bmatrix}$$

2) Oriented-detector coordinates; measured in millimeters and with the same axes as the direct lab coordinate system when all detector and goniometer angles are zero. The matrix $\mathbf{O}$ transforms from the direct lab space to pixel axes; in the experimental geometry described above,

$$\mathbf{O} = \begin{bmatrix} 0 & 0 & -1 \\ -1 & 0 & 0 \\ 0 & 1 & 0 \end{bmatrix}$$

3) Direct-lab coordinates, as defined above. In the lab axes, using the notation $R_{\hat{\boldsymbol{i}}}(\theta)$ to indicate a rotation about axis $\hat{\boldsymbol{i}}$ of angle θ, $\mathbf{D}$ is defined:

$$\mathbf{D} = R_{\hat{\boldsymbol{x}}}(roll)R_{\hat{\boldsymbol{y}}}(pitch)R_{\hat{\boldsymbol{z}}}(yaw)$$

and the vector going from the origin of the oriented-detector frame to the origin of the direct-lab frame (i.e., from the beam center on the detector to the sample) is

$$\mathbf{t}_d s = \begin{bmatrix} l \\ 0 \\ 0 \end{bmatrix}$$

4) The reciprocal-lab frame, with identical axes to the direct lab frame, using units of inverse Angstroms. This frame could be called unoriented **Q** space, as it is independent of the orientation of the crystal being studied. The vector $\mathbf{t}_E$ pointing from the origin of the reciprocal-lab frame to the origin of the direct lab frame is defined by the wavelength λ, with $\mathbf{t}_E = (\frac{1}{\lambda}, 0, 0)$.

5) The goniometer-head coordinate system, with identical origin and units to the reciprocal-lab frame. When all goniometer angles are 0°, this is identical to the reciprocal-lab frame, but the axes move with the goniometer. The matrix that transforms from goniometer-head coordinates to reciprocal lab coordinates is **G**; using the conventions outlined earlier,

$$\mathbf{G} = R_{\hat{\boldsymbol{z}}}(\phi) R_{\hat{\boldsymbol{x}}}(\chi) R_{\hat{\boldsymbol{z}}}(\omega) R_{\hat{\boldsymbol{y}}}(\psi)$$

6) The crystal coordinate system, with identical origin and units to the reciprocal-lab system. The axes are fixed to the crystal, with $+\hat{\boldsymbol{x}}$ coinciding with the crystal $+\hat{\boldsymbol{a}}^*$, $+\hat{\boldsymbol{y}}$ perpendicular to $+\hat{\boldsymbol{x}}$ in the plane defined by $\hat{\boldsymbol{a}}^*$ and $\hat{\boldsymbol{b}}^*$ and the angle between $+\hat{\boldsymbol{y}}$ and $+\hat{\boldsymbol{b}}^*$ less than 90°, and $+\hat{\boldsymbol{z}}$ completing the right-handed set. The matrix that transforms from crystal coordinates to goniometer-head coordinates is **U**. For an orthorhombic crystal, if $\hat{\boldsymbol{a}}^*$, $\hat{\boldsymbol{b}}^*$, and $\hat{\boldsymbol{c}}^*$ coincide with $\hat{\boldsymbol{x}}$, $\hat{\boldsymbol{y}}$, and $\hat{\boldsymbol{z}}$, **U** will be the identity matrix.

7) The reciprocal-lattice coordinate system, defined by reciprocal lattice vectors $\hat{\boldsymbol{a}}^*$, $\hat{\boldsymbol{b}}^*$, and $\hat{\boldsymbol{c}}^*$. The matrix **B** transforms from this basis to the crystal coordinate system. The

inverse of this matrix $\mathbf{B^{-1}}$ can be written in terms of the unit cell parameters $a, b, c, \alpha, \beta, \gamma$ as

$$\mathbf{B}^{-1} = \begin{bmatrix} a & b\cos\gamma & c\cos\beta \\ 0 & b\sin\gamma & c\frac{\cos\alpha - \cos\beta\cos\gamma}{\sin\gamma} \\ 0 & 0 & c\sqrt{\sin^2\beta - (\frac{\cos\alpha - \cos\beta\cos\gamma}{\sin\gamma})^2)} \end{bmatrix}$$

If the unit cell has $\alpha = \beta = \gamma = 90°$, this easily inverts to

$$\mathbf{B} = \begin{bmatrix} 1/a & 0 & 0 \\ 0 & 1/b & 0 \\ 0 & 0 & 1/c \end{bmatrix}$$

By transforming from one frame to the next, one can go from a stack of detector images to reciprocal lattice coordinates.

$$\mathbf{v}_1 = (i, j, 0)$$

$$\mathbf{v}_2 = s_p \times \mathbf{O}^{-1}(\mathbf{v}_1 - \mathbf{t}_{pd})$$

$$\mathbf{v}_3 = \mathbf{D}^{-1}\mathbf{v}_2 - \mathbf{t}_{ds}$$

$$\mathbf{v}_4 = (Q_x, Q_y, Q_z) = \frac{1}{\lambda}\frac{\mathbf{v}_3}{|\mathbf{v}_3|} - \mathbf{t}_E$$

$$\mathbf{v}_5 = \mathbf{G}^{-1} \cdot \mathbf{v}_4$$

$$\mathbf{v}_6 = \mathbf{U}^{-1} \cdot \mathbf{v}_5$$

$$\mathbf{v}_7 = \mathbf{B}^{-1} \cdot \mathbf{v}_6 = (h, k, l)$$

APPENDIX B

RIGHT TO USE AUTHOR CONTRIBUTION TO *NATURE MATERIALS* ARTICLE "THE RELATION BETWEEN LOCAL ORDER AND MATERIAL PROPERTIES IN RELAXOR FERROELECTRICS"

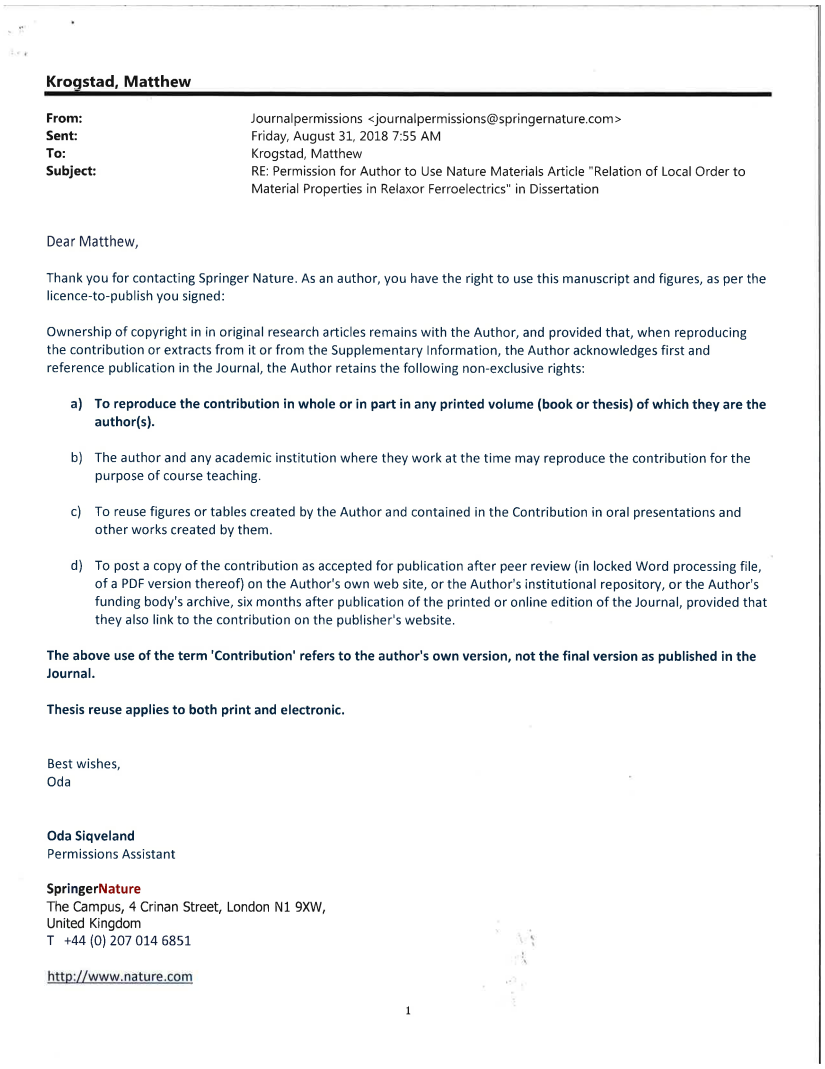

Krogstad, Matthew

From: Journalpermissions <journalpermissions@springernature.com>
Sent: Friday, August 31, 2018 7:55 AM
To: Krogstad, Matthew
Subject: RE: Permission for Author to Use Nature Materials Article "Relation of Local Order to Material Properties in Relaxor Ferroelectrics" in Dissertation

Dear Matthew,

Thank you for contacting Springer Nature. As an author, you have the right to use this manuscript and figures, as per the licence-to-publish you signed:

Ownership of copyright in in original research articles remains with the Author, and provided that, when reproducing the contribution or extracts from it or from the Supplementary Information, the Author acknowledges first and reference publication in the Journal, the Author retains the following non-exclusive rights:

a) **To reproduce the contribution in whole or in part in any printed volume (book or thesis) of which they are the author(s).**

b) The author and any academic institution where they work at the time may reproduce the contribution for the purpose of course teaching.

c) To reuse figures or tables created by the Author and contained in the Contribution in oral presentations and other works created by them.

d) To post a copy of the contribution as accepted for publication after peer review (in locked Word processing file, of a PDF version thereof) on the Author's own web site, or the Author's institutional repository, or the Author's funding body's archive, six months after publication of the printed or online edition of the Journal, provided that they also link to the contribution on the publisher's website.

The above use of the term 'Contribution' refers to the author's own version, not the final version as published in the Journal.

Thesis reuse applies to both print and electronic.

Best wishes,
Oda

Oda Siqveland
Permissions Assistant

SpringerNature
The Campus, 4 Crinan Street, London N1 9XW,
United Kingdom
T +44 (0) 207 014 6851

http://www.nature.com

1

Figure B.1: Email permitting the use of previously published work for this dissertation.

Some of the work presented here, particularly in Chapter 3, was previously presented in *Nature Materials* Article "The Relation Between Local Order and Material Properties in Relaxor Ferroelectrics." The journal gives permission for authors to reproduce their original contribution in a book or thesis, and this permission has been explicitly reiterated in the email above.